

1 **Recent global decline of CO₂ fertilization effects on vegetation photosynthesis**

2 Songhan Wang^{1, 2}, Yongguang Zhang^{1, 2, 3*}, Weimin Ju^{1, 2}, Jing M. Chen^{1, 4}, Philippe Ciais⁵,
3 Alessandro Cescatti⁶, Jordi Sardans^{7, 8}, Ivan A. Janssens⁹, Mousong Wu^{1, 2}, Joseph A. Berry¹⁰,
4 Elliott Campbell¹¹, Marcos Fernández-Martínez^{7, 8, 9}, Ramdane Alkama⁶, Stephen Sitch¹², Pierre
5 Friedlingstein¹³, William K. Smith¹⁴, Wenping Yuan¹⁵, Wei He^{1, 2}, Danica Lombardozzi¹⁶,
6 Markus Kautz¹⁷, Dan Zhu⁵, Sebastian Lienert¹⁸, Etsushi Kato¹⁹, Benjamin Poulter²⁰, Tanja GM
7 Sanders²¹, Inken Krüger²¹, Rong Wang²², Ning Zeng^{23, 24}, Hanqin Tian²⁵, Nicolas Vuichard⁵,
8 Atul K. Jain²⁶, Andy Wiltshire²⁷, Vanessa Haverd²⁸, Daniel S. Goll^{5, 29}, Josep Peñuelas^{7, 8}

9 ¹*International Institute for Earth System Sciences, Nanjing University, Nanjing, China.*

10 ²*Jiangsu Provincial Key Laboratory of Geographic Information Technology, Key Laboratory for Land Satellite Remote Sensing
11 Applications of Ministry of Natural Resources, School of Geography and Ocean Science, Nanjing University, Nanjing, Jiangsu
12 210023, China.*

13 ³*Huangshan Park Ecosystem Observation and Research Station, Ministry of Education, China.*

14 ⁴*Department of Geography and Planning, University of Toronto, Toronto, Ontario, Canada.*

15 ⁵*Laboratoire des Sciences du Climat et de l'Environnement, CEA CNRS UVSQ, Gif-sur-Yvette, France.*

16 ⁶*European Commission, Joint Research Centre (JRC), Ispra, Italy.*

17 ⁷*CSIC, Global ecology Unit CREAM-CSIC-UAB, Bellaterra 08193, Catalonia, Spain.*

18 ⁸*CREAF, Cerdanyola del Vallès 08193, Catalonia, Spain.*

19 ⁹*Department of Biology, Centre of Excellence PLECO (Plant and Vegetation Ecology), University of Antwerp, Wilrijk, Belgium.*

20 ¹⁰*Department of Global Ecology, Carnegie Institution for Science, Stanford, California 94305, USA.*

21 ¹¹*Sierra Nevada Research Institute, University of California, Merced, California 95343, USA.*

22 ¹²*College of Life and Environmental Sciences, University of Exeter, Exeter, UK.*

23 ¹³*College of Engineering, Mathematics and Physical Sciences, University of Exeter, Exeter, UK.*

24 ¹⁴*School of Natural Resources and the Environment, University of Arizona, Tucson, AZ, USA.*

25 ¹⁵*School of Atmospheric Sciences, Center for Monsoon and Environment Research, Sun Yat-Sen University, Guangzhou, China.*

26 ¹⁶*Terrestrial Sciences Section, National Center for Atmospheric Research, Boulder, CO, USA.*

27 ¹⁷*Forest Research Institute Baden-Württemberg, Freiburg, Germany.*

28 ¹⁸*Climate and Environmental Physics, Physics Institute, and Oeschger Centre for Climate Change Research, University of Bern,
29 Bern, Switzerland.*

30 ¹⁹*Institute of Applied Energy, Tokyo, Japan.*

31 ²⁰*NASA Goddard Space Flight Center, Greenbelt, MD 20771, USA.*

32 ²¹*Thünen Institute of Forest Ecosystems, Alfred-Möller-Str. 1, 16225 Eberswalde, Germany.*

33 ²²*Department of Environmental Science and Engineering, Fudan University, Shanghai, 200433.*

34 ²³*Department of Atmospheric and Oceanic Science, University of Maryland, College Park, MD 20742, USA.*

35 ²⁴*LASG, Institute of Atmospheric Physics, Chinese Academy of Science, Beijing 100029, China.*

36 ²⁵*International Center for Climate and Global Change Research, School of Forestry and Wildlife Sciences, Auburn University,
37 Auburn, AL, USA.*

38 ²⁶*Department of Atmospheric Sciences, University of Illinois, 105 South Gregory Street, Urbana, IL, 61801-3070, USA.*

39 ²⁷*Met Office, Fitzroy Road, Exeter, Devon, EX1 3PB, UK.*

40 ²⁸*CSIRO Oceans and Atmosphere, Canberra, ACT 2601, Australia.*

41 ²⁹*Institute of Geography, University of Augsburg, Augsburg, Germany.*

42

43 **Abstract**

44 The enhanced vegetation productivity driven by increased levels of carbon dioxide (CO₂) (i.e.
45 the CO₂ fertilization effect, CFE) sustains an important negative feedback on climate warming,
46 but the temporal dynamics of CFE remain unclear. We used multiple long-term satellite- and
47 ground-based data sets to investigate the temporal variations in CFE. Our results indicated that
48 global CFE has declined across most terrestrial regions of the globe during 1982–2015,
49 correlating well with changing nutrient concentrations and availability of soil water. Current
50 carbon-cycle models also demonstrate a declining CFE trend, albeit substantially weaker than
51 that from our Earth observations. This declining trend in the forcing of terrestrial carbon sinks by
52 increasing levels of atmospheric CO₂ implies a weakening negative feedback on the climatic
53 system and increases the society's dependence on future strategies to mitigate climate warming.
54 Our results also highlight the need for continued investments in current carbon-cycle models.

55 **One Sentence Summary:** Observations reveal declined plant response to CO₂

56 Terrestrial ecosystems have accounted for more than half of the global carbon sink during
57 the last six decades and have thus substantially mitigated climate warming (1). Global process-
58 based models attribute part of the increasing land carbon sink (2) to the increase in vegetation
59 productivity driven by the fertilization effect of increasing atmospheric CO₂ concentration (3), a
60 process acting as a negative feedback in the climate system (4), i.e., the CO₂ fertilization effect
61 (CFE). First introduced by Keeling (5), the β factor was generally used to characterize the plant
62 response to increasing CO₂ concentration (i.e., CFE). In order to compare the results between
63 global analysis and experimental measurements, here we used an approximation form of original

64 β ($\beta = \frac{\partial \text{GPP}}{\partial C_a}$) (6), which is defined as the relative increase in gross primary production (GPP) in

65 response to a 100 ppm increase in atmospheric CO₂ concentration (C_a).

66 Increases of GPP originate from the direct acceleration of photosynthesis in response to the
67 increased supply of CO₂ (7), but are also modified by a suite of indirect responses, including
68 water saving because of the reduced stomatal conductance under increasing atmospheric CO₂
69 concentration (8, 9), and nutrient limitation (10). Enhanced GPP and net primary production
70 (NPP) are commonly observed in field experiments, such as free-air CO₂ enrichment (FACE)
71 experiments (7) and open top chamber experiments (11), where ecosystems are being exposed to
72 elevated CO₂ in the range of two times ambient values, albeit with different magnitudes of
73 response across sites (7).

74 The fingerprint of CFE on the carbon and water cycles at global scales (3, 8) is, however,
75 more elusive, given the co-variation of atmospheric CO₂ with other environmental drivers of
76 vegetation productivity. Elucidating this fingerprint of CFE is a scientific problem involving

77 detection-attribution methods, requiring either statistical methods and long-term data such that
78 effects of non-CFE drivers can be removed empirically (12, 13), or process-based models with
79 which CFE can be isolated by deliberate factorial simulations (14).

80 Process-based models of the terrestrial carbon cycle have indicated that CFE accounts for
81 approximately 70% of the increasing global trend in foliar area, i.e. global greening (15), and for
82 up to 60% of the current terrestrial carbon sink (3). These models project that CFE will induce
83 increased land carbon storage by the end of this century, despite opposing effects from climate
84 change (3, 16). A cascade of uncertainties in projecting future land carbon storage arises from
85 the responses of photosynthesis, NPP and ecosystem carbon turnover times to increasing CO₂,
86 especially in the presence of increasing limitations from nutrient and water availability.
87 Therefore, accurately quantifying the temporal dynamics of CFE on GPP is essential for
88 reducing the uncertainties of future land carbon storage and climate projections based on Earth
89 system models (ESMs) (4).

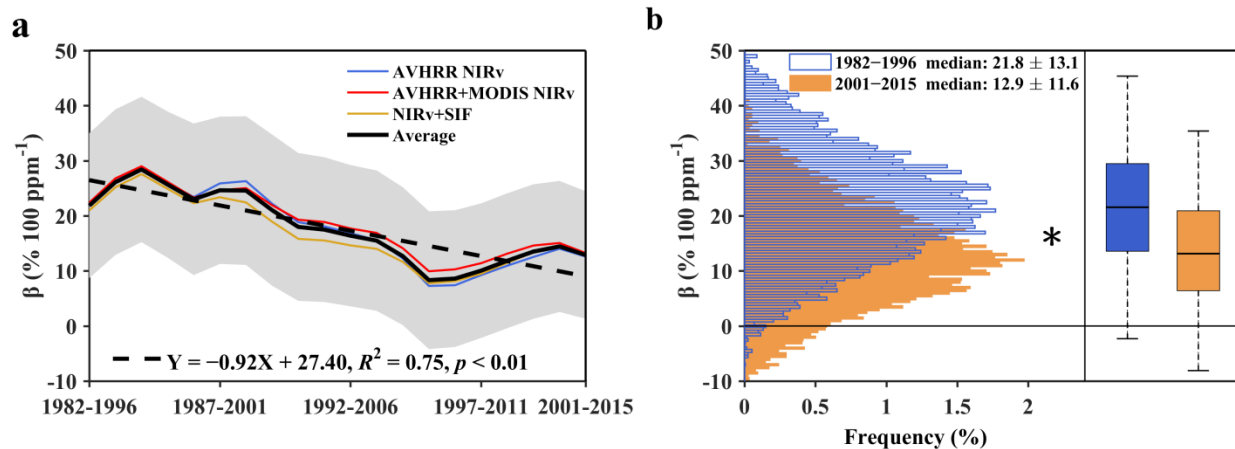
90 Recently, a study based on the long-term CO₂ concentration measurements at Barrow
91 atmospheric measurement station (Alaska, 71°N) found that the sensitivity of the seasonal
92 amplitude (AMP) of atmospheric CO₂ concentration to the increase in CO₂ concentration has
93 decreased, which may suggest a declining response of GPP at northern high-latitudes to
94 atmospheric CO₂ (17). If such declining trend prevails across the globe, the terrestrial vegetation
95 carbon sink response to increasing CO₂ will decrease, with important consequences for the
96 global carbon budget and for the effort required by mitigation policies to meet future climate
97 targets. For this reason, a comprehensive assessment of the temporal dynamics of CFE on global
98 GPP is thus timely and valuable as a first step to understand its impacts on the trends of the land
99 carbon sinks. To address this goal, we used three long-term satellite data sets collected during
100 1982–2015: a recently developed vegetation index (NIR_V) (18) from Advanced Very High
101 Resolution Radiometer (AVHRR NIR_V), the fusion of NIR_V from AVHRR and Moderate
102 Resolution Imaging Spectroradiometer (AVHRR+MODIS NIR_V), and the fusion of NIR_V and
103 sun-induced chlorophyll fluorescence (SIF) (19) (NIR_V+SIF), which are proxies for GPP
104 (hereafter satellite GPP proxies, see Methods, [Supplementary Text S1](#) and [Figs. S1–S2](#)).
105 Comparisons with the GPP estimates from 106 eddy-covariance (EC) flux towers indicated the
106 robustness and generality of using NIR_V as the proxy of GPP ([Figs. S3–S5](#)). We also
107 corroborated our findings using long-term GPP estimates from EC flux towers, and further
108 compared the results with GPP time series from a light-use-efficiency (LUE) model (20) and
109 from an ensemble of terrestrial carbon cycle models (TRENDY v6, trends and drivers of the
110 regional scale sources and sinks of carbon dioxide (14)).

111 Linear and non-linear multiple regression approaches were used to estimate β from satellite
112 GPP proxies at each pixel across the globe (12, 13), which attributed the temporal variations of
113 GPP to the effects of CO₂ and other environmental and climate factors (12, 13) (see Methods).
114 Pixels with large land cover changes were excluded from the analyses (Supplementary Text S2
115 and Fig. S6). The global median β for the entire period (1982–2015) derived from satellite GPP
116 proxies using the non-linear regression method was $16.1 \pm 11.5\% \text{ 100 ppm}^{-1}$ (Fig. S7), consistent
117 with the FACE experiments (7), that on average suggest a 15.5% increase in light-saturated
118 photosynthesis per 100 ppm CO₂. Results showed that the estimated β of different vegetation
119 physiology and biome types were also aligned with experiments (7), e.g., the β values of C₄
120 plants were much smaller than those of C₃ plants (Supplementary Text S3 and Fig. S8). We next
121 calculated the time series of β with 15-year moving windows from 1982 to 2015 and found that β
122 significantly decreased at a rate of $-0.92 \pm 0.12\% \text{ 100 ppm}^{-1} \text{ y}^{-1}$ ($p < 0.01$, Fig. 1a). This decrease
123 was also evident after excluding the crop areas (Fig. S9). Compared to the global median of the
124 declining trend in β , grasslands and plants in cold climate zones exhibited a larger declining
125 trend of β , while the β trends of shrubs and plants in tropical areas were slightly lower;
126 nevertheless, the decreases in β across all the climate zones and land cover types were significant
127 (Fig. S10). Across the global terrestrial areas, β significantly declined from $21.8 \pm 13.1\% \text{ 100}$
128 ppm^{-1} during 1982–1996 to $12.9 \pm 11.6\% \text{ 100 ppm}^{-1}$ during 2001–2015 (Fig. 1b).

129 To test the robustness of this result, we also calculated the time series of β using another
130 data source of AVHRR NIRv (i.e., LTDR NIRv, Supplementary Text S1), using various masks
131 of land cover changes (Supplementary Text S2), using a range of moving windows (i.e., 10- to
132 17-years, Supplementary Text S4), and using various combinations of environmental and climate
133 factors that co-vary with CO₂, including annual maximum, minimum, and mean air temperatures,
134 as well as vapour pressure deficit (VPD), precipitation, soil moisture, terrestrial water storage
135 (TWS), photosynthetically active radiation (PAR), the standardised precipitation
136 evapotranspiration index (SPEI, a drought index) and atmospheric nitrogen deposition (Ndep,
137 Supplementary Text S5 and Tables. S2 & S3). Results also showed a robust decrease in β when
138 using LTDR NIRv (Fig. S11), across various land cover change masks (Fig. S12), different
139 window lengths (Fig. S13) and various combinations of explanatory variables (Figs. S14–S15).
140 We also tested our results using different definitions of growing seasons (Supplementary Text S1)
141 and included the seasonal precipitation into the regression models (Supplementary Text S6), both
142 of which confirmed the robustness of the declining trends in global β (Figs. S16–S17).

143 The uncertainties of the calculated β time series were estimated by combining the
144 propagated uncertainties from original satellite data and the errors introduced from the methods
145 (Supplementary Text S7). Due to the larger noise during the early period of AVHRR satellites

146 (Fig. S18), the uncertainties of β during the early period (before 2000) were about two-fold
 147 higher than those of the late period (after 2000, Fig. S19a). After considering the uncertainties,
 148 the global β estimated from satellite GPP proxies during 2001–2015 was still significantly lower
 149 than that during 1982–1996 (Fig. S19b). To verify whether the trend of β was an artefact of our
 150 regression method, we also estimated the temporal dynamics of β using the optimal fingerprint
 151 attribution method (Supplementary Text S8) and again found that the declining trend of β was
 152 significant (Fig. S20). Altogether, these results based on satellite observations of GPP proxies,
 153 suggest a significantly declining trend in the response of GPP to increasing atmospheric CO₂.
 154



155
 156 **Fig. 1. Declining trend of global β .** **a**, Temporal dynamics of β for three satellite GPP proxies with 15-year moving
 157 windows during 1982–2015. β represents the CFE. The solid black line indicates the average of these three
 158 observations. The grey area indicates one standard deviation (SD) either side of the mean ($n = 12850$). The dashed
 159 black line indicates the linear regression. The trend and statistical significance (p value) of the β time series were
 160 estimated using a nonparametric trend test (Mann-Kendall test). **b**, The histogram distribution of β across all pixels
 161 in two 15-year periods (1982–1996 and 2001–2015, left panel). β was the average of these three satellite GPP
 162 proxies. In the right panel, boxes represent the interquartile ranges of the β values (solid lines represent the median
 163 value), and whiskers extend to one times the interquartile range. Median β of these two periods and their SDs were
 164 marked atop. The asterisk indicates a significantly different β between these two periods using a two-sample
 165 Kolmogorov-Smirnov test at $p < 0.01$.

166 To further assess the decreases in β inferred from satellite GPP proxies, we used other
 167 independent datasets: (1) the GPP time series derived from the revised EC-LUE model (20)
 168 (which also accounted for the direct CO₂ effects on LUE, see Supplementary Text S9), (2)
 169 satellite-based leaf area index (LAI) time series (Supplementary Text S10), (3) multi-year GPP
 170 estimations from 22 EC flux sites (Supplementary Text S11 and Table. S4) and (4) a global long-
 171 term GPP dataset from the Carbon Cycle Data Assimilation System (CCDAS) (Supplementary

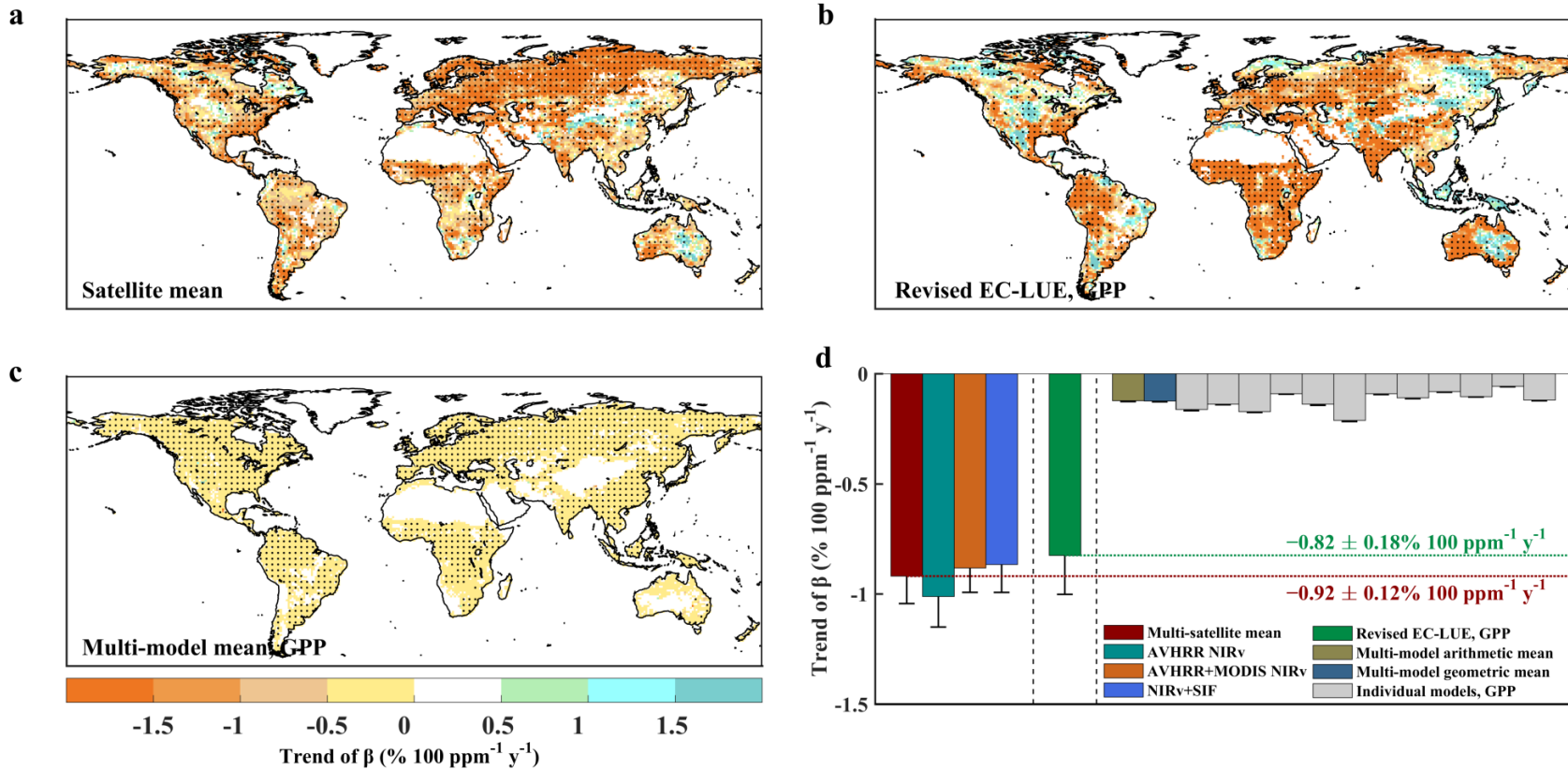
172 [Text S12](#)). We also found a significant declining trend of β based on the revised EC-LUE GPP
173 with a rate of $-0.82 \pm 0.18\% \text{ } 100 \text{ ppm}^{-1} \text{ y}^{-1}$ ([Fig. S21](#)), which was similar to the estimates from
174 satellite GPP proxies. However, the result from satellite-based LAI showed a smaller declining
175 rate of β ($-0.59 \pm 0.11\% \text{ } 100 \text{ ppm}^{-1} \text{ y}^{-1}$) compared to satellite GPP proxies ([Fig. S22](#)). This
176 divergence suggested that the decrease in β was likely due to two factors, the direct effect on
177 foliar physiology, and the indirect effect on LAI. The former referred to the CO_2 -induced
178 stimulation of carboxylation per unit leaf area, while the latter depicted the increased carbon
179 sequestration used for leaf area expansion. The smaller declining β trend from satellite LAI
180 suggested that these two effects were both relevant for the full description of the global decreases
181 in the CO_2 effect on GPP. Ground GPP estimates from EC flux sites also confirmed our findings,
182 by indicating an average declining rate of β at $-0.70\% \text{ } 100 \text{ ppm}^{-1} \text{ y}^{-1}$, which was comparable to
183 the results from satellite GPP proxies around these sites ([Fig. S23](#)). Based on the CCDAS GPP, a
184 data-model fusion product constrained by atmospheric CO_2 observations, which is totally
185 independent from satellite data, we also found a declining β trend at a rate of $-0.62\% \text{ } 100 \text{ ppm}^{-1}$
186 y^{-1} ([Fig. S24](#)). The overall consistency between various remote sensing data, ground
187 measurements and a carbon assimilation system suggests that the global decline of β is robust
188 and coherent across multiple, independent observations.

189 The geographic distribution of the temporal trends of β from satellite GPP proxies ([Fig. 2a](#))
190 revealed that β decreased in approximately 86% of global lands (84–88% for the three satellite
191 GPP proxies, [Fig. S25a-c](#)). Areas with declining β spanned over most of the globe, including
192 Europe, Siberia, western and southern North America, South America, Africa and west Australia.
193 In contrast, increasing β was found in some limited regions of Southeast Asia, east Australia and
194 Northern America ([Fig. 2a-b](#)). These increasing β trends are likely driven by an intensification of
195 management in croplands (i.e. irrigation and fertilization), or related to increasing atmospheric
196 nutrients deposition in recent years ([Fig. S33](#)). We also observed similar spatial patterns for β
197 trends calculated using both 10-year and 17-year moving windows, which proves that our
198 findings are independent of the temporal resolution of the analysis ([Fig. S26](#)). Overall, the
199 decreases of β in tropical areas were smaller, while cold regions had a slightly stronger declining
200 trend ([Figs. S10a & S25a-c](#)). The latter may be because the declining signals of β in northern
201 high-latitudes include both the indirect effects on LAI and the direct effect on foliar physiology,
202 while those in warmer climates include only the physiological effect, given that LAI in some
203 tropical humid regions may already be close to saturation. Results of the satellite LAI confirmed
204 this interpretation by suggesting a larger reduction of β in colder northern regions than in warmer
205 climates ([Fig. S25e&f](#)). Similar declines in β were obtained from the revised EC-LUE GPP,
206 which covered approximately 74% of the global terrestrial area ([Fig. 2b](#)). In general, all data sets

207 indicated that β has been declining in most of global lands, and across various land cover types
208 and climate zones.

209 We then looked at whether an ensemble of state-of-the art carbon cycle models was able to
210 reproduce these observed global declines of β on GPP, since these models are currently used to
211 quantify the terrestrial carbon budget (*I*). We used results from twelve models that contributed to
212 the TRENDY v6 ensemble (*I4*) to calculate β (Supplementary Text S13). For each model, we
213 extracted the differences in simulated GPP between ‘S1’ (time-varying CO₂ only) and ‘S0’
214 (constant CO₂) scenarios, which represented the CO₂ effect on vegetation productivity (see
215 Methods). These models predicted a negative trend in β , both for the multi-model mean and for
216 the individual one, but the declining rate was clearly lower than that derived from satellite GPP
217 proxies and with no evident spatial variations (Figs. 2c & S27). Grouping the estimates of CFE
218 trends, we found that the global β was declining at a rate of $-0.92 \pm 0.12\% \text{ 100 ppm}^{-1} \text{ y}^{-1}$ for
219 satellite GPP proxies, $-0.82 \pm 0.18\% \text{ 100 ppm}^{-1} \text{ y}^{-1}$ for the revised EC-LUE GPP, and only -0.12
220 $\pm 0.01\% \text{ 100 ppm}^{-1} \text{ y}^{-1}$ for TRENDY GPP (Fig. 2d). Looking at individual models, their β trends
221 also had divergences ranging from -0.06 to $-0.21\% \text{ 100 ppm}^{-1} \text{ y}^{-1}$ (Fig. S28), but all of them
222 were lower than that from satellite GPP proxies. Given that we defined β as the per cent increase
223 in GPP per 100 ppm increase in CO₂, and the ‘S1’ simulations solely considered the CO₂ effect,
224 the smaller decreases in β from TRENDY GPP were likely caused by the saturating
225 physiological response of GPP to CO₂ (*2I*), without adequately capturing the concurrent
226 emergence of other limiting factors driven by the changing environmental conditions. We also
227 used GPP from TRENDY ‘S2’ (time-varying CO₂ and climate) and ‘S3’ (time-varying CO₂,
228 climate and land cover changes) scenarios to estimate the trends in β using the same regression
229 approaches as applied for the satellite data (see Methods). The temporal trends of β remained
230 unaltered, with a value of approximately $-0.12 \pm 0.12\% \text{ 100 ppm}^{-1} \text{ y}^{-1}$ for both TRENDY ‘S2’
231 and ‘S3’ simulations (Fig. S29). These results highlight that the ongoing strong decrease in β
232 inferred from satellite data sets is likely to be underestimated by TRENDY models.

233



234

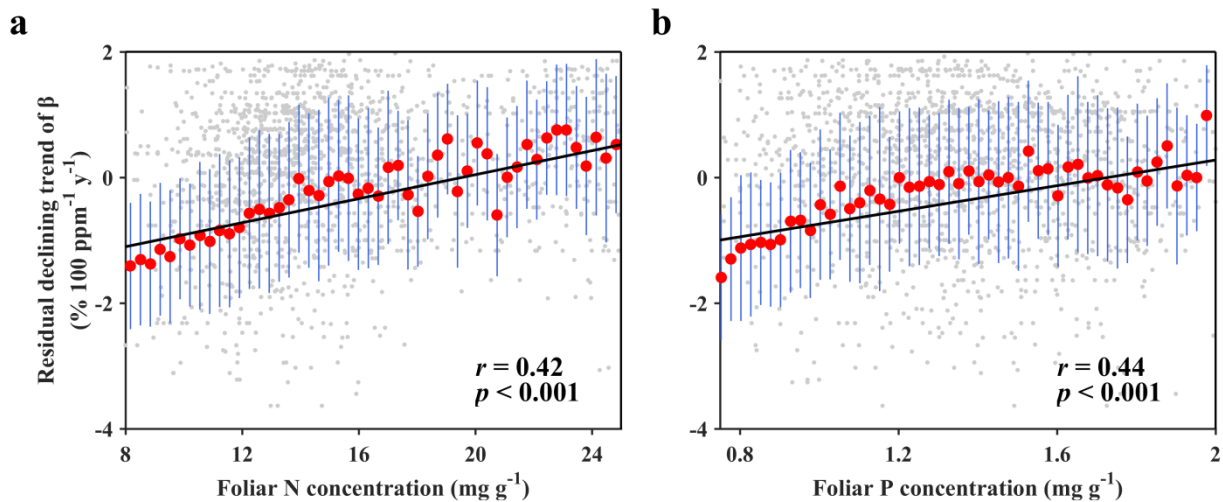
235 **Fig. 2. Global declining trend of β (% 100 ppm⁻¹ y⁻¹).** Spatial patterns of trends in β derived from three data sets using 15-year moving windows: **a**, Means
 236 from three satellite GPP proxies (AVHRR NIR_v, AVHRR+MODIS NIR_v and NIR_v+SIF); **b**, the revised EC-LUE GPP; **c**, multi-model mean GPP from the
 237 TRENDY v6 ensemble. All data sets are from 1982 to 2015. The Mann-Kendall test was used to estimate the trend of β pixel by pixel, and the regions with
 238 black dots indicate significant trends ($p < 0.05$). The pixel size is 1°. **d**, Mean declining trend of β from different data sets. For each data set, we first calculated
 239 the global median β for every moving window during 1982–2015. Then the trends and their standard errors (SEs) for the β time series were estimated. The
 240 error bars represent SEs. The horizontal dotted lines are used to aid comparisons with the results from the TRENDY v6 models.

241 We then looked for possible factors accounting for the declining β and explaining why
242 TRENDY models fail to adequately replicate the magnitude of this phenomenon. Two possible
243 non-mutually exclusive hypotheses were proposed: 1) the increasing constraints on vegetation
244 productivity by emerging nutrient limitations and imbalances that were not adequately
245 represented in models, and 2) current models underestimated the sensitivity of terrestrial GPP
246 to changes in water availability.

247 The first hypothesis relates to the possible effect of the growing limitation of key nutrients,
248 including nitrogen (N) and phosphorus (P). To address this point, here we used 410 groups of
249 ground-based observations of changes in foliar N and P concentrations from the 1990s to the
250 2010s across various tree species in Europe (Supplementary Text S14 and Fig. S30), the
251 continent for which we had ample available data. Results indicated a general decrease in foliar
252 N and P concentrations, with a mean value of $-0.24 \pm 0.06\% \text{ y}^{-1}$ and $-0.55 \pm 0.06\% \text{ y}^{-1}$,
253 respectively (Fig. S31a&b). Our findings are consistent with a recent study suggesting a
254 general global pattern of decreasing foliar N concentration (22), as well as many examples of
255 local to regional decreases in foliar N and P concentrations (23, 24). Enhanced GPP from the
256 increasing atmospheric CO_2 concentration, leading to larger NPP and higher nutrients demands
257 by plants, may partly explain the observed declines of foliar N and P concentrations.
258 Concurrently, these decreases in key foliar nutrients may impose limitations on GPP and
259 thereby limit β . To test this hypothesis, we applied a linear spatial mixed-effects model with
260 3846 site-specific foliar N and P samples (Supplementary Text S14 and Fig. S32), using the
261 trend of β as the response variable, tree species as a random variable, and several potential
262 explanatory variables, including mean annual air temperature (MAT), mean annual
263 precipitation (MAP), and foliar N and P concentrations (Table. S5). After accounting for the
264 trends in β explained statistically by MAT and MAP, we found clear positive correlations
265 between the residual declining trends of β with both foliar N and P concentrations across
266 European forests (Fig. 3). These results suggested that vegetation with lower foliar nutrients
267 concentrations generally showed larger declines in β , therefore supporting our hypothesis of a
268 role of nutrient limitation in the temporal dynamics of β .

269 This phenomenon was also verified from global trends in atmospheric N and P
270 depositions, which suggested that areas with decreasing atmospheric nutrients supply were
271 likely to have larger decreases in β (such as Europe and Siberia), and vice versa (such as East
272 Asia, Fig. S33). This may be because vegetation in areas with declining nutrient supplies from
273 atmospheric depositions tended to have larger N and P limitations on GPP. Moreover, the
274 increases of N and P depositions in some regions of East Asia may explain the increasing trend
275 of β in these areas (Figs. 2a & S33). The ongoing decreases in foliar nutrients might constrain
276 the plant photosynthetic capacity and then resulted in the declining of β , which might not have
277 been adequately represented in current models (Supplementary Text S14). On this aspect, the
278 models that included C-N cycle interactions to emulate nutrient constraints exhibited a larger

279 declining rate of β (Fig. S34), which partly confirmed this interpretation. The role of N
 280 limitation on β has been widely suggested by experimental evidence (10, 25, 26), model
 281 analyses (27) and synthesis reviews (28, 29), all of which were consistent with our analyses.
 282 Our finding regarding P limitation was also consistent with FACE experiments, which
 283 demonstrated that insufficient P availability generally had negative impacts on β (30).
 284 Furthermore, as foliar P:N ratios positively correlated with plant net photosynthesis and growth
 285 (31), the decreasing foliar P:N ratios in European forests (Fig. S31c) suggested a worsening
 286 nutrient imbalance that may partly account for the observed decline in β .



287
 288 **Fig. 3. Relationship between the residual trend of β and foliar nutrients concentrations.** Results for foliar N
 289 (a) and foliar P (b) concentrations after accounting for site mean annual air temperature (MAT), and mean annual
 290 precipitation (MAP) from 3846 samples based on a spatial mixed-effects model. The decreases in β and tree
 291 species were used as the response variables and random factors, respectively. The trends of β were derived from
 292 satellite GPP proxies. MAT, MAP and foliar N and P concentrations were included in the models as the
 293 explanatory variables. Model performance and results are presented in Table. S5. The residual declining trends of
 294 β were then calculated after excluding the effects of background climate (MAT and MAP). Data are classified into
 295 50 bins for clear visualization based on foliar N or P concentrations. The red dots represent the means for each bin,
 296 and the blue lines represent the standard deviations (SDs) of the means. The grey dots represent the raw individual
 297 samples, and solid black lines represent the linear regressions of these grey dots. The correlation coefficients (r)
 298 and p -values are based on the raw data ($n = 3846$).

299 The second, non-mutually exclusive hypothesis to explain the divergence of the β trend
 300 between the TRENDY models and the satellite-derived estimates stated that these models
 301 underestimated the sensitivity of GPP to water availability. The TRENDY models may
 302 underestimate the effect of water availability on GPP, because the coupling between water and
 303 carbon in models has been underestimated (32). To test this hypothesis, we analyzed the
 304 sensitivity of satellite GPP proxies and TRENDY GPP to water availability using a moving
 305 window of 15 years (Supplementary Text S15). We firstly used the TWS data from MERRA-2
 306 (the modern-era retrospective analysis for research and applications, version 2) product to
 307 represent the availability of water to plants and selected arid, temperate and dry tropical
 308 climate zones as the research areas (Fig. S35), as GPP in these zones was found to be highly
 309 sensitive to TWS (Fig. S36). We observed that the sensitivity of GPP to TWS was relatively

310 constant across these three zones for the multi-model mean of TRENDY GPP, whereas the
311 TWS-sensitivities derived from satellite GPP proxies exhibited significantly increasing trends
312 for arid ($2.93 \pm 0.38\% \text{ y}^{-1}$, $p < 0.01$), temperate ($2.12 \pm 0.39\% \text{ y}^{-1}$, $p < 0.01$) and dry tropical
313 ($2.30 \pm 0.57\% \text{ y}^{-1}$, $p < 0.01$) ecosystems (Fig. 4). In temperate and dry tropical areas, the
314 majority of models exhibited divergent results compared to satellite GPP proxies; and almost
315 all of them largely underestimated the GPP sensitivities to TWS in arid areas (Fig. S37). The
316 decreases in β were larger in the regions where the increases of TWS-sensitivities were higher
317 (Fig. S38). These strongly divergent sensitivities between satellite GPP proxies and TRENDY
318 GPP were also confirmed when using three additional TWS products (see Methods,
319 Supplementary Text S15 and Fig. S39) and when using a shorter moving window (Fig. S40).

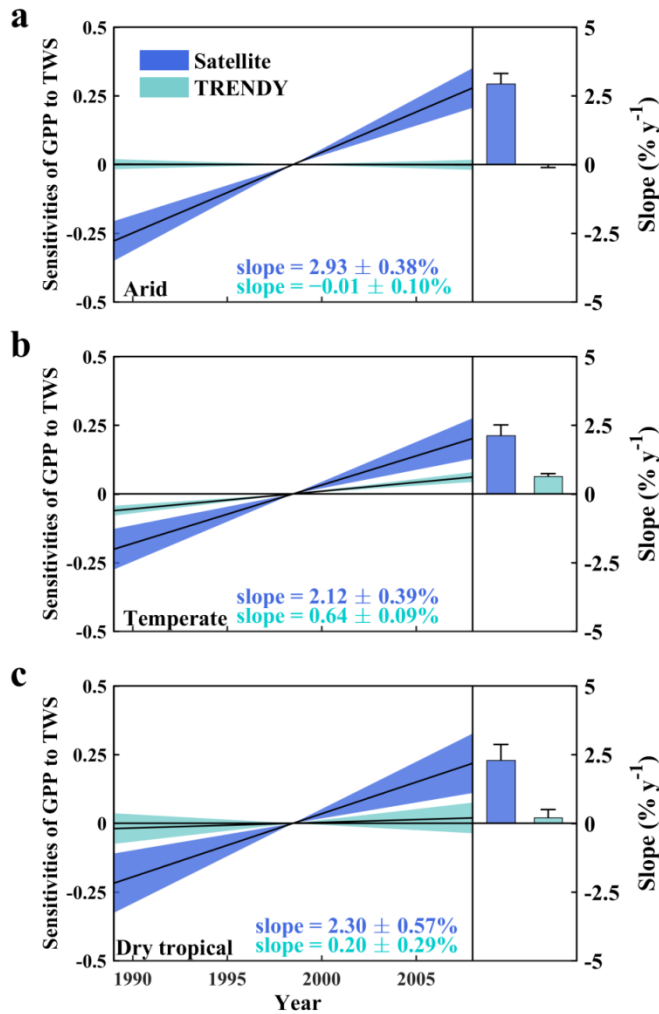
320 This finding implies that GPP and consequently land carbon uptake are more sensitive to
321 the variations in water availability than assumed by the TRENDY models, as previously
322 suggested by several recent studies (33, 34). Moreover, a recent study has shown that the CFE
323 of grasslands could be reduced under drier conditions (35). The relationship between drought
324 stress and CFE is complex and ecosystem specific, and may be impacted by rainfall seasonality
325 and not only by the total annual rainfall. It was shown for instance at 19 grasslands
326 experiments that the annual CFE effect was negated when spring precipitation becomes too
327 low (36). Field experiments also support our results by suggesting that the CFE on vegetation
328 productivity is at least partly limited by water availability (37). The significant increases in the
329 sensitivity of vegetation productivity to TWS may thus partly explain the decreases of β in arid,
330 temperate and dry tropical climate zones.

331 From a theoretical perspective, the global declines of CFE may result from several factors.
332 First, given that the CO_2 -induced photosynthesis stimulation at the leaf level is scaled up to the
333 canopy level through LAI (38, 39), the declining β based on satellite LAI (Fig. S22) could
334 partly explain the global decreases of GPP response to CO_2 . Consistent with our findings, a
335 very recent study based on the FACE experiments on mature forests found a relative low CO_2
336 effect on GPP (40), which may be because the LAI of these forests does not change much (38).
337 Second, the CO_2 effect on photosynthesis at the leaf level involves both the stimulation of
338 carboxylation and the increases in water use efficiency (WUE). The former may possibly be
339 regulated by the foliar key nutrients (N and P), and the latter is related to the water availability.
340 According to the progressive N limitation theory, the soil N availability for plant growth may
341 be expected to diminish over time (41), possibly leading to the observed global decreases in β .
342 A recent study based on carbon isotope measurements revealed the diminishing CO_2 -induced
343 WUE gains across global forests (42), which supported our findings of the water supply
344 limitation on CFE and could partly explain the global declines in β . Moreover, complex
345 interactive effects between nutrients and water supply may also have impacts on CFE. For
346 example, low soil water supply could possibly strengthen the nutrient constraints on CFE
347 through limiting the nutrients decomposition and diffusion in soils (37). Our further analysis

348 based on model simulations showed that the GPP trends have clear reductions in arid areas
349 after considering the interactions between N limitation and climate constrains, which supports
350 this hypothesis (Fig. S41b and Supplementary Text S16). On the other hand, an excess of N
351 fertilizer may result in a reduction in the soil water and therefore possibly lead to drought stress
352 (43). On this aspect, this analysis also highlights the need for future efforts to better understand
353 the complex interactions between nutrients, water and CO₂ effects on vegetation in a climate
354 change perspective.

355 Additional mechanisms may also explain the observed global decrease in CFE. For
356 example, if the environmental saturation point for the CO₂ effect is lower than those suggested
357 in previous studies, as the atmospheric CO₂ is persistently increasing, CFE could be
358 diminishing faster than expected. Meanwhile, due to plant acclimation, the physiological
359 response of vegetation photosynthesis to CO₂ may have changed over time, ultimately
360 affecting the temporal variations of CFE. For instance, a recent study suggested that, due to
361 photosynthetic acclimation, the underinvestment of vegetation in electron transport relative to
362 carboxylation would potentially limit the photosynthetic response to future elevated CO₂ at leaf
363 level (44). In addition, the composition of plant species possibly has changed over time by
364 adaptation to the changing environmental conditions, resulting in a different response of GPP
365 to CO₂. A previous study based on experimental evidence suggested that the CO₂-stimulation
366 of plant productivity was suppressed by the shifts in plant community composition (45).
367 Nevertheless, it is still not feasible to disentangle these factors at the global scale. On the other
368 hand, the effects from plant physiological acclimation and dynamic changes in species
369 composition are also not adequately represented in current models, which also need further
370 investments in the future.

371



372
 373 **Fig. 4. Sensitivities of GPP to TWS.** The change in satellite GPP proxies or TRENDY GPP per unit change in
 374 TWS was estimated for arid (a), temperate (b), and dry tropical (c) climate zones using a moving window of 15
 375 years. To make the comparisons between satellite GPP proxies and TRENDY GPP, the sensitivity time series
 376 have been standardized. The solid lines in the left panels represent the linear regression of the standardized
 377 sensitivity time series based on satellite GPP proxies and TRENDY GPP. We first calculated the global median
 378 sensitivity for every moving window during 1982–2015. Then the trends and their standard errors (SEs) for the
 379 sensitivities time series were estimated. The shaded areas represent the SEs. The bars and error bars in the right
 380 panels represent the slopes and their SEs, respectively.

381 Changes in CO₂ effects on vegetation photosynthesis directly influence the global carbon
 382 cycle and may have large impacts on the water cycle and on global energy budgets by
 383 modifying vegetation transpiration and surface albedo. Our analyses based on multiple decades
 384 of satellite data and long-term observations of surface fluxes at EC flux sites, demonstrated a
 385 significant and spatially extensive decline in the sensitivity of GPP to CO₂. This declining
 386 trend of β implies a substantial reduction of the positive effects of increasing atmospheric CO₂
 387 on terrestrial carbon uptake. A recent study suggested that the CO₂ effect on the carbon cycle
 388 over tropical regions (3) might be counteracted by the impacts from climate-driver changes
 389 (46), in agreement with our findings. Although still under debate, the possibly increasing
 390 trend of the airborne fraction of anthropogenic CO₂ (the fraction that remains in the atmosphere)
 391 may imply a saturation of the CO₂ sinks from land and oceans (47-50), which may be partly

392 caused by the global decline in CFE. Current carbon cycle models also exhibit such global
 393 decreases in β , but fail to adequately detect the sharp declining trend that we identified from
 394 satellite data. This divergence between observations and process-based models possibly
 395 originates from the models' limitations in adequately representing the emerging decline in key
 396 foliar nutrients concentrations and the increasing constraints of water limitations on vegetation
 397 productivity. Ultimately, these results indicate that terrestrial photosynthesis may not increase
 398 as much as models project, possibly reducing the potential of land-based climate mitigation,
 399 further accelerating global warming and exacerbating the efforts required for meeting climate
 400 targets. Our findings also highlight the need for a better characterization of the biogeochemical
 401 and hydrological effects on vegetation in current carbon cycle models in order to produce more
 402 robust projections of the terrestrial carbon budget for the next decades.

403 **References and Notes:**

- 404 1. P. Friedlingstein *et al.*, Global carbon budget 2019. *Earth System Science Data* **11**, 1783-1838
 405 (2019).
- 406 2. A. Ballantyne, C. Alden, J. Miller, P. Tans, J. White, Increase in observed net carbon dioxide
 407 uptake by land and oceans during the past 50 years. *Nature* **488**, 70-72 (2012).
- 408 3. D. Schimel, B. B. Stephens, J. B. Fisher, Effect of increasing CO₂ on the terrestrial carbon cycle.
 409 *Proceedings of the National Academy of Sciences* **112**, 436-441 (2015).
- 410 4. P. Friedlingstein *et al.*, Uncertainties in CMIP5 climate projections due to carbon cycle
 411 feedbacks. *Journal of Climate* **27**, 511-526 (2014).
- 412 5. C. D. Keeling, "The carbon dioxide cycle. Reservoir models to depict the exchange of
 413 atmospheric carbon dioxide with the oceans and land plants" in *Chemistry of the lower*
 414 *atmosphere*, S. I. Rasool, Ed. (Plenum Press, New York, 1973), pp. 251-329.
- 415 6. Bacastow, R., C. D. Keeling, "Atmospheric carbon dioxide and radio-carbon in the natural
 416 carbon cycle. II: Changes from A. D. 1700 to 2070 as deduced from a geochemical model" in
 417 *Carbon in the Biosphere*, G. M. Woodwell, and E. V. Pecan Eds. (Atomic Energy Commission,
 418 Washington, D.C., 1973), pp. 86-136.
- 419 7. E. A. Ainsworth, A. Rogers, The response of photosynthesis and stomatal conductance to rising
 420 [CO₂]: mechanisms and environmental interactions. *Plant, cell & environment* **30**, 258-270
 421 (2007).
- 422 8. T. F. Keenan *et al.*, Increase in forest water-use efficiency as atmospheric carbon dioxide
 423 concentrations rise. *Nature* **499**, 324-327 (2013).
- 424 9. J. A. Morgan *et al.*, C₄ grasses prosper as carbon dioxide eliminates desiccation in warmed
 425 semi-arid grassland. *Nature* **476**, 202-205 (2011).
- 426 10. P. B. Reich *et al.*, Nitrogen limitation constrains sustainability of ecosystem response to CO₂.
 427 *Nature* **440**, 922-925 (2006).
- 428 11. W. I. Dieleman *et al.*, Simple additive effects are rare: a quantitative review of plant biomass
 429 and soil process responses to combined manipulations of CO₂ and temperature. *Global Change*
 430 *Biology* **18**, 2681-2693 (2012).
- 431 12. S. Piao *et al.*, Evaluation of terrestrial carbon cycle models for their response to climate
 432 variability and to CO₂ trends. *Global change biology* **19**, 2117-2132 (2013).
- 433 13. W. K. Smith *et al.*, Large divergence of satellite and Earth system model estimates of global
 434 terrestrial CO₂ fertilization. *Nature Climate Change* **6**, 306-310 (2016).
- 435 14. S. Sitch *et al.*, Recent trends and drivers of regional sources and sinks of carbon dioxide.
 436 *Biogeosciences* **12**, 653-679 (2015).
- 437 15. Z. Zhu *et al.*, Greening of the Earth and its drivers. *Nature Climate Change* **6**, 791-795 (2016).
- 438 16. P. M. Cox *et al.*, Sensitivity of tropical carbon to climate change constrained by carbon dioxide
 439 variability. *Nature* **494**, 341-344 (2013).

- 440 17. J. Peñuelas *et al.*, Shifting from a fertilization-dominated to a warming-dominated period.
441 *Nature ecology & evolution* **1**, 1438-1445 (2017).
- 442 18. G. Badgley, C. B. Field, J. A. Berry, Canopy near-infrared reflectance and terrestrial
443 photosynthesis. *Science advances* **3**, e1602244 (2017).
- 444 19. L. Guanter *et al.*, Global and time-resolved monitoring of crop photosynthesis with chlorophyll
445 fluorescence. *Proceedings of the National Academy of Sciences*, **111**, E1327-E1333 (2014).
- 446 20. W. Yuan *et al.*, Increased atmospheric vapor pressure deficit reduces global vegetation growth.
447 *Science Advances* **5**, eaax1396 (2019).
- 448 21. M. G. De Kauwe, T. F. Keenan, B. E. Medlyn, I. C. Prentice, C. Terrer, Satellite based
449 estimates underestimate the effect of CO₂ fertilization on net primary productivity. *Nature*
450 *Climate Change* **6**, 892-893 (2016).
- 451 22. J. M. Craine *et al.*, Isotopic evidence for oligotrophication of terrestrial ecosystems. *Nature*
452 *Ecology & Evolution* **2**, 1735-1744 (2018).
- 453 23. M. Jonard *et al.*, Tree mineral nutrition is deteriorating in Europe. *Global change biology* **21**,
454 418-430 (2015).
- 455 24. K. K. McLauchlan *et al.*, Centennial-scale reductions in nitrogen availability in temperate
456 forests of the United States. *Scientific Reports* **7**, 7856 (2017).
- 457 25. R. E. McMurtrie *et al.*, Why is plant-growth response to elevated CO₂ amplified when water is
458 limiting, but reduced when nitrogen is limiting? A growth-optimisation hypothesis. *Functional*
459 *Plant Biology* **35**, 521-534 (2008).
- 460 26. R. J. Norby, J. M. Warren, C. M. Iversen, B. E. Medlyn, R. E. McMurtrie, CO₂ enhancement of
461 forest productivity constrained by limited nitrogen availability. *Proceedings of the National*
462 *Academy of Sciences* **107**, 19368-19373 (2010).
- 463 27. VEMAP Participants, Vegetation/ecosystem modeling and analysis project: Comparing
464 biogeography and biogeochemistry models in a continental-scale study of terrestrial ecosystem
465 responses to climate change and CO₂ doubling, *Global Biogeochemical Cycles* **9**, 407-437,
466 1995.
- 467 28. H. Mooney, B. G. Drake, R. Luxmoore, W. Oechel, L. Pitelka, Predicting ecosystem responses
468 to elevated CO₂ concentrations. *BioScience* **41**, 96-104 (1991).
- 469 29. A. D. McGuire, J. M. Melillo, L. A. Joyce, The role of nitrogen in the response of forest net
470 primary production to elevated atmospheric carbon dioxide. *Annual Review of Ecology and*
471 *systematics* **26**, 473-503 (1995).
- 472 30. C. Terrer *et al.*, Nitrogen and phosphorus constrain the CO₂ fertilization of global plant biomass.
473 *Nature Climate Change* **9**, 684-689 (2019).
- 474 31. J. Penuelas *et al.*, Human-induced nitrogen-phosphorus imbalances alter natural and managed
475 ecosystems across the globe. *Nature communications* **4**, 2934 (2013).
- 476 32. V. Humphrey *et al.*, Sensitivity of atmospheric CO₂ growth rate to observed changes in
477 terrestrial water storage. *Nature* **560**, 628-631 (2018).
- 478 33. P. B. Reich *et al.*, Effects of climate warming on photosynthesis in boreal tree species depend
479 on soil moisture. *Nature* **562**, 263-267 (2018).
- 480 34. J. K. Green *et al.*, Large influence of soil moisture on long-term terrestrial carbon uptake.
481 *Nature* **565**, 476-479 (2019).
- 482 35. W. Obermeier *et al.*, Reduced CO₂ fertilization effect in temperate C₃ grasslands under more
483 extreme weather conditions. *Nature Climate Change* **7**, 137-141 (2017).
- 484 36. M. J. Hovenden *et al.*, Globally consistent influences of seasonal precipitation limit grassland
485 biomass response to elevated CO₂. *Nature plants* **5**, 167-173 (2019).
- 486 37. P. B. Reich, S. E. Hobbie, T. D. Lee, Plant growth enhancement by elevated CO₂ eliminated by
487 joint water and nitrogen limitation. *Nature Geoscience* **7**, 920-924 (2014).
- 488 38. Y. Luo, S. Niu, The fertilization effect of CO₂ on a mature forest. *Nature* **580**, 191-192 (2020).
- 489 39. Q. Li *et al.*, Leaf area index identified as a major source of variability in modeled CO₂
490 fertilization. *Biogeosciences* **15**, 6909-6925 (2018).
- 491 40. M. Jiang *et al.*, The fate of carbon in a mature forest under carbon dioxide enrichment. *Nature*
492 **580**, 227-231 (2020).

- 493 41. Y. Luo *et al.*, Progressive nitrogen limitation of ecosystem responses to rising atmospheric
494 carbon dioxide. *Bioscience* **54**, 731-739 (2004).
- 495 42. M. A. Adams, T. N. Buckley, T. L. Turnbull, Diminishing CO₂-driven gains in water-use
496 efficiency of global forests. *Nature Climate Change* **10**, 466-471 (2020).
- 497 43. E. C. da Silva, R. Nogueira, M. A. da Silva, M. B. de Albuquerque, Drought stress and plant
498 nutrition. *Plant stress* **5**, 32-41 (2011).
- 499 44. N. G. Smith, T. F. Keenan, Mechanisms underlying leaf photosynthetic acclimation to warming
500 and elevated CO₂ as inferred from least-cost optimality theory. *Global Change Biology*, **26**,
501 5202-5216 (2020).
- 502 45. J. A. Langley, J. P. Mezonigal, Ecosystem response to elevated CO₂ levels limited by nitrogen-
503 induced plant species shift. *Nature* **466**, 96-99 (2010).
- 504 46. J. Liu *et al.*, Contrasting carbon cycle responses of the tropical continents to the 2015–2016 El
505 Niño. *Science* **358**, eaam5690 (2017).
- 506 47. J. G. Canadell *et al.*, Contributions to accelerating atmospheric CO₂ growth from economic
507 activity, carbon intensity, and efficiency of natural sinks. *Proceedings of the national academy
508 of sciences* **104**, 18866-18870 (2007).
- 509 48. M. Raupach, J. Canadell, C. Le Quéré, Anthropogenic and biophysical contributions to
510 increasing atmospheric CO₂ growth rate and airborne fraction. *Biogeosciences* **5**, 1601-1613
511 (2008).
- 512 49. W. Knorr, Is the airborne fraction of anthropogenic CO₂ emissions increasing? *Geophysical
513 Research Letters* **36**, L21710 (2009).
- 514 50. M. R. Raupach *et al.*, The declining uptake rate of atmospheric CO₂ by land and ocean sinks.
515 *Biogeosciences* **11**, 3453-3475 (2014).
- 516 51. G. Badgley, L. D. Anderegg, J. A. Berry, C. B. Field, Terrestrial Gross Primary Production:
517 Using NIR_v to Scale from Site to Globe. *Global change biology*, **25**, 3731-3740 (2019).
- 518 52. Y. Zhang, J. Joiner, S. H. Alemohammad, S. Zhou, P. Gentine, A global spatially contiguous
519 solar-induced fluorescence (CSIF) dataset using neural networks. *Biogeosciences* **15**, 5779-
520 5800 (2018).
- 521 53. M. Fernández-Martínez *et al.*, Global trends in carbon sinks and their relationships with CO₂
522 and temperature. *Nature climate change* **9**, 73-79 (2019).
- 523 54. P. F. Abbott, & Tabony, R. C., The estimation of humidity parameters. *Meteorological
524 Magazine* **114**, 49-56 (1985).
- 525 55. X. Wang *et al.*, A two-fold increase of carbon cycle sensitivity to tropical temperature
526 variations. *Nature* **506**, 212-215 (2014).
- 527 56. M. C. Peel, B. L. Finlayson, T. A. McMahon, Updated world map of the Köppen-Geiger
528 climate classification. *Hydrology and earth system sciences discussions* **4**, 439-473 (2007).
- 529 57. R. Wang *et al.*, Global forest carbon uptake due to nitrogen and phosphorus deposition from
530 1850 to 2100. *Global change biology* **23**, 4854-4872 (2017).
- 531 58. Y. Zeng *et al.*, A practical approach for estimating the escape ratio of near-infrared solar-
532 induced chlorophyll fluorescence. *Remote Sensing of Environment*, 111209 (2019).
- 533 59. J. E. Pinzon, C. J. Tucker, A non-stationary 1981–2012 AVHRR NDVI3g time series. *Remote
534 Sensing* **6**, 6929-6960 (2014).
- 535 60. J. Pedelty *et al.*, “Generating a long-term land data record from the AVHRR and MODIS
536 instruments” in *IEEE International Geoscience and Remote Sensing Symposium*, 1021-1025
537 (2007).
- 538 61. Y. Y. Liu, A. I. van Dijk, R. A. de Jeu, T. R. Holmes, An analysis of spatiotemporal variations
539 of soil and vegetation moisture from a 29-year satellite-derived data set over mainland Australia.
540 *Water Resources Research* **45**, W07405 (2009).
- 541 62. R. H. Reichle, R. D. Koster, Bias reduction in short records of satellite soil moisture.
542 *Geophysical Research Letters* **31**, L19501 (2004).
- 543 63. E. N. Anagnostou, A. J. Negri, R. F. Adler, Statistical adjustment of satellite microwave
544 monthly rainfall estimates over Amazonia. *Journal of Applied Meteorology* **38**, 1590-1598
545 (1999).

- 546 64. Y. Y. Liu, R. A. de Jeu, M. F. McCabe, J. P. Evans, A. I. van Dijk, Global long-term passive
547 microwave satellite-based retrievals of vegetation optical depth. *Geophysical Research Letters*
548 **38**, L18402 (2011).
- 549 65. M. Reichstein *et al.*, On the separation of net ecosystem exchange into assimilation and
550 ecosystem respiration: review and improved algorithm. *Global Change Biology* **11**, 1424-1439
551 (2005).
- 552 66. D. D. Baldocchi *et al.*, Outgoing Near Infrared Radiation from Vegetation Scales with Canopy
553 Photosynthesis Across a Spectrum of Function, Structure, Physiological Capacity and Weather.
554 *Journal of Geophysical Research: Biogeosciences*, **125**, e2019JG005534 (2020).
- 555 67. B. Dechant *et al.*, Canopy structure explains the relationship between photosynthesis and sun-
556 induced chlorophyll fluorescence in crops. *Remote Sensing of Environment* **241**, 111733 (2020).
- 557 68. G. Wu *et al.*, Radiance-based NIRv as a proxy for GPP of corn and soybean. *Environmental*
558 *Research Letters* **15**, 034009 (2020).
- 559 69. Y. Zhang, J. Joiner, P. Gentine, S. Zhou, Reduced solar-induced chlorophyll fluorescence from
560 GOME-2 during Amazon drought caused by dataset artifacts. *Global change biology* **24**, 2229-
561 2230 (2018).
- 562 70. K. H. Cook, E. K. Vizy, Impact of climate change on mid-twenty-first century growing seasons
563 in Africa. *Climate Dynamics* **39**, 2937-2955 (2012).
- 564 71. S. Piao, J. Fang, L. Zhou, P. Ciais, B. Zhu, Variations in satellite-derived phenology in China's
565 temperate vegetation. *Global change biology* **12**, 672-685 (2006).
- 566 72. S. J. Jeong, C. H. HO, H. J. GIM, M. E. Brown, Phenology shifts at start vs. end of growing
567 season in temperate vegetation over the Northern Hemisphere for the period 1982–2008. *Global*
568 *change biology* **17**, 2385-2399 (2011).
- 569 73. J. Barichivich *et al.*, Large-scale variations in the vegetation growing season and annual cycle
570 of atmospheric CO₂ at high northern latitudes from 1950 to 2011. *Global change biology* **19**,
571 3167-3183 (2013).
- 572 74. G. C. Hurtt *et al.*, Harmonization of land-use scenarios for the period 1500–2100: 600 years of
573 global gridded annual land-use transitions, wood harvest, and resulting secondary lands.
574 *Climatic change* **109**, 117 (2011).
- 575 75. S. Bontemps *et al.*, “Consistent global land cover maps for climate modelling communities:
576 current achievements of the ESA’s land cover CCI” in *Proceedings of the ESA Living Planet*
577 *Symposium*, Edinburgh, 9-13 (2013).
- 578 76. X.-P. Song *et al.*, Global land change from 1982 to 2016. *Nature* **560**, 639-643 (2018).
- 579 77. E. A. Ainsworth, S. P. Long, What have we learned from 15 years of free-air CO₂ enrichment
580 (FACE)? A meta-analytic review of the responses of photosynthesis, canopy properties and
581 plant production to rising CO₂. *New Phytologist* **165**, 351-372 (2005).
- 582 78. S. J. Wand, G. F. Midgley, M. H. Jones, P. S. Curtis, Responses of wild C₄ and C₃ grass
583 (Poaceae) species to elevated atmospheric CO₂ concentration: a meta-analytic test of current
584 theories and perceptions. *Global Change Biology* **5**, 723-741 (1999).
- 585 79. V. Haverd *et al.*, Higher than expected CO₂ fertilization inferred from leaf to global
586 observations. *Global change biology* **26**, 2390-2402 (2020).
- 587 80. J. Carnicer *et al.*, Widespread crown condition decline, food web disruption, and amplified tree
588 mortality with increased climate change-type drought. *Proceedings of the National Academy of*
589 *Sciences* **108**, 1474-1478 (2011).
- 590 81. A. Anav *et al.*, Spatiotemporal patterns of terrestrial gross primary production: A review.
591 *Reviews of Geophysics* **53**, 785-818 (2015).
- 592 82. Z. Sun *et al.*, Spatial pattern of GPP variations in terrestrial ecosystems and its drivers: Climatic
593 factors, CO₂ concentration and land-cover change, 1982–2015. *Ecological Informatics* **46**, 156-
594 165 (2018).
- 595 83. W. J. Van Leeuwen, B. J. Orr, S. E. Marsh, S. M. Herrmann, Multi-sensor NDVI data
596 continuity: Uncertainties and implications for vegetation monitoring applications. *Remote*
597 *sensing of environment* **100**, 67-81 (2006).

- 598 84. C. Cao, X. Xiong, A. Wu, X. Wu, Assessing the consistency of AVHRR and MODIS L1B
599 reflectance for generating fundamental climate data records. *Journal of Geophysical Research:*
600 *Atmospheres* **113**, D09114 (2008).
- 601 85. M. Crosetto, J. A. M. Ruiz, B. Crippa, Uncertainty propagation in models driven by remotely
602 sensed data. *Remote Sensing of Environment* **76**, 373-385 (2001).
- 603 86. K. Guan *et al.*, Improving the monitoring of crop productivity using spaceborne solar-induced
604 fluorescence. *Global change biology* **22**, 716-726 (2016).
- 605 87. W. Yuan *et al.*, Deriving a light use efficiency model from eddy covariance flux data for
606 predicting daily gross primary production across biomes. *Agricultural and Forest Meteorology*
607 **143**, 189-207 (2007).
- 608 88. W. Yuan *et al.*, Global comparison of light use efficiency models for simulating terrestrial
609 vegetation gross primary production based on the LaThuile database. *Agricultural and forest*
610 *meteorology* **192**, 108-120 (2014).
- 611 89. W. Yuan *et al.*, Global estimates of evapotranspiration and gross primary production based on
612 MODIS and global meteorology data. *Remote Sensing of Environment* **114**, 1416-1431 (2010).
- 613 90. G. v. Farquhar, S. v. von Caemmerer, J. Berry, A biochemical model of photosynthetic CO₂
614 assimilation in leaves of C₃ species. *Planta* **149**, 78-90 (1980).
- 615 91. G. J. Collatz, J. T. Ball, C. Grivet, J. A. Berry, Physiological and environmental regulation of
616 stomatal conductance, photosynthesis and transpiration: a model that includes a laminar
617 boundary layer. *Agricultural and Forest meteorology* **54**, 107-136 (1991).
- 618 92. B. E. Medlyn *et al.*, Reconciling the optimal and empirical approaches to modelling stomatal
619 conductance. *Global Change Biology* **17**, 2134-2144 (2011).
- 620 93. T. F. Keenan *et al.*, Recent pause in the growth rate of atmospheric CO₂ due to enhanced
621 terrestrial carbon uptake. *Nature Communications* **7**, 13428 (2016).
- 622 94. I. C. Prentice, N. Dong, S. M. Gleason, V. Maire, I. J. Wright, Balancing the costs of carbon
623 gain and water transport: testing a new theoretical framework for plant functional ecology.
624 *Ecology letters* **17**, 82-91 (2014).
- 625 95. L. Korson, W. Drost-Hansen, F. J. Millero, Viscosity of water at various temperatures. *The*
626 *Journal of Physical Chemistry* **73**, 34-39 (1969).
- 627 96. Z. Zhu *et al.*, Global data sets of vegetation leaf area index (LAI) 3g and Fraction of
628 Photosynthetically Active Radiation (FPAR) 3g derived from Global Inventory Modeling and
629 Mapping Studies (GIMMS) Normalized Difference Vegetation Index (NDVI3g) for the period
630 1981 to 2011. *Remote sensing* **5**, 927-948 (2013).
- 631 97. B. Poulter *et al.*, Contribution of semi-arid ecosystems to interannual variability of the global
632 carbon cycle. *Nature* **509**, 600-603 (2014).
- 633 98. S. Piao *et al.*, Evidence for a weakening relationship between interannual temperature
634 variability and northern vegetation activity. *Nature communications* **5**, 5018 (2014).
- 635 99. Y. Knyazikhin, J. Martonchik, R. B. Myneni, D. Diner, S. W. Running, Synergistic algorithm
636 for estimating vegetation canopy leaf area index and fraction of absorbed photosynthetically
637 active radiation from MODIS and MISR data. *Journal of Geophysical Research: Atmospheres*
638 **103**, 32257-32275 (1998).
- 639 100. C. Jiang *et al.*, Inconsistencies of interannual variability and trends in long-term satellite leaf
640 area index products. *Global change biology* **23**, 4133-4146 (2017).
- 641 101. P. J. Rayner *et al.*, Two decades of terrestrial carbon fluxes from a carbon cycle data
642 assimilation system (CCDAS). *Global Biogeochemical Cycles* **19**, GB2026 (2005).
- 643 102. T. Kaminski *et al.*, Consistent assimilation of MERIS FAPAR and atmospheric CO₂ into a
644 terrestrial vegetation model and interactive mission benefit analysis. *Biogeosciences* **9**, 3173-
645 3184 (2012).
- 646 103. M. Scholze *et al.*, Simultaneous assimilation of SMOS soil moisture and atmospheric CO₂ in-
647 situ observations to constrain the global terrestrial carbon cycle. *Remote sensing of environment*
648 **180**, 334-345 (2016).
- 649 104. H. Graven *et al.*, Enhanced seasonal exchange of CO₂ by northern ecosystems since 1960.
650 *Science*, **341**, 1085-1089 (2013).

- 651 105. J. Kattge, W. Knorr, T. Raddatz, C. Wirth, Quantifying photosynthetic capacity and its
652 relationship to leaf nitrogen content for global-scale terrestrial biosphere models. *Global*
653 *Change Biology* **15**, 976-991 (2009).
- 654 106. A. P. Walker *et al.*, The relationship of leaf photosynthetic traits—V_cmax and J_{max}—to leaf
655 nitrogen, leaf phosphorus, and specific leaf area: a meta-analysis and modeling study. *Ecology*
656 *and evolution* **4**, 3218-3235 (2014).
- 657 107. P. B. Reich, S. E. Hobbie, T. D. Lee, M. A. Pastore, Unexpected reversal of C₃ versus C₄ grass
658 response to elevated CO₂ during a 20-year field experiment. *Science* **360**, 317-320 (2018).
- 659 108. K. Fleischer *et al.*, Amazon forest response to CO₂ fertilization dependent on plant phosphorus
660 acquisition. *Nature Geoscience*, 1-6 (2019).
- 661 109. V. Haverd *et al.*, A new version of the CABLE land surface model (Subversion revision r4601)
662 incorporating land use and land cover change, woody vegetation demography, and a novel
663 optimisation-based approach to plant coordination of photosynthesis. *Geoscientific Model*
664 *Development* **11**, 2995-3026 (2018).
- 665 110. R. Gelaro *et al.*, The modern-era retrospective analysis for research and applications, version 2
666 (MERRA-2). *Journal of Climate* **30**, 5419-5454 (2017).
- 667 111. P. Doell, H. Mueller Schmied, C. Schuh, F. T. Portmann, A. Eicker, Global-scale assessment of
668 groundwater depletion and related groundwater abstractions: Combining hydrological modeling
669 with information from well observations and GRACE satellites. *Water Resources Research* **50**,
670 5698-5720 (2014).
- 671 112. D. P. Dee *et al.*, The ERA-Interim reanalysis: Configuration and performance of the data
672 assimilation system. *Quarterly Journal of the royal meteorological society* **137**, 553-597 (2011).
- 673 113. M. Rodell *et al.*, The global land data assimilation system. *Bulletin of the American*
674 *Meteorological Society* **85**, 381-394 (2004).
- 675 114. J. M. Chen *et al.*, Vegetation structural change since 1981 significantly enhanced the terrestrial
676 carbon sink. *Nature communications* **10**, 4259 (2019).
- 677 115. W. Ju, J. M. Chen, Distribution of soil carbon stocks in Canada's forests and wetlands simulated
678 based on drainage class, topography and remotely sensed vegetation parameters. *Hydrological*
679 *Processes: An International Journal* **19**, 77-94 (2005).
- 680 116. W. Dorigo *et al.*, Evaluating global trends (1988–2010) in harmonized multi-satellite surface
681 soil moisture. *Geophysical Research Letters* **39**, L18405 (2012).
- 682 117. Y. Ryu, J. A. Berry, D. D. Baldocchi, What is global photosynthesis? History, uncertainties and
683 opportunities. *Remote sensing of environment* **223**, 95-114 (2019).
- 684 118. D. Baldocchi, J. Penuelas, The physics and ecology of mining carbon dioxide from the
685 atmosphere by ecosystems. *Global change biology* **25**, 1191-1197 (2019).
- 686 119. M. Zhao, S. W. Running, Drought-induced reduction in global terrestrial net primary
687 production from 2000 through 2009. *science* **329**, 940-943 (2010).
- 688 120. S. L. Lewis, P. M. Brando, O. L. Phillips, G. M. van der Heijden, D. Nepstad, The 2010
689 amazon drought. *Science* **331**, 554-554 (2011).
- 690 121. S. R. Saleska, K. Didan, A. R. Huete, H. R. Da Rocha, Amazon forests green-up during 2005
691 drought. *Science* **318**, 612-612 (2007).
- 692 122. P. Ciais *et al.*, Europe-wide reduction in primary productivity caused by the heat and drought in
693 2003. *Nature* **437**, 529-533 (2005).
- 694 123. A. Eldering *et al.*, The Orbiting Carbon Observatory-2 early science investigations of regional
695 carbon dioxide fluxes. *Science* **358**, eaam5745 (2017).
- 696 124. M. Kondo *et al.*, Land use change and El Niño-Southern Oscillation drive decadal carbon
697 balance shifts in Southeast Asia. *Nature communications* **9**, 1154 (2018).
- 698 125. W. Lucht *et al.*, Climatic control of the high-latitude vegetation greening trend and Pinatubo
699 effect. *Science* **296**, 1687-1689 (2002).
- 700 126. R. Myneni, K. Yuri, T. Park, MOD15A3H MODIS/Combined Terra+Aqua Leaf Area
701 Index/FPAR Daily L4 Global 500m SIN Grid. NASA LP DAAC (2015).
702 <http://doi.org/10.5067/MODIS/MOD15A3H.006>
- 703 127. C. Schaaf, Z. Wang, MCD43A4 MODIS/Terra+Aqua Nadir BRDF-Adjusted Refelctance Daily
704 L3 Global-500m. NASA LP DAAC (2015). <http://doi.org/10.5067/MODIS/MCD43A4.006>

- 705 128. G. Pastorello *et al.*, The FLUXNET2015 dataset and the ONEFlux processing pipeline for eddy
706 covariance data. *Scientific Data* **7**, 225 (2020).
- 707 129. Y. Zheng *et al.*, Improved estimate of global gross primary production for reproducing its long-
708 term variation, 1982–2017. *Earth System Science Data Discussion* **2019**, 1-31 (2019).
- 709 130. K. A. Masarie, P. P. Tans, Extension and integration of atmospheric carbon dioxide data into a
710 globally consistent measurement record. *Journal of Geophysical Research: Atmospheres* **100**,
711 11593-11610 (1995).
- 712 131. I. Harris, P. D. Jones, T. J. Osborn, D. H. Lister, Updated high-resolution grids of monthly
713 climatic observations—the CRU TS3. 10 Dataset. *International journal of climatology* **34**, 623-
714 642 (2014).
- 715 132. Viovy, N, CRUNCEP Version 7-Atmospheric Forcing Data for the Community Land Model, in
716 *Research Data Archive at the National Center for Atmospheric Research*. Boulder, CO:
717 Computational and Information Systems Laboratory (2018).
718 <https://rda.ucar.edu/datasets/ds314.3/>.
- 719 133. S. M. Vicente-Serrano, S. Beguería, J. I. López-Moreno, M. Angulo, A. El Kenawy, A new
720 global 0.5 gridded dataset (1901–2006) of a multiscalar drought index: comparison with current
721 drought index datasets based on the Palmer Drought Severity Index. *Journal of*
722 *Hydrometeorology* **11**, 1033-1043 (2010).
- 723 134. J. Penuelas *et al.*, Increasing atmospheric CO₂ concentrations correlate with declining
724 nutritional status of European forests. *Communications Biology* **3**, 125 (2020).
- 725 135. J. Pinheiro, D. Bates, S. DebRoy, D. Sarkar, R Core Team, nlme: Linear and nonlinear mixed
726 effects models. *R package version 3.1-139* (2019).
- 727

728 **Acknowledgments: Funding:** this research was supported by the National Key R&D Program
729 of China (2016YFA0600202), Jiangsu Provincial NSF for Distinguished Young Scholars
730 (BK20170018) and International Cooperation and Exchange Programs between NSFC and
731 DFG (41761134082). J.P., P.C., I.A.J., J.S., and D.S.G. would like to acknowledge the financial
732 support from the European Research Council Synergy grant ERC-SyG-2013-610028
733 IMBALANCE-P. S.L. has received funding from the European Union’s Horizon 2020 research
734 and innovation program under grant agreement No 821003 (project CCiCC/4C, Climate-
735 Carbon Interactions in the Coming Century) and SNSF (grant no. 20020_172476). H.Q.T. was
736 supported by US National Science Foundation grants (1903722 and 1243232). We
737 acknowledge the constructive and insightful comments from Dr. Shilong Piao in Peking
738 University. We thank Hannes Müller Schmied for providing the WaterGAP TWS data. The
739 authors are also deeply indebted to the data providers and the managers of the ICP Forests data.
740 We also acknowledge our sincere thanks to all data providers listed in [Table S1](#) for their
741 continuous efforts and for sharing their data. We also thank the three anonymous reviewers for
742 their constructive and insightful suggestions and comments which have greatly improved our
743 manuscript. **Author contributions:** Y.G.Z., S.H.W, and J.P. designed the research; S.H.W.
744 performed the analysis; S.H.W., Y.G.Z., J. P., and W.M.J. drafted the paper; P.C., A.C., J.M.C.,
745 and J.S. contributed to the interpretation of the results and to the writing; I.A.J., M.S.W.,
746 J.A.B., E.C., M.F.M., R.A., S.S., P.F., W.K.S., W.P.Y., W.H., D.L., M.K., D.Z., S.L., E.K., B.P.,
747 T.G.S., I.K., R.W., N.Z., H.Q.T., N.V., A.K.J., A.W., V.H., and D.S.G. provided the data and
748 contributed to the writing. **Competing interests:** the authors declare no competing interests.

749 **Data and materials availability:** all data acquired or used in this analysis are available from
750 the links in [Table S1](#).

751 **Supplementary Materials:**

752 Materials and Methods

753 Supplementary Text S1-S17

754 Figures S1-S47

755 Tables S1-S5

756 References (51-135)

757

758

759

760

761

762

763

764

765

766

767

768

769

770

771

772

773

774

775

776

777

778

779

780

781

782

Supplementary Materials for

Recent global decline of CO₂ fertilization effects on vegetation photosynthesis

Songhan Wang, Yongguang Zhang, Weimin Ju, Jing M. Chen, Philippe Ciais, Alessandro Cescatti, Jordi Sardans, Ivan A. Janssens, Mousong Wu, Joseph A. Berry, Elliott Campbell, Marcos Fernández-Martínez, Ramdane Alkama, Stephen Sitch, Pierre Friedlingstein, William K. Smith, Wenping Yuan, Wei He, Danica Lombardozzi, Markus Kautz, Dan Zhu, Sebastian Lienert, Etsushi Kato, Benjamin Poulter, Tanja GM Sanders, Inken Krüger, Rong Wang, Ning Zeng, Hanqin Tian, Nicolas Vuichard, Atul K. Jain, Andy Wiltshire, Vanessa Haverd, Daniel S. Goll, Josep Peñuelas

Correspondence to: yongguang_zhang@nju.edu.cn

This PDF file includes:

Materials and Methods
Supplementary Text S1-S17
Figs. S1 to S47
Tables S1 to S5

783 **Materials and Methods**

784 *Data*

785 We used three long-term satellite NIR_V and SIF data sets (AVHRR NIR_V,
786 AVHRR+MODIS NIR_V and NIR_V+SIF) to represent the dynamics of GPP during 1982–2015.
787 NIR_V combines the information from total scene NIR reflectance (NIR_T) and the normalized
788 difference vegetation index (NDVI), which is a novel index to estimate the vegetation
789 photosynthesis and able to capture a large fraction of GPP variations at both monthly and
790 annual scales (18, 51). SIF has been widely used as a proxy of GPP at regional and global
791 scales (19). In this analysis, we calculated three products that combined the long-term NIR_V
792 observations from AVHRR and MODIS satellites, and the reconstructed global contiguous SIF
793 (cSIF) data (52). Comparisons with GPP estimates from 106 EC flux sites and global data-
794 driven products indicated that these three satellite data sets could capture GPP variations both
795 in space and time (Figs. S2–S5), and therefore, these three products are the proxies of GPP
796 (hereafter satellite GPP proxies) that can be used to assess β (Supplementary Text S1).

797 A long-term GPP data set (the revised EC-LUE GPP) based on LUE models were also
798 used to assess the temporal dynamics of β. This data set is based on a revised EC-LUE model
799 (20) considered CFE by adding a scale factor to represent the direct CO₂ effects on LUE
800 (Supplementary Text S9). We used two long-term satellite-based LAI data sets to assess the
801 temporal dynamics of β: GIMMS-3g LAI and GIMMS+MODIS LAI (Supplementary Text
802 S10). In addition to satellite data, we also used GPP estimates from 22 EC flux sites which
803 have at least 14 years of uninterrupted observations to calculate the temporal trends of β
804 (Supplementary Text S11).

805 In parallel, we also used the GPP and LAI outputs from the simulations of multiple carbon
806 cycle models (TRENDY v6 ensemble (14), 1982–2015). Twelve models (CABLE, CLM4.5,
807 DLEM, ISAM, JULES, LPJ-GUESS, LPJ-wsl, LPX-Bern, ORCHIDEE-MICT, ORCHIDEE,
808 VEGAS and VISIT) and four experimental scenarios (S0, S1, S2, and S3) were used, which
809 estimated the contributions of CO₂ fertilization, climate change and land cover changes to the
810 global vegetation trends (Supplementary Text S13). Detailed information of the data sets used
811 in this study is presented in Table S1.

812 *Estimation of β*

813 For satellite GPP proxies, two LUE-based GPP datasets and satellite LAI, two alternative
814 regression approaches were used to estimate β (12, 13):

815
$$y = \beta(\text{CO}_2) + C_1(\text{VPD}) + C_2(\text{T max}) + C_3 + \varepsilon \quad (1)$$

816
$$y = \beta(\text{CO}_2) + C_1(\text{VPD}) + C_2(\text{T max}) + C_3(\text{CO}_2 \cdot \text{VPD}) + C_4(\text{CO}_2 \cdot \text{T max}) + C_5 + \varepsilon \quad (2)$$

817 where Eq. (1) represents the linear regression method and Eq. (2) represents the non-linear
818 regression method by adding additional interaction effects of CO₂ and climate on vegetation

819 growth; y represents the growing season integrated satellite GPP proxies, LUE-based GPP or
 820 satellite LAI time series; CO_2 , VPD and T_{max} represent the atmospheric CO_2 concentration,
 821 vapour pressure deficit and the maximum temperature time series, respectively; β , C_1 , C_2 , C_3 ,
 822 C_4 and C_5 represent regression coefficients, and ε is the residual error term.

823 Regressions were estimated on annual anomalies (i.e. annual values minus the mean
 824 signal over the moving window or for the entire period) for all the variables (y , CO_2 , T_{max} and
 825 VPD). Such an approach based on the annual anomalies of these variables could eliminate the
 826 effects from the background values of these factors, but keep their interannual variations
 827 impacts on vegetation growth, which represented the sensitivities of vegetation growth to these
 828 factors (53). For comparison this approach has been applied by computing anomalies on
 829 moving windows or for the entire period (i.e., 1982–2015). The outputs of these two
 830 approaches are very similar (results not shown).

831 The regression coefficients of Eq. (1) and Eq. (2) were estimated pixel by pixel using
 832 maximum likelihood analysis. β were then normalized to the unit of % 100 ppm^{-1} by dividing
 833 the mean value of y during the period. The global variance inflation factors of CO_2 with T_{max}
 834 and VPD were assessed respectively (Fig. S42), which indicated that the regression coefficients
 835 were likely not to be affected by the multicollinearity issue, due to no multicollinearity almost
 836 everywhere.

837 For TRENDY GPP data, we used two categories of methods to estimate β . The first
 838 category follows Eqs. (1) and (2), which was used for GPP data from the TRENDY ‘S2’ and
 839 ‘S3’ scenarios. The second category used the following equation:

$$840 \quad \beta^t = \frac{\text{GPP}_{\text{S1}}^t - \text{GPP}_{\text{S0}}^t}{\text{CO}_2^t - \text{CO}_2^{t_0}} \quad (3)$$

841 where GPP_{S1}^t represents the GPP data in year t from the simulation scenario that used varying
 842 CO_2 (TRENDY ‘S1’), while GPP_{S0}^t represents the GPP data in year t from the simulation
 843 scenario that used constant CO_2 (TRENDY ‘S0’); CO_2^t and $\text{CO}_2^{t_0}$ represent the global mean
 844 atmospheric CO_2 concentrations from NOAA in year t and in the start year (t_0) of the
 845 TRENDY simulations, respectively. Given that the estimation of β was driven by the mean
 846 CO_2 concentrations during the whole growing seasons, the use of global averages instead of
 847 gridded CO_2 concentrations did not affect our results (see details in Fig. S43).

848 The TRENDY v6 models were forced with CRU-NCEP (Climatic Research Unit-National
 849 Centers for Environmental Prediction) climate data, which were produced based on the
 850 monthly CRU climate data set. For consistency with the TRENDY models, in this analysis, we
 851 used the climate data set (T_{max} , T_{min} , T_{mean} , Pre and VAP) from CRU 4.0.1. T_{max} , T_{min}
 852 and T_{mean} represent the maximum, minimum and mean air temperatures, respectively; Pre is
 853 precipitation, and VAP is actual vapour pressure. VPD was then calculated as the difference
 854 between the saturated vapour pressure (SVP) and the actual vapour pressure (VAP) at each
 855 pixel for each month. The SVP was calculated based on the following equation (54):

$$856 \quad \text{SVP} = 0.6107 \times e^{17.38 T_{\text{mean}} / (239.0 + T_{\text{mean}})} \quad (4)$$

857 All data were resampled to 1° scale. To reduce the effects of land cover change on the temporal
858 trends of β , we used two land cover data sets: the land use harmonization (LUH2 v2h) data and
859 the Climate Change Initiative (CCI) product to conduct the masks of land cover change
860 (Supplementary Text S2). For consistency with the TRENDY models, we used the mask from
861 LUH2 data as representative in the following analysis (Fig. S6a).

862 We tested the robustness of the temporal trends of β using the following additional
863 analyses. Firstly, we used another data source of satellite NIRv (i.e., LTDR NIRv) to reproduce
864 the temporal trends of β (Supplementary Text S1). Secondly, various masks of land cover
865 changes were conducted to test whether the decrease in β was an artefact of land cover change
866 (Supplementary Text S2). Thirdly, different time-window lengths were tested, ranging from 10
867 to 17 years, to verify whether the declining trend in β was affected by the window length
868 (Supplementary Text S4). We also tested the robustness of our results by considering the
869 autocorrelation of the original data sets, which also suggested a significantly declining trend in
870 β (Supplementary Text S4 & Fig. S44). Fourthly, various combinations of explanatory
871 variables accounting for the vegetation trends were tested. Thirty different models were
872 conducted to estimate the temporal dynamics of β , which included different combinations of
873 temperatures (T_{min} , T_{max} and MAT), indices of water limitation (VPD, precipitation, soil
874 moisture and TWS), radiation (PAR), a drought index (SPEI) and atmospheric nitrogen
875 deposition (Ndep) (Supplementary Text S5). We also checked our findings by using different
876 definitions of growing seasons (Supplementary Text S1) and by adding the seasonal
877 precipitation into the regression models (Supplementary Text S6). At last, we tested the
878 robustness of the regression method by calculating the temporal dynamics of β using an
879 optimal fingerprint attribution method (Supplementary Text S8).

880 We produced a comprehensive assessment of the uncertainties of the β estimates by
881 quantifying the following components: 1) the uncertainty from the original satellite data; 2) the
882 uncertainty from the cumulative distribution frequency (CDF) fusion method; and 3) the
883 uncertainty from the regression models (Supplementary Text S7). The uncertainties of the
884 original satellite data were propagated from the noises of original satellite GPP proxies. The
885 uncertainty introduced from CDF fusion method was calculated as the differences between the
886 estimated β using the original NIRv and the CDF-fitted NIRv, respectively. The uncertainties
887 from the regression models were estimated using bootstrap analyses (55), for all of the
888 combinations between various models, input data and parameters (Supplementary Text S7).
889 This assessment showed that despite the multiple sources of uncertainties in this analysis, the
890 detected global declining trend in β was robust and statistically significant (Supplementary
891 Text S7 & S17).

892 *Statistical analysis*

893 We firstly calculated β across all pixels with 15-year moving windows during 1982–2015
894 using three satellite GPP proxies. To make comparisons with previous studies (7, 12, 13), β
895 was defined in this study as the relative increase in GPP in response to a 100 ppm increase in
896 CO₂. To this end, for each window, we used the observed ratio of GPP increase per CO₂
897 concentration increase during that period, and extrapolated this ratio to a CO₂ concentration
898 increase of 100 ppm. Comparisons across land cover types and climate zones were defined
899 using the CCI global land cover product and the Köppen-Geiger classification (56) (Fig. S35).
900 The trends and statistical significance (*p* values) of β time series were estimated using a
901 nonparametric trend test (Mann-Kendall test). We tested the robustness of global declines in β
902 by estimating the temporal trends of β using multiple and independent data sources, different
903 masks of land cover changes, different lengths of moving-window, various combinations of
904 explanatory variables and alternative calculation approach. In addition, a comprehensive
905 uncertainty analysis of the β time series has been finally performed (Supplementary Text S7).
906 We then verified this declining trend using a LUE-based GPP data set and two satellite-based
907 LAI data sets. We also verified our results using a totally independent dataset of multi-year
908 GPP estimates from surface observations at 22 EC flux sites, and a global long-term GPP
909 dataset from the Carbon Cycle Data Assimilation System (CCDAS). β from current carbon
910 cycle models (TRENDY v6) was then estimated and compared with satellite data.

911 We analyzed the effects of the decreases in key foliar nutrients concentrations on global
912 declines in β , using three regional or global observations of foliar N and P concentrations.
913 Firstly, we used the time series of foliar N and P concentrations observations from 410
914 European sites to investigate their temporal trends in recent decades (Fig. S30). Secondly, 3846
915 samples of site- and species-specific observations of foliar N and P concentrations across
916 Europe (Fig. S32) were used in the linear mixed-effects model, which identified the
917 relationship between foliar nutrients concentrations with the decreases in β . Finally, we also
918 used the global time series of data for atmospheric N and P deposition during 1980–2013 (57)
919 to investigate the relationship between the trends of N and P depositions and the trends of β
920 (Supplementary Text S14).

921 We analyzed the impacts of water availability on the temporal trends of β by firstly
922 investigating the sensitivity of GPP to TWS. Four TWS data sets were used, which were
923 derived from the MERRA-2 reanalysis data product, WaterGAP 2.2d (Water Global
924 Assessment and Prognosis 2.2d) model outputs, the ERA-Interim product and GLDAS (Global
925 Land Data Assimilation Systems) Noah v2.0 models, respectively. The sensitivities of GPP to
926 the TWS data were estimated with 15-year moving windows using satellite GPP proxies and
927 TRENDY ‘S2’ GPP data. Finally, we investigated the relationship between the trends of TWS
928 sensitivities and the trends of β (Supplementary Text S15).
929

930 **Supplementary Text**931 **S1. Satellite NIR_v and SIF data**

932 We used two long-term (1982–2015) satellite NIR_v data sets: NIR_v from Advanced Very
933 High Resolution Radiometer (AVHRR NIR_v), the fusion of NIR_v from AVHRR and Moderate
934 Resolution Imaging Spectroradiometer (AVHRR+MODIS NIR_v), as proxies of vegetation
935 gross primary productivity (GPP) at the global scale (18). NIR_v, calculated as the product of
936 total scene NIR reflectance (NIR_T) and the normalized difference vegetation index (NDVI), is
937 a novel index to estimate GPP that could disentangle the confounding effects from soil
938 background, foliar area and canopy structure (18). Previous studies have demonstrated that
939 NIR_v can explain a large fraction of GPP variations at both monthly and annual scales and has
940 been successfully used to estimate global terrestrial GPP (51). Because NIR_v is resilient
941 against the soil background contamination, it could isolate the vegetated signal from satellite
942 observations of reflectance and eliminate much of the mixed-pixel problem (18). Moreover, a
943 recent study found that NIR_v could be used to estimate the escape ratio of sun-induced
944 chlorophyll fluorescence (SIF) (58). This is because NIR_v conveys the information of
945 vegetation and their emitted SIF signals, whilst being not sensitive to soil background(18, 58).
946 Comparisons with satellite SIF product (GOME-2 SIF) and radiation transfer simulations
947 demonstrated that NIR_v is highly correlated with SIF across vegetation types and various
948 levels of leaf area, soil brightness and canopy structure (18). Furthermore, global GPP has also
949 been estimated using MODIS NIR_v, which result in a reasonable range falling between the
950 bottom-up GPP estimates and the top-down global constraint on GPP (51). More importantly,
951 it was found that NIR_v accounts for a large fraction of the GPP variations, whose estimates
952 could be advanced by improving the quality of satellite retrievals and accounting for key
953 vegetation properties like the photosynthetic pathway (51).

954 For AVHRR NIR_v, we used the Global Inventory Modeling and Mapping Studies
955 (GIMMS) NDVI version 3g (59) (8-km spatial resolution) and NIR_T data from Land Long
956 Term Data Record (LTDR v4 (60), 5-km spatial resolution) hosted on the Google Earth Engine.
957 To calculate the monthly NIR_T data, we firstly screened the cloudy and cloud shadow pixels
958 using the quality flags from the original datasets, and then took the median value of all
959 available daily pixels. We calculated monthly NIR_v as the product of monthly NDVI and
960 monthly NIR_T ($\text{NIR}_v = (\text{NDVI} - 0.08) \times \text{NIR}_T$). Before multiplication, we subtracted 0.08 from all
961 NDVI values to partially account for the NDVI of bare soil.

962 To test whether our results were affected by the data source of AVHRR reflectance, we
963 also used both the NDVI and NIR_T data from LTDR v4 (60) hosted on the Google Earth
964 Engine. Following the same procedure, we calculated the monthly LTDR NIR_v data during
965 1982–2015 and estimated the time series of global β (Fig. S11). Results based on this
966 alternative dataset also showed a significant decrease in global β at a rate of $-1.09 \pm 0.12\%$ 100
967 $\text{ppm}^{-1} \text{y}^{-1}$ ($p < 0.01$, Fig. S11a).

968 In addition, we calculated the monthly MODIS NIR_v data following the same procedure
969 during 2001–2015 based on MCD43A4 v6 products, which corrected the degradation of
970 MODIS sensors and could thus be used to assess the long-term trend of vegetation dynamics.
971 Finally, we produced the fusion NIR_v by combining AVHRR NIR_v during 1982–2000 and
972 MODIS NIR_v during 2001–2015 using the cumulative distribution frequency (CDF) matching
973 approach (61). Similar CDF approaches have been successfully used to merge satellite
974 observations of soil moisture and other satellite data (61–64). We firstly resample the monthly
975 AVHRR NIR_v and MODIS NIR_v to the scale of 1° based on the nearest neighbour method.
976 The CDF methods were then applied to the monthly AVHRR NIR_v and MODIS NIR_v pixel by
977 pixel. Eight segments of the cumulative distribution were divided using the 0th, 5th, 10th, 25th,
978 50th, 75th, 90th, 95th and 100th percentiles of the AVHRR and MODIS NIR_v data (61). Eight
979 linear regressions were then conducted to adjust MODIS NIR_v to AVHRR NIR_v. Based on an
980 example of a certain pixel (Fig. S1a&b), this CDF method harmonised the yearly NIR_v data in
981 similar absolute magnitudes but maintained the original temporal trends of the individual data
982 series.

983 We tested whether the CDF matching method would introduce some errors into the
984 estimation of β . We used the MODIS NIR_v data during the 2001–2015 window to derive the
985 global β before and after the CDF matching respectively. We excluded the pixels with clear
986 land cover changes (see Supplementary text S2) and then calculated the global median β .
987 Results showed that there were very little differences in global β estimation (Fig. S1c), which
988 suggested that our results were not affected by the CDF matching approach.

989 We tested whether NIR_v could be used as the proxy of GPP in the following aspects (Figs.
990 S3 & S4). Firstly, we analyzed the relationship of monthly AVHRR and MODIS NIR_v (or
991 NDVI) with monthly GPP estimates from 106 eddy-covariance (EC) flux sites (Table S4). We
992 used the monthly GPP estimations (GPP_NT_VUT_REF) from the FLUXNET 2015
993 dataset(65). For each site, the monthly AVHRR NDVI and NIR_v were calculated as the
994 average values of all pixels intersecting a 5-km-diameter circle centered at the latitude and
995 longitude of the site. And for MODIS data, we used a 1-km-diameter circle. The R^2 values
996 between monthly NIR_v (or NDVI) with GPP were then calculated using linear regressions (see
997 the example in Figs. S3a & S4a). Results showed that AVHRR and MODIS NIR_v could
998 explain about 60% and 72% of the monthly variances in ground GPP estimates respectively,
999 which were both significantly higher than those of NDVI (47% for AVHRR and 55% for
1000 MODIS, $p = 0.009$ and $p < 0.001$ respectively, see Figs. S3b & S4b). More importantly, NIR_v
1001 could partly alleviate the saturation of NDVI at high GPP values (Fig. S4a). It should be noted
1002 that the inherent differences in footprints between satellite data and flux sites may have impacts
1003 on the strength of the relationships between satellite NIR_v and ground GPP. Therefore, we
1004 further analyzed the R^2 values between monthly MODIS NIR_v with GPP according to different
1005 homogeneity levels of the flux sites (Fig. S45). We found that the average R^2 value increased to

1006 0.78 at flux sites with homogeneity larger than 90%. This result suggested that the relationships
1007 between NIRv and GPP could be closer if we had factored out the uncertainty driven by
1008 footprint differences, which we did not further investigate because it is beyond the scope of this
1009 study. Nevertheless, several recent studies based on ground NIRv and GPP measurements have
1010 proven the strong relationships between them (66-68), which were consistent with our results.

1011 Secondly, we analyzed the variations of the slopes of monthly NIRv-GPP relationship at
1012 these 106 flux sites. We classified the flux sites into ten major vegetation types, i.e., C₃ crop
1013 (CRO-C3), C₄ crop (CRO-C4), broadleaved deciduous forest (DBF), evergreen broadleaf
1014 forest (EBF), evergreen needleleaf forest (ENF), mixed forest (MF), savannas (SAV),
1015 shrubland (SHR), grassland (GRA), wetland (WET). For each type, we randomly selected two-
1016 thirds of the flux sites as the calibration dataset and used the remaining one-third as validation
1017 dataset. Then we derived the monthly NIRv-GPP relationship based on the calibration dataset
1018 and applied it to the validation dataset. This process was repeated many times, depending on
1019 the number of sites for each type. The slope values of all repetitions were not significantly
1020 different, therefore they were averaged for further analysis. Results showed that NIRv was
1021 strongly correlated with GPP for all the ten vegetation types and the slopes converge for each
1022 vegetation group (Fig. S5). Ultimately, with type-specific NIRv-GPP relationship, global GPP
1023 could be estimated pixel by pixel, consistently with the findings from a recent study (51).

1024 Thirdly, we tested the interannual variability of NIRv-GPP slopes for each site. To meet
1025 this scope, we analyzed the monthly NIRv-GPP relationship for each year at individual sites. If
1026 NIRv-GPP slopes had no significant differences in different years, we could use the temporal
1027 variations of NIRv as the indicator of temporal changes in GPP. Results showed that the NIRv-
1028 GPP slopes had no significant interannual variability at most of the flux sites (for AVHRR
1029 NIRv, 101 of 106; for MODIS NIRv, 103 of 106) (Figs. S3d & S4d). These results indicated
1030 that NIRv was highly correlated with GPP and could capture the temporal variations of GPP.
1031 Therefore, long-term satellite NIRv could be used to assess the CO₂ fertilization effects (CFE,
1032 expressed as β factor).

1033 We also used a satellite-based SIF (a proxy for GPP) dataset. At present, the longest
1034 satellite SIF products are from SCIAMACHY (Scanning Imaging Absorption Spectrometer for
1035 Atmospheric Chartography) and GOME-2 (Global Ozone Monitoring Experiment-2), but these
1036 data suffer from sensor degradation (69) and may not be suitable for long-term analyses. We
1037 therefore used the global contiguous SIF (cSIF) data during 2001–2015 (52) produced using
1038 MODIS surface reflectance, Orbiting Carbon Observatory-2 (OCO-2) SIF and a neural
1039 network method. Then we calculated the fusion of NIRv and cSIF data (NIRv+SIF, 1982–2015)
1040 that combined AVHRR NIRv during 1982–2000 and cSIF during 2001–2015 using the same
1041 CDF matching approach. Three long-term data sets of satellite GPP proxies were therefore
1042 obtained, which could explain approximately 85% of the spatial variations in annual data-
1043 driven GPP product (Fluxcom GPP) (Fig. S2). Note that this value represents the spatial

1044 correlation between global satellite NIR_v and global data-driven GPP, which is not the same
1045 case as shown in (51). Their result (MODIS NIR_v could explain about 68% of annual GPP)
1046 was based on GPP estimates from flux sites, but not based on the global continuous GPP
1047 product. Our analysis based on 106 flux sites also found that MODIS NIR_v could explain
1048 about 72% of the GPP variations, which was the similar with the previous results (18, 51).

1049 We used the growing-season integrated satellite NIR_v data in this analysis. The growing
1050 season for each 1° grid cell of global vegetated areas were identified when the mean monthly
1051 air temperature was > 0°C. The data sets were integrated to yearly using the calculated growing
1052 seasons and resampled to a scale of 1°. We also tested whether the definition criterion of the
1053 growing seasons would affect the global trend of β . Since some biomes in arid or semi-arid
1054 zones were still inactive when the air temperature was > 0°C due to lack of precipitation, we
1055 also included the precipitation threshold (10% or 20%) to redefine the growing seasons (70).
1056 That means, for a given pixel, the start of the season was defined as the date when the
1057 cumulative precipitation exceeded 10% (or 20%) of the annual total rainfall, while the end of
1058 the season was defined as the date when the cumulative precipitation exceeded 90% (or 80%)
1059 of the annual total rainfall (Fig. S16a). The significant negative trends of β in both global scale
1060 and arid and semi-arid areas across different definition criteria of the growing seasons, further
1061 suggested the robustness of the findings (Fig. S16b).

1062 We further tested whether the length of the growing season in the mid- to high-latitudes of
1063 the Northern Hemisphere (>30°N) had changed during 1982–2015. Following a widely used
1064 method in previous studies (71, 72), we firstly used a six-degree polynomial function to fit the
1065 monthly AVHRR NIR_v data for each pixel. Then the start of the season (SOS) and the end of
1066 the season (EOS) were determined as the maximum increase time and the maximum decrease
1067 time of the fitted NIR_v, respectively (72). The length of the growing season (GSL) was
1068 obtained as the period between SOS and EOS in each pixel. The trends of GSL were then
1069 analyzed using the Mann-Kendall test. We found that the GSL of most areas in the northern
1070 high-latitudes had increased during 1982–2015, with a median value of 0.27 days y^{-1} (Fig. S46),
1071 which was consistent with several previous studies based on NDVI (72, 73).

1072 **S2. Robustness of the land cover change**

1073 We calculated the temporal trends of β using various masks of land cover change. We
1074 used two land cover data sets: the land use harmonization (LUH2 v2h) data (74) and the
1075 Climate Change Initiative (CCI) product (75). The LUH2 data is a global gridded land-use
1076 forcing data set, which is used in the simulations of TRENDY v6 (trends and drivers of the
1077 regional scale sources and sinks of carbon dioxide) models (74). The CCI land cover product
1078 covers the period from 1992 to 2015 based on satellite observations (75). We used a series of
1079 set values (i.e., from 5% to 100%) to construct the masks. For example, “5%” means that if the
1080 area of changed land cover was larger than 5% of the total area in a certain 1° pixel, the pixel
1081 was excluded from this analysis. There are almost no differences between the β trends for

1082 various masks (Fig. S12). Moreover, the excluded pixels also have significantly declining
1083 trends, which are similar with the remaining pixels for analysis (Fig. S12). Results
1084 demonstrated that the declining trends of β were robust for various masks of land cover change
1085 and for both of these two land cover products (Fig. S12). For consistency with the TRENDY
1086 models, we used the masks from LUH2 data with a set value of 20% as representative in the
1087 following analysis (Fig. S6a).

1088 To further testify that our findings were not affected by the land cover change masks, we
1089 investigated the relationship of the β trends with the long-term vegetation cover changes during
1090 1982–2015. Based on a long-term vegetation cover dataset (76), we firstly calculated the
1091 percentages of the vegetation cover changes in each 1° pixel, and then related them with the
1092 global β trends. Results showed that there were significantly declining trends of β for all the
1093 scenarios of vegetation cover changes, even in the areas where the vegetation cover was
1094 increasing during the past decades (Fig. S47). Moreover, there was generally no significant
1095 relationship ($p = 0.85$) between vegetation cover change percentages and the β trends, which
1096 suggested that our static land cover change masks did not significantly affect the results and
1097 thus further indicated the robustness of our findings.

1098 **S3. Global distributions of β**

1099 To test whether our multiple regression approaches could estimate the global CO₂ impacts
1100 on vegetation, we further analyzed the global distributions of β and their variations across
1101 different vegetation physiology types (C₃ or C₄), climate zones, and biome types (Fig. S8). The
1102 response of C₄ plants to elevated CO₂ was much smaller than those of C₃ plants, consistently
1103 with the observations from FACE experiments (7, 77, 78) (Fig. S8b). C₃ vegetation in arid
1104 climate zones showed higher β values than in other areas, because plants in these regions may
1105 benefit from the water saving effect (8, 9) (Fig. S8b). Across different biome types (excluding
1106 C₄ plants), forests showed a slightly higher response to elevated CO₂, while shrubs showed the
1107 smallest β values, which were consistent with the results from controlled experiments (7) (Fig.
1108 S8b). Across different forests, β values of deciduous broadleaf forest (DBF) were generally
1109 larger than other forests (Fig. S8b). These results demonstrated the ability of our multiple
1110 regression approaches to investigate the global CO₂ fertilization effect on photosynthesis.

1111 The global median β derived from satellite GPP proxies using our multiple regression
1112 approaches was $16.1 \pm 11.5\% \text{ } 100 \text{ ppm}^{-1}$ (Fig. S7), which was slightly lower than the multi-
1113 model mean value from TRENDY models ($18.6 \pm 9.3\% \text{ } 100 \text{ ppm}^{-1}$). There are also large
1114 divergences among different models in the TRENDY ensemble. For example, global β from
1115 the CABLE model was the highest among these 12 models (Fig. S7), in agreement with the
1116 findings from a recent study (79). Note that their results are not contradicted with our findings,
1117 because they focus on the absolute values of CFE (79), while our analysis aims at estimating
1118 the temporal variations of CFE. On the other hand, based on the same datasets, we both found a

1119 consistent result that the global CFE estimated from the CABLE model was the highest within
1120 the TRENDY ensemble.

1121 The global declining β trends across different land cover types and functional types also
1122 showed some divergence. Fig. S10b shows the medians and standard errors of the β trends for
1123 the major plant function types (PFTs). The median declining β trend in grasslands was larger
1124 than the global median, which may be because grasses with shallow rooting depth are more
1125 sensitive to water limitation. Among different vegetation types, the median declining β trend in
1126 evergreen broadleaf forests (EBF) was the lowest, while the median declining β trend in
1127 deciduous broadleaf forests (DBF) was the highest (Fig. S10b). This may be because EBF are
1128 generally located at tropical areas, where the declining β trends are generally low due to the
1129 LAI in some tropical humid regions may already be close to saturation (Fig. 2a). On the
1130 contrary, the declining β trends in DBF (located at high-latitudes) may include both the indirect
1131 effects on LAI and the direct effect on foliar physiology. Nevertheless, it should be noted that
1132 since this analysis is conducted at a spatial resolution of 1° , a detailed PFT level assessment
1133 would be impractical and uncertain.

1134 **S4. Robustness of the window lengths**

1135 We calculated the temporal dynamics of β using a moving window (15-years) for the
1136 study period (1982–2015). To test whether the changes in β were affected by the length of
1137 moving window, different window lengths were tested, ranging from 10 to 17 years. The
1138 maximum length was set to 17 years to avoid data overlap between the first and last time
1139 window and thus to ensure the independence between them. Considering that yearly satellite
1140 GPP proxies may have about 1-year autocorrelation (Fig. S44a), the minimum window length
1141 was chosen as 10 years. The results demonstrated that the declining trends of β were significant
1142 for all window lengths (Fig. S13). In the following analysis, we used the results of the 15-year
1143 moving window as representative. We also calculated the temporal changes of β using a linear
1144 mixed model that specifically accounts for the temporal autocorrelation with a first-order
1145 autocorrelation function (55, 80). The declining trend of β remained significant after
1146 considering the possible autocorrelation effects (Fig. S44b).

1147 **S5. Robustness of the explanatory variables**

1148 In order to test the robustness of the declining β trends calculated from satellite GPP
1149 proxies, we also calculated the temporal trends of β using various combinations of explanatory
1150 variables. A recent study included maximum annual air temperature (Tmax) and vapour
1151 pressure deficit (VPD) into the regression methods to derive β from satellite net primary
1152 productivity (NPP) data (13), and another study used mean annual air temperature (MAT),
1153 mean annual precipitation (MAP) for the TRENDY NPP data (12). In this study, we did not
1154 specifically choose the climatic constraint factors on vegetation photosynthesis, because the
1155 controlling climatic factors for vegetation growth across different areas are still vague (81). On

1156 the other hand, we used multiple different combinations of factors to represent the climatic and
1157 environmental constraints on vegetation, in order to achieve a robust result. Therefore, overall
1158 thirty different models were used to estimate the temporal trends of β , which included various
1159 combinations of temperatures (Tmin, Tmax, and MAT) and indices of water limitation (VPD,
1160 precipitation, soil moisture, and TWS (terrestrial water storage)). We also included the
1161 photosynthetic active radiation (PAR), the standardized precipitation evapotranspiration index
1162 (SPEI, a drought index), and atmospheric nitrogen deposition (Ndep) into the regression model.
1163 All of these variables were originated from monthly data and we integrated them into yearly
1164 data according to the same growing season period that applied for satellite GPP proxies. Ndep
1165 was not included when calculating β from the TRENDY GPP data, because the GPP
1166 simulations from TRENDY 'S2' and 'S3' scenarios did not consider the impacts of Ndep.

1167 The models including Ndep had a slightly weaker declining trend of β , with a rate of
1168 $-0.75\% \text{ } 100 \text{ ppm}^{-1} \text{ y}^{-1}$ (Table S2). The trends of β from satellite GPP proxies ranged from
1169 -0.75 to $-1.05\% \text{ } 100 \text{ ppm}^{-1} \text{ y}^{-1}$, while those from TRENDY 'S2' GPP ranged from 0.02 to
1170 $-0.37\% \text{ } 100 \text{ ppm}^{-1} \text{ y}^{-1}$ (Tables S2-S3). The models that included soil moisture or TWS
1171 generally showed larger declining β trends, while those models including PAR or Ndep had
1172 slightly smaller decreases in β (Tables S2-S3). We also considered the impacts of water-
1173 limitation factors and their interactions with the CO₂ effect on vegetation photosynthesis by
1174 adding these factors (i.e., precipitation, soil moisture and TWS) into the regression models (see
1175 Table S3). The non-linear models considering the additional interaction effects of CO₂ and
1176 climate on vegetation growth generally showed slightly larger declining β trends than the linear
1177 models (Fig. S14). Results showed a relatively larger decrease in global β , after considering the
1178 impacts from soil moisture and TWS (Fig. S14 and Tables S2-S3). Moreover, the declining β
1179 trend was the largest among all of these thirty models when we considered the interactions
1180 between the CO₂ effect and water-limitation factors (Tables S2-S3), further supporting our
1181 finding about the limitation of water availability on global CFE.

1182 Overall, all thirty models showed a significantly different β trends between the satellite
1183 GPP proxies and the TRENDY GPP data (Fig. S14). More importantly, β significantly
1184 declined across all of these models from the period of 1982–1996 to the recent period (2001–
1185 2015, Fig. S15). These results indicated that the detected global declines in β were robust,
1186 independent of the various combinations of environmental and climate explanatory variables
1187 used for the analysis.

1188 **S6. Impacts of MAT, MAP and seasonal precipitation on vegetation photosynthesis**

1189 We also investigated the relative contributions of climatic and environmental factors (CO₂,
1190 MAT, VPD, Ndep, MAP and seasonal precipitation) to the increasing trend of vegetation
1191 photosynthesis in recent decades with multiple regression approaches (Fig. S17a). Similar with

1192 Eqs. (1) and (2), we used the following two equations to estimate the relative contributions
1193 from different climatic and environmental factors:

$$1194 \quad y = \beta(\text{CO}_2) + C_1(\text{MAT}) + C_2(\text{VPD}) + C_3(\text{Ndep}) + C_4(\text{MAP}) + C_5 + \varepsilon \quad (5)$$

$$1195 \quad y = \beta(\text{CO}_2) + C_1(\text{MAT}) + C_2(\text{VPD}) + C_3(\text{Ndep}) + \\ C_4(\text{Spring Pre}) + C_5(\text{Non-spring Pre}) + C_6 + \varepsilon \quad (6)$$

1196 Eq. (5) was used to estimate the contributions of CO₂, MAT, MAP, VPD and Ndep, while Eq.
1197 (6) was used to estimate the contributions of seasonal precipitation (divided into spring
1198 precipitation and non-spring precipitation). Similar to Eqs. (1) and (2), when calculating the
1199 regression coefficients here, we used the annual anomalies of these variables in the equations.

1200 Results showed that the rising CO₂ explained the largest contribution to the increasing
1201 trends of satellite observed GPP proxies ($59.5 \pm 26.6\%$), while atmospheric Ndep contributed
1202 the second largest part ($19.3 \pm 22.2\%$), which was consistent with the results from a previous
1203 study (15). Global increasing MAT also had positive impacts on vegetation photosynthesis at
1204 the global scale ($10.2 \pm 19.3\%$). The positive impact of temperature on global vegetation
1205 photosynthesis and growth was consistent with some previous studies (82). For example, the
1206 global average contribution from temperature on the GPP trend was estimated to be about
1207 13.07% (82). On the other hand, our result had some differences with another study (79),
1208 which found that global warming generally had negative impacts on the GPP trend. One
1209 possible reason for this divergence may be because our regression models included VPD into
1210 consideration while Haverd et al. (2020) did not. Given that global increasing VPD generally
1211 has negative impacts on vegetation growth during the recent decades (20), the exclusion of the
1212 VPD effect on GPP can substantially affect the derived temperature sensitivity of GPP.
1213 Excluding VPD in the analysis might amplify the negative impact of global warming on the
1214 GPP trend. Moreover, we argue that this divergence may be caused by the different GPP
1215 products (carbon-cycle models vs satellite products), climate variables (considering VPD and
1216 Ndep or not) and analysis methods (factorial simulation vs statistical methods) used in these
1217 studies. It should be noted that the global contributions of various climatic factors to GPP and
1218 LAI still diverge (81), even among the different process-based models (15), which need to be
1219 further investigated in the future.

1220 Global increasing in VPD had negative impacts on vegetation growth ($-4.5 \pm 18.0\%$),
1221 which was consistent with a recent study (20). Although MAP had no obvious effects ($0.2 \pm$
1222 13.4%), seasonal precipitation had significant impacts on vegetation photosynthesis. Results
1223 showed that the spring precipitation generally had positive effects on plant photosynthesis (5.7
1224 $\pm 12.6\%$), while non-spring precipitation had adverse impacts ($-5.4 \pm 11.9\%$). This result was
1225 consistent with the findings observed from dozens of temperate grassland experiments, which
1226 suggested that the spring and non-spring precipitation generally had positive and negative
1227 impacts on CFE respectively (36).

1228 We then included seasonal precipitation into the regression models to check the global
1229 trends of β , by replacing the annual total precipitation with seasonal precipitation. The annual
1230 precipitation was divided into four seasons (36): spring (March–May), summer (June–August),
1231 autumn (September–November) and winter (December–February). Temporal changes of β
1232 during 1982–2015 were estimated with 15-year moving windows using the following equation:

$$1233 \quad y = \beta(\text{CO}_2) + C_1(\text{MAT}) + C_2(\text{VPD}) + C_3(\text{Spring Pre}) + C_4(\text{Summer Pre}) \quad (7)$$

$$1234 \quad + C_5(\text{Autumn Pre}) + C_6(\text{Winter Pre}) + C_7 + \varepsilon$$

1234 We found a slightly larger decline of global β at a rate of $-0.95 \pm 0.13\% \text{ } 100 \text{ ppm}^{-1} \text{ y}^{-1}$ (p
1235 < 0.01 , Fig. S17b), which also confirmed the robustness of our results.

1236 S7. Uncertainty analysis

1237 We analyzed the uncertainties of the β time series. Three components of the uncertainty
1238 were considered in this analysis: 1) the uncertainty from original satellite data; 2) the
1239 uncertainty from the CDF fusion method; and 3) the uncertainty from the regression models.

1240 (1) Uncertainty from original satellite data

1241 Although the LTDR, GIMMS and MODIS products have extensively included the sensor
1242 post-launch calibration, bias corrections for systematic orbit shifts, cloud screening, sensor
1243 degradations and atmospheric corrections (59, 60), some uncertainties still remained (83, 84),
1244 especially during the earlier periods of AVHRR satellites (59, 60, 85). Quantifying the global
1245 uncertainties in AVHRR and MODIS products during the last four decades is a challenging
1246 task. To estimate the relative uncertainties of AVHRR and MODIS NIRv, here we followed the
1247 approach presented in a previous study (86). The method was based on the quantification of the
1248 noise of weekly NIRv data. We firstly derived the smoothed response of a time series for any
1249 single pixel, using a moving average filter with a span of 4 weeks. The deviations between the
1250 raw and smoothed time series were then calculated and interpreted as the noise, since we
1251 assumed that the responses of vegetation at the ecosystem-level were slow within one week,
1252 therefore any sudden changes were likely caused by noise rather than signals (86). We then
1253 normalized these deviations to relative uncertainties by dividing the peak values of the seasonal
1254 cycles. Fig. S18c shows an example of this approach. It should be noted that our assumption
1255 that any sudden changes beyond the smoothed curve at a weekly scale was noise could be
1256 compromised at finer spatial scales and shorter time scales. However, since our analyses were
1257 based on monthly scale at 1° resolution, we argued that this assumption was applicable for this
1258 study.

1259 During the whole period of NOAA satellites, two types of AVHRR instruments have been
1260 used, i.e., AVHRR/2 and AVHRR/3. AVHRR/2 instruments flew from July 1981 to November
1261 2000 onboard NOAA-7/9/11/14 satellites. AVHRR/3 instruments have flown since November
1262 2000 to present onboard NOAA-16/17/18/19 satellites. MODIS instruments have been in
1263 operation since December 1999 to present onboard Terra and Aqua. We applied the above
1264 introduced approach to estimate the uncertainties of satellite GPP proxies from AVHRR/2,

1265 AVHRR/3 and MODIS instruments (Fig. S18a, b&d). Results showed that the relative
1266 uncertainties of AVHRR/2 instruments were about 1.5 times larger than those of AVHRR/3
1267 and MODIS (Fig. S18d).

1268 The propagated uncertainties in the β time series (σ_{data}) due to the uncertainties of original
1269 satellite data ($\sigma_{\text{satellite}}$) were estimated based on Eq. (1) in the “Materials and Methods” section:

$$1270 \quad \sigma_{\text{data}} = \sqrt{\left(\frac{1}{\text{CO}_2} \cdot \sigma_{\text{satellite}}\right)^2} \quad (8)$$

1271 where σ operator refers to the standard error (SE), CO_2 represent the atmospheric CO_2
1272 concentration, and $\sigma_{\text{satellite}}$ are the uncertainties of satellite GPP proxies calculated from the
1273 previous approach.

1274 (2) Uncertainty from the CDF fusion method

1275 The CDF matching technique used to merge the AVHRR NIRv and MODIS NIRv, may
1276 also bring some uncertainties into the estimation of β . We quantified this uncertainty (σ_{CDF}) by
1277 calculating the global β during the 2001–2015 window using the original MODIS NIRv and
1278 the CDF-fitted MODIS NIRv, respectively:

$$1279 \quad \sigma_{\text{CDF}} = \sqrt{(\beta_{\text{original}} - \beta_{\text{CDF_fitted}})^2} \quad (9)$$

1280 where β_{original} represent the global β values calculated from the original MODIS NIRv data,
1281 while $\beta_{\text{CDF_fitted}}$ represent the global β values calculated from the CDF-fitted MODIS NIRv data.

1282 The result presented in Fig. S1c showed that the CDF matching approach had very little
1283 effects on the estimation of β , since this approach could maintain the original temporal trends
1284 of the NIRv time series (Fig. S1a&b).

1285 (3) Uncertainty from the regression models

1286 The regression models used to derive β also would bring some uncertainties (σ_{method}). To
1287 estimate this uncertainty, we used 500 bootstrap analyses (55), for each combination of
1288 different sources of satellite data, different moving window lengths, different land cover
1289 change masks, different definitions of growing seasons, and different combinations of climate
1290 and environmental factors. The uncertainties of the β time series were taken from all scenarios
1291 of these sensitivity tests.

1292 The overall uncertainties of the β time series were then calculated as:

$$1293 \quad \sigma_{\beta} = \sqrt{(\sigma_{\text{data}})^2 + (\sigma_{\text{CDF}})^2 + (\sigma_{\text{method}})^2} \quad (10)$$

1294 We applied this procedure to estimate the β uncertainties from satellite GPP proxies, the
1295 revised EC-LUE GPP and TRENDY GPP. The results are shown in Fig. S19. The global β
1296 estimated from satellite GPP proxies during 2001–2015 was $12.9 \pm 1.9\%$ 100 ppm^{-1} (median \pm
1297 SE), which was significantly smaller than that during 1982–1996, with a value of $21.8 \pm 3.4\%$
1298 100 ppm^{-1} (Fig. S19b). The global β during 2001–2015 calculated from the revised EC-LUE
1299 GPP also showed a significant decline compared to the period of 1982–1996. On the contrary,

1300 the global β from TRENDY GPP between these two periods showed only a slight decline.
 1301 These results indicated that the global declines of β in recent decades are robust and
 1302 statistically significant after considering the uncertainties from original satellite data, time
 1303 series fusion approach and multiple regression models. This uncertainty analysis methodology
 1304 was used to estimate the global β uncertainties. It was applied to the remote sensing datasets,
 1305 TRENDY GPP and regression methods, but not to other analyses in this study.

1306 **S8. Robustness of the calculation method**

1307 To test whether the global declining trends of β were affected by the regression methods,
 1308 we also calculated the temporal dynamics of β using an optimal fingerprint attribution method
 1309 (15). We used the simulation results from TRENDY to replace the contributions of climate and
 1310 land cover changes to GPP, similar to the direct regression methods introduced in the Methods
 1311 section. The optimal fingerprint attribution method can be expressed as:

$$1312 \quad y = \beta(\text{CO}_2) + C_1(\text{GPP}_{\text{climate}}) + C_2(\text{GPP}_{\text{LULC}}) + C_3 + \varepsilon \quad (11)$$

1313 where y represents the time series of the satellite GPP proxies, CO_2 represents the atmospheric
 1314 CO_2 concentration, $\text{GPP}_{\text{climate}}$ and GPP_{LULC} represent the contributions of climate and land
 1315 cover changes to GPP respectively, which were derived from the TRENDY GPP simulations.
 1316 For example, the GPP outputs from the TRENDY ‘S1’ scenario only included the CO_2
 1317 fertilization effects, while those from the ‘S2’ scenario considered both the impacts of CO_2 and
 1318 climate on vegetation; therefore we used the differences in GPP between the ‘S2’ and ‘S1’
 1319 scenarios as the contributions of climate factors, expressed as $\text{GPP}_{\text{climate}}$ in Eq. (11). We also
 1320 estimated the contributions of land cover change to GPP (GPP_{LULC}) using the differences
 1321 between the TRENDY ‘S3’ and ‘S2’ scenarios. β , C_1 , C_2 and C_3 represent regression
 1322 coefficients, and ε is the residual error term. Regression coefficient β was estimated using
 1323 maximum likelihood analysis.

1324 Based on this optimal fingerprint attribution method, we then calculated the temporal
 1325 dynamics of β based on three satellite GPP proxies with 15-year moving windows during
 1326 1982–2015. Using the simulation results of TRENDY to estimate the contributions of climate
 1327 and land cover changes to GPP, this method could alleviate the uncertainties of choosing
 1328 different indices and data to represent the climate variables and land use changes. Results
 1329 showed that β also had a significant declining trend at a rate of $-0.85 \pm 0.10\% \text{ } 100 \text{ ppm}^{-1} \text{ y}^{-1}$
 1330 (Fig. S20), which was similar with the results from the regression method and indicated the
 1331 robustness of the recent declines in global β on GPP.

1332 **S9. GPP data from a revised EC-LUE model**

1333 We used a long-term GPP time series from a revised eddy covariance-LUE (EC-LUE)
 1334 model (20, 87). LUE models generally consider the effects of temperature and water limitation
 1335 on GPP, although various regulation scalars have been used (88, 89). Previous LUE model-
 1336 based GPP data have generally ignored the direct effects of CO_2 on LUE (21), so β derived

1337 from these data is generally lower than that from the ESMS and the FACE experiments (13).
 1338 Compared with previous models, this revised EC-LUE model added a scaling factor to
 1339 represent the CFE on vegetation and therefore could be used to verify our estimates of β trends.
 1340 The approach to estimate GPP was based on the following equations (20):

$$1341 \quad \text{GPP} = (\varepsilon_{\text{sun}} \times \text{APAR}_{\text{sun}} + \varepsilon_{\text{shade}} \times \text{APAR}_{\text{shade}}) \times C_s \times \min(T_s, W_s) \quad (12)$$

$$1342 \quad C_s = \frac{C_i - \Gamma^*}{C_i + 2\Gamma^*} \quad (13)$$

1343 where APAR represents the absorbed PAR; ε represents the maximum LUE; sun and shade
 1344 represent the values of sunlit and shaded leaves, respectively; C_s , T_s and W_s represent the
 1345 regulation scalars representing the effects of atmospheric CO_2 , temperature and VPD on LUE;
 1346 min represents the minimum value of T_s and W_s . C_s was estimated following Eq. (9) (90, 91),
 1347 where Γ^* is the CO_2 compensation point in the absence of dark respiration, and C_i represents
 1348 the intercellular CO_2 concentration, which is the product of atmospheric CO_2 concentration (C_a)
 1349 and the ratio of leaf-internal to ambient CO_2 (χ):

$$1350 \quad C_i = C_a \times \chi \quad (14)$$

1351 χ is estimated by (92-94):

$$1352 \quad \chi = \frac{\gamma}{\gamma + \sqrt{\text{VPD}}} \quad (15)$$

$$1353 \quad \gamma = \sqrt{\frac{356.51K}{1.6\eta^*}} \quad (16)$$

1354 where K and η^* were derived from air temperature and several constant variables (95). The
 1355 CO_2 compensation point (Γ^*) was calibrated based on the GPP estimations at EC flux sites.
 1356 The detailed information can be found in (20).

1357 **S10. Satellite LAI data**

1358 We also used two long-term satellite-based LAI data sets to assess the temporal dynamics
 1359 of β . The first data set is the GIMMS-3g LAI products generated from an artificial neural
 1360 network (ANN) model and GIMMS-3g NDVI (96). Direct comparisons with field
 1361 measurements, indirect comparisons with other similar products and a statistical analysis with
 1362 climate variables have been used to evaluate the quality and applicability of this product (96).
 1363 Providing the global LAI dynamics during 1982–2015 at a spatial resolution of 8-km and a
 1364 temporal resolution of half-month, this product has been widely used in previous studies (15,
 1365 97, 98). Another long-term LAI product was derived from MODIS C6 data. This product used
 1366 the biome-specific look-up tables simulated by a radiative transfer model to estimate LAI from
 1367 MODIS C6 reflectance (99, 100). We then used the fusion LAI data that combined GIMMS
 1368 LAI during 1982–2000 and MODIS LAI during 2001–2015 through the CDF matching
 1369 approach (hereafter GIMMS+MODIS LAI).

1370 S11. Trends of β using GPP estimates at EC flux sites

1371 To test the β trends derived from satellite GPP proxies, we also used the long-term GPP
1372 estimates at 22 EC flux sites to derive an independent estimate of the temporal trends of β . For
1373 this scope we used the yearly GPP data from the FLUXNET 2015 dataset. In order to compute
1374 the β trend, even if we used the shortest window length (10-year), we need at least 14 years of
1375 uninterrupted observations. Following this criteria, we finally selected 22 flux sites for this
1376 analysis, see [Table S4](#). Based on the same regression approach (Eq. (1) and (2)), we estimated
1377 the β trends at these flux sites using the 10-year moving windows. The results are shown in [Fig.](#)
1378 [S23](#). Twenty out of the twenty-two sites showed declining trends of β , although with some
1379 variability in the magnitude ([Fig. S23a](#)). Overall, results from these 22 flux sites suggested a
1380 significantly declining trend of β at an average rate of $-0.70\% \text{ } 100 \text{ ppm}^{-1} \text{ y}^{-1}$ ($p < 0.001$), which
1381 was comparable to the results from satellite GPP proxies around these sites ([Fig. S23b](#)). The
1382 overall consistency between remote sensing data and flux sites observations indicates that the
1383 global decline of β is robust and coherent across multiple observations.

1384 S12. Trends of β using CCDAS GPP

1385 We also used a global long-term GPP dataset from the Carbon Cycle Data Assimilation
1386 System (CCDAS) system, which is totally independent of the remote sensing data (i.e.,
1387 AVHRR and MODIS). CCDAS is based on the Biosphere Energy Transfer HYdrology
1388 (BETHY) model coupled with the transport model TM2 and utilizes a variational method to
1389 optimize the model parameters and state variables by assimilating *in-situ* observations of
1390 atmospheric CO_2 concentration (*101*, *102*). In this analysis, we used the long-term GPP output
1391 (1982-2015) from an assimilation experiment (hereafter CCDAS GPP), which simultaneously
1392 assimilated the atmospheric CO_2 data and surface soil moisture data from ESA-CCI (version
1393 4.3, <https://www.esa-soilmoisture-cci.org>), similar to the SMOS soil moisture assimilation as
1394 done by (*103*) but in a longer period.

1395 Based on the CCDAS GPP, we calculated the temporal changes of global β based on the
1396 15-year moving windows. We found that the global β significantly decreased during 1982-
1397 2015 at a rate of $-0.62\% \text{ } 100 \text{ ppm}^{-1} \text{ y}^{-1}$ ($p < 0.01$, [Fig. S24](#)), consistent with our findings from
1398 satellite observations. This result from an independent dataset indicates the robustness of the
1399 global declines in β , and confirms our results.

1400 S13. TRENDY data

1401 We used GPP and LAI data (1982–2015) from multiple terrestrial carbon cycle models
1402 (TRENDY v6 ensemble (*14*)). Twelve models (CABLE, CLM4.5, DLEM, ISAM, JULES,
1403 LPJ-GUESS, LPJ-wsl, LPX-Bern, ORCHIDEE-MICT, ORCHIDEE, VEGAS and VISIT)
1404 were used. Seven of these models have considered the process of carbon-nitrogen (C-N)
1405 interactions (CABLE, CLM4.5, DLEM, ISAM, LPJ-GUESS, LPX-Bern and ORCHIDEE),
1406 while other remaining five models (JULES, LPJ, ORCHIDEE-MICT, VEGAS and VISIT) did

1407 not include the process of C-N interactions. It should be noted that the LAI outputs from the
1408 DLEM model are not available. Therefore, the LAI data from DLEM is not included in this
1409 analysis. A set of experimental simulations were performed and here we used the GPP and LAI
1410 outputs from four simulations to calculate the β factor: (S0) constant CO₂, climate and land
1411 cover change, (S1) varying CO₂ only, (S2) varying CO₂ and climate, (S3) varying CO₂, climate
1412 and land cover change. All data were resampled to a spatial resolution of 1° using the nearest
1413 neighbour method.

1414 Although these models may have discrepancies about CFE (Fig. S7), and may also have
1415 weakness to adequately capture the satellite observed LAI response to CO₂ (15), as well as to
1416 replicate the changes in CO₂ amplitude (104), they are state-of-the-art and currently used to
1417 quantify the global land carbon budget, and some of them are coupled into Earth system
1418 models for climate projection (1). Therefore, it is valuable to analyze whether these models
1419 could adequately capture or not the global declining β trends that we observed from satellite
1420 data, and to investigate the possible reasons. These analyses could shed new light on the future
1421 efforts for improving the global carbon cycle models and could be beneficial for reducing the
1422 uncertainties of land carbon storage estimates.

1423 **S14. Analysis of the decreases in foliar N and P concentrations**

1424 To attribute the global declines in β to the decreases of key foliar nutrients concentrations,
1425 we used three regional or global datasets of nitrogen (N) and phosphorus (P) concentrations.
1426 The first data set reported the ground-based observations of foliar N and P concentrations from
1427 410 European sites (Fig. S30) provided by the International Co-operative Programme on
1428 Assessment and Monitoring of Air Pollution Effects on Forests (ICP Forests). We used this
1429 data set to investigate the temporal trends of foliar N and P concentrations in recent decades.
1430 The second data set was the site-specific observations of foliar N and P concentrations across
1431 Europe (3846 samples, Fig. S32). To obtain this data set, we firstly collected 31274
1432 observations of key foliar nutrients (N and P) concentrations in Europe together with
1433 geolocation information. The data were collected from ICP Forests, a global plant trait
1434 database (TRY database) and 334 items previously published from the 1980s to the 2010s. We
1435 selected the observations based on tree species. Ten types of trees with more than 100
1436 observations were used (Fig. S32). Then the site-specific foliar trait observations of each tree
1437 species were calculated, resulting in 3846 class- and site-specific samples. Finally, we used a
1438 spatial linear mixed-effects model to identify the relationships of foliar N and P concentrations
1439 with the decreases in β . The decreases in β were used as the response variables, and tree
1440 species were used as random variables. Several potential explanatory variables were also
1441 included (MAT, MAP, foliar N and P concentrations). Since we used the spatial linear mixed-
1442 effects model, we included MAT and MAP as the explanatory variables to account for the
1443 foliar N and P distributions in response to climate background. In this model, we also added a
1444 Gaussian spatial correlation scheme to account for the potential within-group spatial

1445 autocorrelations. The third data set was the global atmospheric N and P deposition data during
1446 1980–2013 (57). The relationships of the global trends of N and P deposition with the trends of
1447 β were then investigated (Fig. S33).

1448 The global decreases in foliar nutrients concentrations could be an important reason for
1449 the global declining trends of β . The recent findings of global reductions in foliar N
1450 concentrations (22), as well as the significant decreases in both foliar N and P over European
1451 forests (Fig. S31), suggested that foliar N and P supply for vegetation photosynthesis in recent
1452 decades have likely diminished. Previous studies had found that plant photosynthetic capacity
1453 (carboxylation capacity V_{cmax} and electron transport capacity J_{max}) at standard temperature
1454 were positively correlated with foliar N and P (105, 106). Therefore, the decreases in foliar N
1455 and P could be a main constraint for vegetation photosynthesis, and therefore limit the global
1456 CO_2 fertilization effects. This hypothesis was consistent with several controlled experiments,
1457 which suggested that soil or foliar N and P availability generally have crucial impacts on CFE
1458 (10, 26, 30, 107, 108). For example, the recent study based on the AmazonFACE experiments
1459 suggested that the responses of Amazon forests to CO_2 fertilization were largely affected by P
1460 availability (108). Moreover, a recent data-driven study based on 138 experiments suggested
1461 that the strength of CO_2 fertilization on 90% of the global vegetation was primarily driven by N
1462 or P (30).

1463 A previous study found that the global foliar N had decreased by 9.8% from 1980 to 2017
1464 (i.e., $-0.26\% \text{ y}^{-1}$) (22). If we assumed that the linear relationship between plant photosynthetic
1465 capacity and foliar N concentrations (105) remained unchanged in recent decades, the
1466 declining trends of global β might be at least similar to the trend of foliar N, i.e., at a rate of
1467 $-0.26\% \text{ 100 ppm}^{-1} \text{ y}^{-1}$. This declining trends of β could be much larger after including the
1468 impacts of foliar P (106), which showed a much larger decrease than foliar N in European
1469 forests ($-0.55\% \text{ y}^{-1}$, Fig. S31). Therefore, most of the TRENDY models might not adequately
1470 represent the increasing nutrient limitation for photosynthesis, given that these models had
1471 rather small negative β trends (-0.06 to $-0.21\% \text{ 100 ppm}^{-1} \text{ y}^{-1}$, Fig. S28). Nevertheless, some
1472 models that have considered the foliar or soil nutrient constraints on vegetation growth showed
1473 larger declining rates of β . For example, CABLE, that used the CASA-CNP model to constrain
1474 the nutrients supply for plants, as well as global synthesis results (106) to relate V_{cmax} with
1475 foliar N and P (109), showed a relatively larger decrease in β compared to the multi-model
1476 mean value (Fig. S28). The models that included C-N cycle interactions to emulate nutrient
1477 constraints also showed larger declining rates of β (Fig. S34). On this aspect, we argued that
1478 additional efforts are required to improve the representation of nutrients constrains on
1479 photosynthesis in vegetation models. In addition, global mapping of foliar nutrients (N and P)
1480 as well as the investigation of their spatiotemporal characteristics could also be beneficial to
1481 forecast the future dynamics of the terrestrial carbon budget.

1482 Currently, the constraints of foliar nutrients on the response of vegetation photosynthesis
1483 to CO₂ have been mainly assessed with FACE experiments (10, 26, 30, 108). Plants in these
1484 experiments generally were exposed to two times ambient CO₂ concentration. However, the
1485 dynamic of atmospheric CO₂ concentration in the real environments is rather different from the
1486 one forced in FACE trials (more gradual and with lower concentration). Vegetation may slowly
1487 adapt to environmental constrains in N and P supplies, even if these adaptations are likely not
1488 sufficient to fully offset the limiting role of nutrients on CFE. This is confirmed by a 20-years
1489 long experiment (107), which also suggested that soil net N mineralization rates largely
1490 controlled the different responses of C₃ and C₄ plants to enhanced CO₂. Moreover, the models
1491 that included the C-N interactions to represent nutrient constraints generally showed larger β
1492 declines than other models (Fig. S34), which could indicate that the nutrient constrains on CFE
1493 also existed under the real environments.

1494 **S15. Sensitivity of GPP to TWS**

1495 To investigate the sensitivity of GPP to water availability, we used four independent TWS
1496 datasets derived from MERRA-2 (the modern-era retrospective analysis for research and
1497 applications, version 2) reanalysis data product, WaterGAP (Water Global Assessment and
1498 Prognosis) model outputs, ERA-Interim product, and GLDAS (Global Land Data Assimilation
1499 Systems) Noah v2.0 model, respectively. Previous studies have usually used precipitation,
1500 drought indices or soil moisture to represent the water available to vegetation. However, this
1501 view has been challenged by a recent study claiming that current carbon cycle models based on
1502 these traditional data may underestimate the response of vegetation to drought stress (32). TWS
1503 not only includes the water supply from soil moisture, but also considers groundwater, surface
1504 water, snow and water stored in the biosphere (32). The MERRA-2 data combine multiple
1505 ground, aircraft and satellite observations with a numerical prediction model and provide
1506 global gridded TWS estimates (110). To test the robustness of our analysis, the TWS data from
1507 a global hydrological model (WaterGAP (111)), a global atmospheric reanalysis product
1508 (ERA-Interim (112)) and a land surface model (GLDAS Noah v2.0 (113)) were also used in
1509 this analysis. It should be noted that the TWS data from ERA-Interim and GLDAS only
1510 included the total column soil moisture and snow water equivalent; and GLDAS TWS data
1511 only spanned from 1982 to 2010. We calculated the sensitivities of GPP to TWS data with 15-
1512 year moving windows using satellite GPP proxies and TRENDY 'S2' GPP data (Fig. S39) and
1513 also testified the results using a shorter window (i.e., 10-years) with MERRA-2 TWS data (Fig.
1514 S40). To conduct the comparison between satellite GPP proxies and TRENDY GPP, we firstly
1515 standardized the water sensitivities to the range of [-1 1] and then calculated the trends of
1516 these sensitivities using linear regressions. We then calculated the correlation between the
1517 slopes of the TWS sensitivities and the trends of β (Fig. S38).

1518 Temporal variations in water availability for plants may also play an important role in the
1519 declining β trends. We found that the sensitivity of satellite GPP proxies to TWS had

1520 significantly increasing trends in arid, temperate and dry tropical areas (Fig. S37). On the
1521 contrary, the sensitivities of TRENDY GPP to TWS were typically much lower, especially for
1522 the arid areas (Fig. S37a). For temperate and dry tropical areas, only few models (CABLE,
1523 DLEM, ISAM and ORCHIDEE) could reproduce the similar increasing GPP sensitivity trends
1524 derived from satellite GPP proxies, whereas the other models predict much smaller or negative
1525 trends of GPP sensitivities to TWS (Fig. S37b&c). Field experiments suggest that water
1526 availability for plants, especially the spring precipitation (36), has a crucial impacts on CO₂
1527 fertilization effects (35, 37). On this aspect, we argued that more efforts are needed to improve
1528 the understanding of the complex interplay between water availability, nutrients supply and
1529 rising CO₂ impacts on vegetation photosynthesis and carbon uptake.

1530 **S16. Analysis based on the Boreal Ecosystem Productivity Simulator (BEPS) model**

1531 Based on the BEPS model simulations, we analyzed the impact of N limitation on global
1532 CFE and the N-climate interactions on GPP trends. BEPS is a process-based model consisting
1533 of photosynthesis, energy balance, hydrological, and soil biogeochemical modules, which
1534 considers the coupling between terrestrial carbon, water, and nitrogen cycles (114). Driven by
1535 remotely sensed vegetation structural parameters, BEPS has been successfully used to estimate
1536 the CO₂ effects on global carbon sinks (114). The N limitation in BEPS model was achieved
1537 through the control of leaf N concentration on V_{cmax} . Dynamics of leaf N concentration was
1538 determined by leaf N storage, leaf biomass, and N uptake from the soil N pool, which is the
1539 sum of atmospheric N deposition and N mineralized through decomposition of soil carbon
1540 pools (115). In this study, we used the same model structure and forcing data sets with the
1541 previous study (114) to simulate the global yearly GPP during 1982–2015.

1542 In order to analyze the effect of N limitation on CFE, we performed four scenarios of
1543 simulations including: (I) all variables temporally invariant since 1982 and without N
1544 limitation, (II) only CO₂ temporally variant since 1982 and without N limitation, (III) all
1545 variables temporally invariant since 1982 and with N limitation, (IV) only CO₂ temporally
1546 variant since 1982 and with N limitation. Then based on the difference between scenarios II
1547 and I, we calculated the global β without considering the N limitation. Similarly, based on
1548 scenarios IV and III, we calculated global β after considering N limitation. We found that the
1549 CO₂ effects on GPP become smaller after considering the N limitation, in both arid areas and
1550 non-arid areas (Fig. S41a). This finding further confirmed our first hypothesis of the
1551 progressive nutrients limitations on global CFE.

1552 We also analyzed the N-climate interactive impacts on vegetation GPP. We further
1553 simulated global yearly GPP with other two scenarios: (V) temporally variant CO₂ and climate
1554 and without N limitation, (VI) temporally variant CO₂ and climate and with N limitation. Then
1555 the global GPP trends for these two scenarios during 1982–2015 were estimated, respectively.
1556 Results showed that the global GPP trends slightly increased after considering the N-climate
1557 interactions (Fig. S41b). However, after including the N-climate interactions, the GPP trends in

1558 arid areas were reduced, in contrast to the trends in non-arid areas (Fig. S41b). This divergence
1559 may be because the drying trends of soil moisture in arid areas (116) had possibly reduced
1560 plant nutrient availability, e.g., exacerbated the N limitation on vegetation growth by reducing
1561 the nutrients decomposition and diffusion in soils (37). This finding suggested that not only N
1562 limitation or water limitation, but also the complex interactions between them could have
1563 strong impacts on global CFE, which need comprehensive investigation in the future.

1564 **S17. Caveats and potential missing mechanisms**

1565 There are still some potential uncertainties in our analysis. Firstly, satellite NIR_V is a
1566 proxy and not a real measurement of GPP. Nonetheless, NIR_V is a better proxy for GPP than
1567 traditional VIs, because it could partly eliminate the saturation of VIs by adding the NIR
1568 reflectance term (18); and it could therefore capture large fractions of the GPP variations both
1569 in space and time (approximately 70%–80%, Figs. S2–S4). Because the relationship between
1570 NIR_V and GPP is linear (18), there should be no large differences in the relative β trends
1571 between NIR_V and GPP. Moreover, we also used a LUE-based GPP data set to verify the
1572 results we identified from NIR_V (Fig. S21), confirming our findings. Secondly, the regression
1573 method for estimating β could not fully explain the temporal variations of NIR_V or GPP (Table
1574 S2 & S3), which may introduce some uncertainties. This caveat may not affect the significant
1575 differences in β trends between satellite GPP proxies and TRENDY GPP, because we used the
1576 same regression approach to estimate β from NIR_V and TRENDY GPP, and also calculated β
1577 with an optimal fingerprint attribution method to testify the robustness of our results (Fig. S20).
1578 Thirdly, there are some slight differences in the β trends between the results derived from the
1579 TRENDY ‘S1’ GPP and TRENDY ‘S2’ GPP (Fig. 2d & Fig. S29). This may be partly because
1580 the climate factors (e.g., temperature and precipitation) in ‘S1’ scenarios are set to the values of
1581 the start year (i.e., 1860); therefore the interactions between climate change and CO_2
1582 fertilization are missing in the GPP simulations of ‘S1’ scenarios. These caveats, therefore,
1583 should not affect the robustness of the declining β trends.

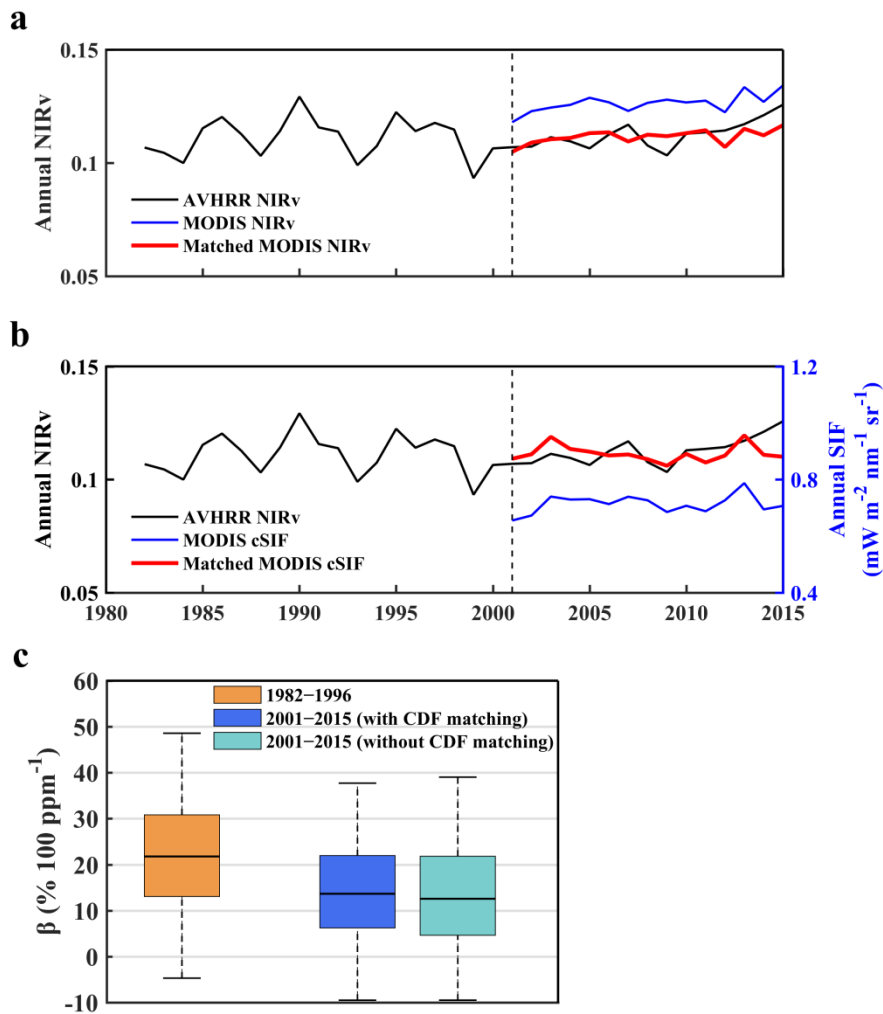
1584 Besides, all the datasets used in this analysis, either from the satellite observations or from
1585 the EC flux sites, are estimated products using certain methods, assumptions or parameters
1586 (117), e.g. the separation of GPP from measured NEE at flux sites. At present we still cannot
1587 directly measure GPP at large scales, but only at leaf scales under certain artificial conditions
1588 using gas exchange chambers (118). However, since there is no gold standard dataset for large-
1589 scale GPP estimation, we used several different sources of GPP estimates (e.g., NIR_V from
1590 AVHRR and MODIS, SIF, LUE models based GPP and flux sites based GPP) to verify the
1591 robustness of our findings.

1592 The two possible explanations for the global decreases of β may have some limitations.
1593 Firstly, the observations of foliar N and P concentrations we used to conduct the spatial mixed-
1594 effects model analysis were restricted to Europe, owing to data availability. Secondly, the TWS
1595 data sets used in this analysis were derived from the model outputs, because the TWS data

1596 from satellite observations (the Gravity Recovery and Climate Experiment, GRACE) only
1597 started from 2002 (32), which was not long enough to calculate the sensitivities of GPP to
1598 TWS using the 15-year moving windows.

1599 We did not explicitly consider other potential factors that may have impacts on the
1600 temporal dynamics of β , for example, forest age (40), the climate extremes including droughts
1601 (119-121), heat waves (122) and El Niño (123, 124), and large anomalous events like Pinatubo
1602 eruption (125). These events may also affect the temporal trends of β . However, their impacts
1603 on vegetation may have been partially expressed by the changes of temperature, indices of
1604 water limitation or radiation, which have been comprehensively taken into consideration in our
1605 methods when calculating β .
1606

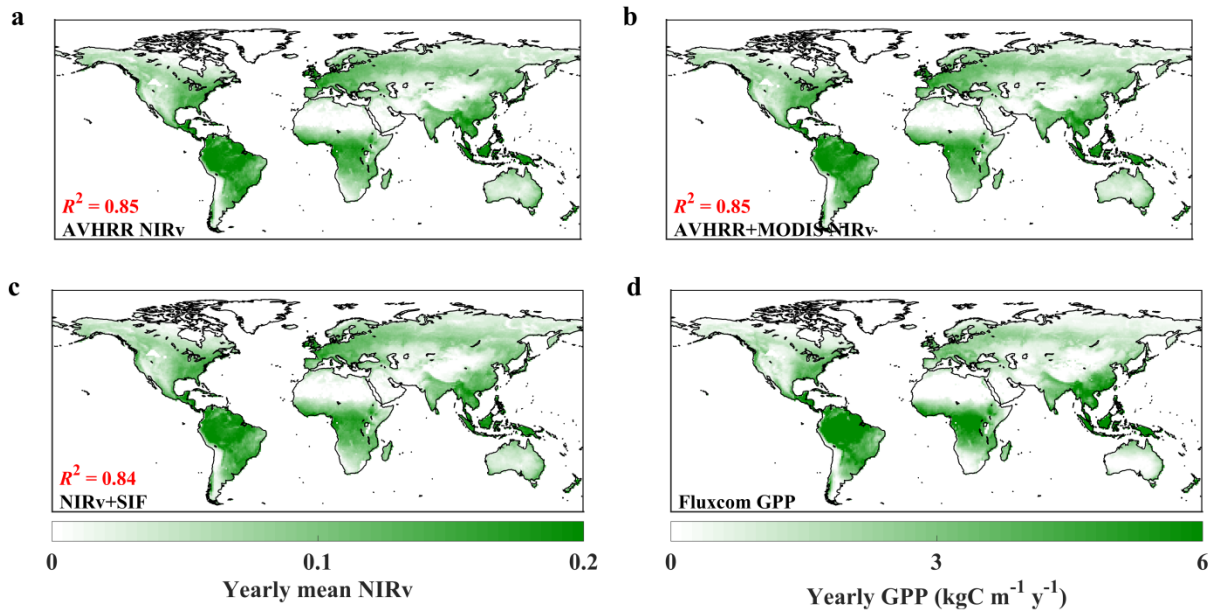
1607



1608

1609 **Fig. S1. The cumulative distribution frequency (CDF) matching approach. a-b: a fusion**
 1610 **example of the (a) AVHRR NIR_v and MODIS NIR_v; (b) AVHRR NIR_v and MODIS cSIF**
 1611 **through the cumulative distribution frequency (CDF) matching approach.** We chose the
 1612 pixel near 30°N and 120°E as the example. Firstly, we used the 0th, 5th, 10th, 25th, 50th, 75th,
 1613 90th, 95th and 100th percentiles of the monthly AVHRR NIR_v and MODIS NIR_v data during
 1614 2001–2015 to divide the cumulative distribution into eight segments. Then eight linear
 1615 regressions of these different segments were conducted to adjust the MODIS NIR_v to AVHRR
 1616 NIR_v. Similar fusion method was used to merge the AVHRR NIR_v and MODIS cSIF. This
 1617 fusion method only adjusted the magnitude of different data but maintained their temporal
 1618 trends. **c,** Global β calculated from different data (excluded the non-vegetated areas and
 1619 masked with the land cover change mask). The yellow bar represents the result calculated from
 1620 the 1982–1996 window based on AVHRR NIR_v data. The blue and cyan boxplots represent
 1621 the global β calculated from the 2001–2015 window based on the CDF-fitted MODIS NIR_v
 1622 data and the original MODIS NIR_v data without CDF matching, respectively. Boxes represent
 1623 the interquartile ranges of the β values (solid lines represent the median value), and whiskers
 1624 extend to one times the interquartile range.

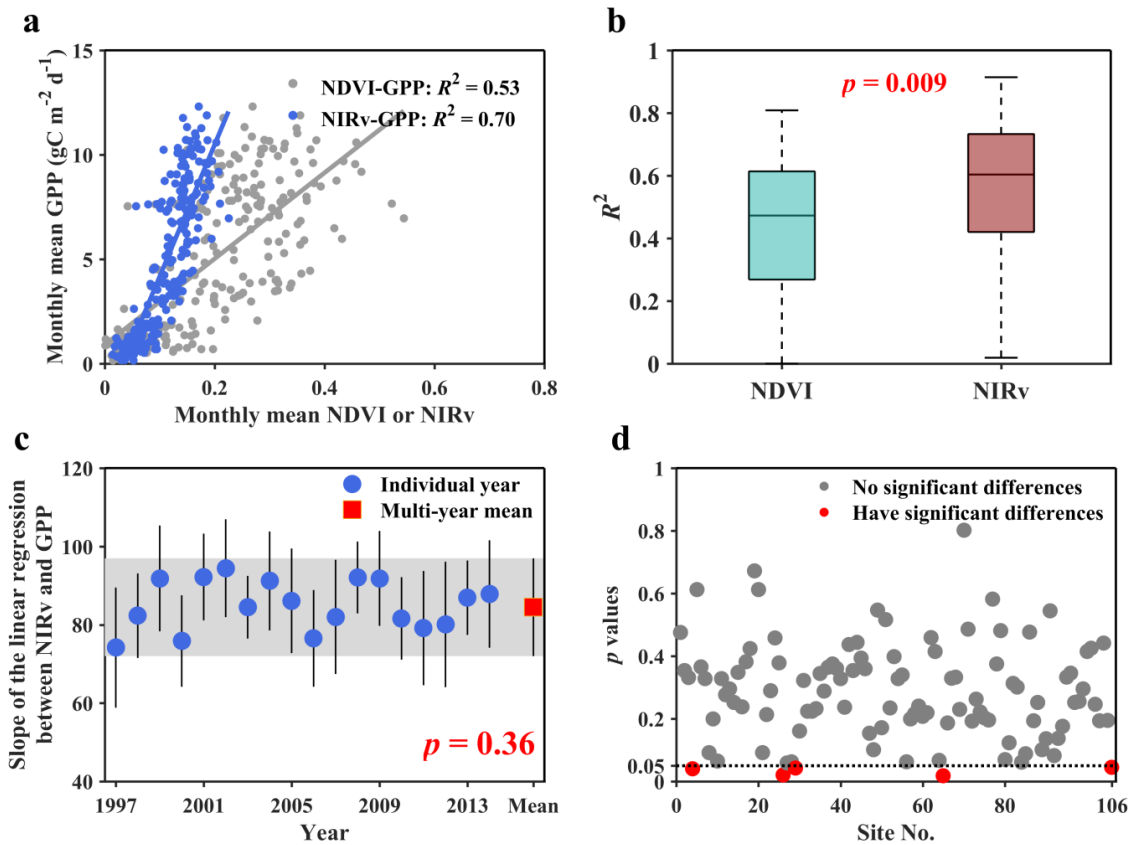
1625



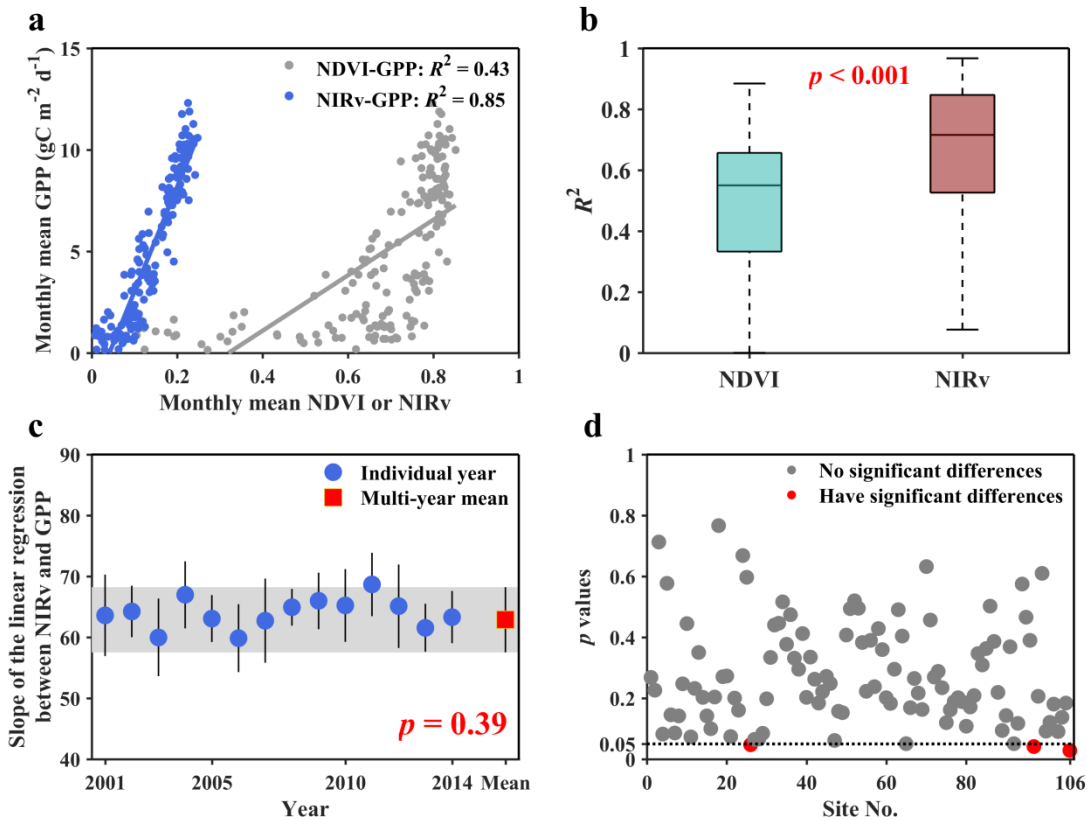
1626

1627 **Fig. S2. Global distribution of yearly (a) AVHRR NIR_v, (b) AVHRR+MODIS NIR_v, (c)**
 1628 **NIR_v+SIF and (d) Fluxcom GPP.** We used the yearly mean NIR_v and GPP during 1982–
 1629 2015. The global GPP data were obtained from the Fluxcom upscaling approach based on
 1630 observations from flux sites and meteorology parameters from CRUNCEP. Multi-year mean
 1631 GPP were calculated based on three different machine learning methods. R^2 values between
 1632 different NIR_v data with Fluxcom GPP were then calculated and marked in red. The spatial
 1633 resolution is 1°. Panels (a-c) share the same colour legend.

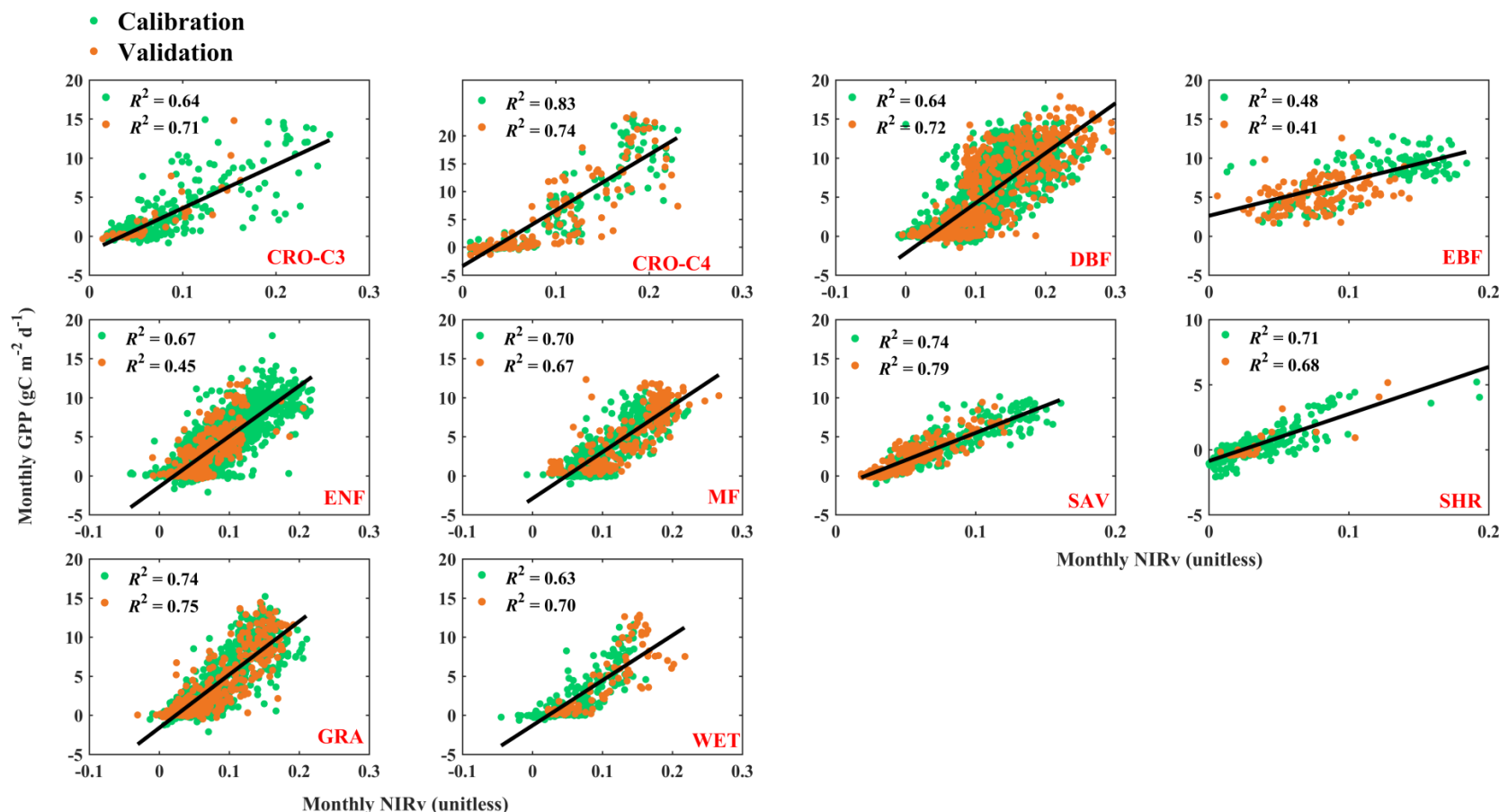
1634



1635
 1636 **Fig. S3. Relationship between AVHRR NIRv and GPP.** a, Relationship between monthly
 1637 NDVI or NIRv with monthly GPP estimates from an EC flux site (BE-Vie, mixed forest). The
 1638 monthly NDVI and NIRv were calculated as the average value of all AVHRR pixels
 1639 intersecting a 5-km-diameter circle centered at the latitude and longitude of the site. b,
 1640 Boxplots of the R^2 values between monthly NDVI or NIRv with monthly GPP estimates from
 1641 106 EC flux sites (Table S4). We used the sites which have more than 5-years data. The
 1642 difference significance between these R^2 values (NDVI-GPP vs NIRv-GPP) was determined
 1643 using Wilcoxon rank sum test in R (version 3.4.3). c, Individual yearly slopes between NIRv
 1644 and GPP at the BE-Vie site. The slope of each specific year was firstly calculated and the
 1645 multi-year mean slope was then calculated. The error bars and the shaded area represent
 1646 standard errors (SEs) of the means ($n = 18$). The difference significance between these
 1647 individual yearly slopes was determined using one-way analysis of variance (one-way
 1648 ANOVA) test and marked in red. d, The difference significance at all of these 106 EC flux
 1649 sites.

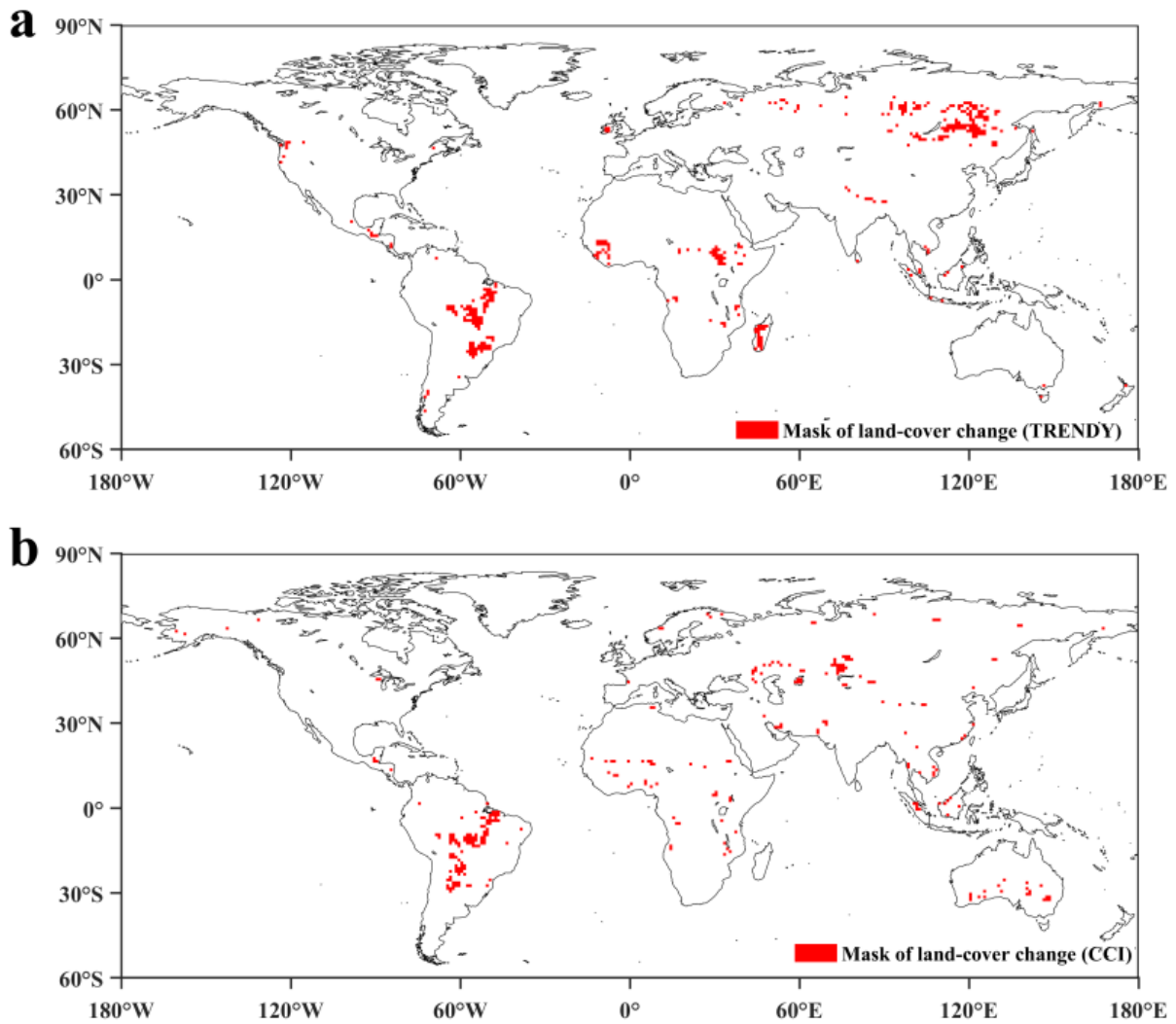


1650
 1651 **Fig. S4. Relationship between MODIS NIRv and GPP.** a, Relationship between monthly
 1652 NDVI or NIRv with monthly GPP estimates from an EC flux site (BE-Vie, mixed forest). The
 1653 monthly NDVI and NIRv were calculated as the average value of all MODIS pixels
 1654 intersecting a 1-km-diameter circle centered at the latitude and longitude of the site. b,
 1655 Boxplots of the R^2 values between monthly NDVI or NIRv with monthly GPP estimates from
 1656 106 EC flux sites (Table S4). We used the sites which have more than 5-years data. The
 1657 difference significance between these R^2 values (NDVI-GPP vs NIRv-GPP) was determined
 1658 using Wilcoxon rank sum test in R (version 3.4.3). c, Individual yearly slopes between NIRv
 1659 and GPP at the BE-Vie site. The slope of each specific year was firstly calculated and the
 1660 multi-year mean slope was then calculated. The error bars and the shaded area represent
 1661 standard errors (SEs) of the means ($n = 14$). The difference significance between these
 1662 individual yearly slopes was determined using one-way analysis of variance (one-way
 1663 ANOVA) test and marked in red. d, The difference significance at all of these 106 EC flux
 1664 sites.
 1665

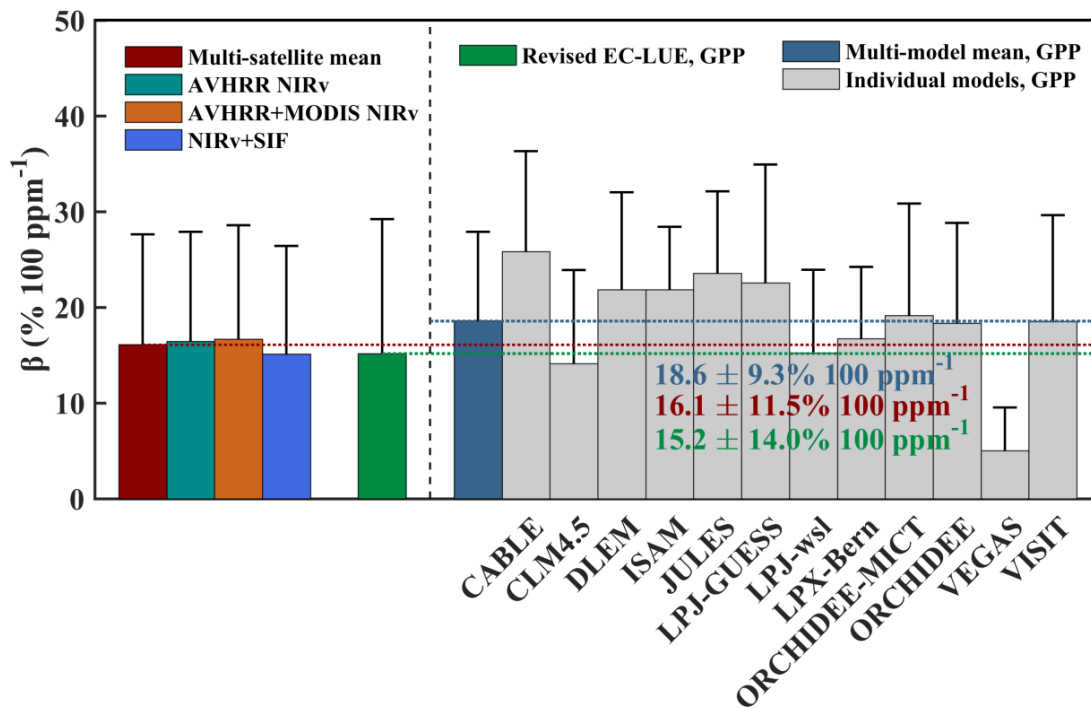


1666
1667
1668
1669
1670
1671

Fig. S5. Scatter plots between monthly AVHRR NIRv and flux tower GPP for ten different vegetation types. The green dots represent the calibration data, whereas the orange dots represent the validation data. The solid black lines in each panel represent the linear regressions between NIRv and GPP. The R^2 values between NIRv and GPP for both the calibration and validation data are presented in the up-left corner of each panel. CRO-C3, C₃ crop; CRO-C4, C₄ crop; DBF, broadleaved deciduous forest; EBF, evergreen broadleaf forest; ENF, evergreen needleleaf forest; MF, mixed forest; SAV, savannas; SHR, shrubland; GRA, grassland; WET, wetland.



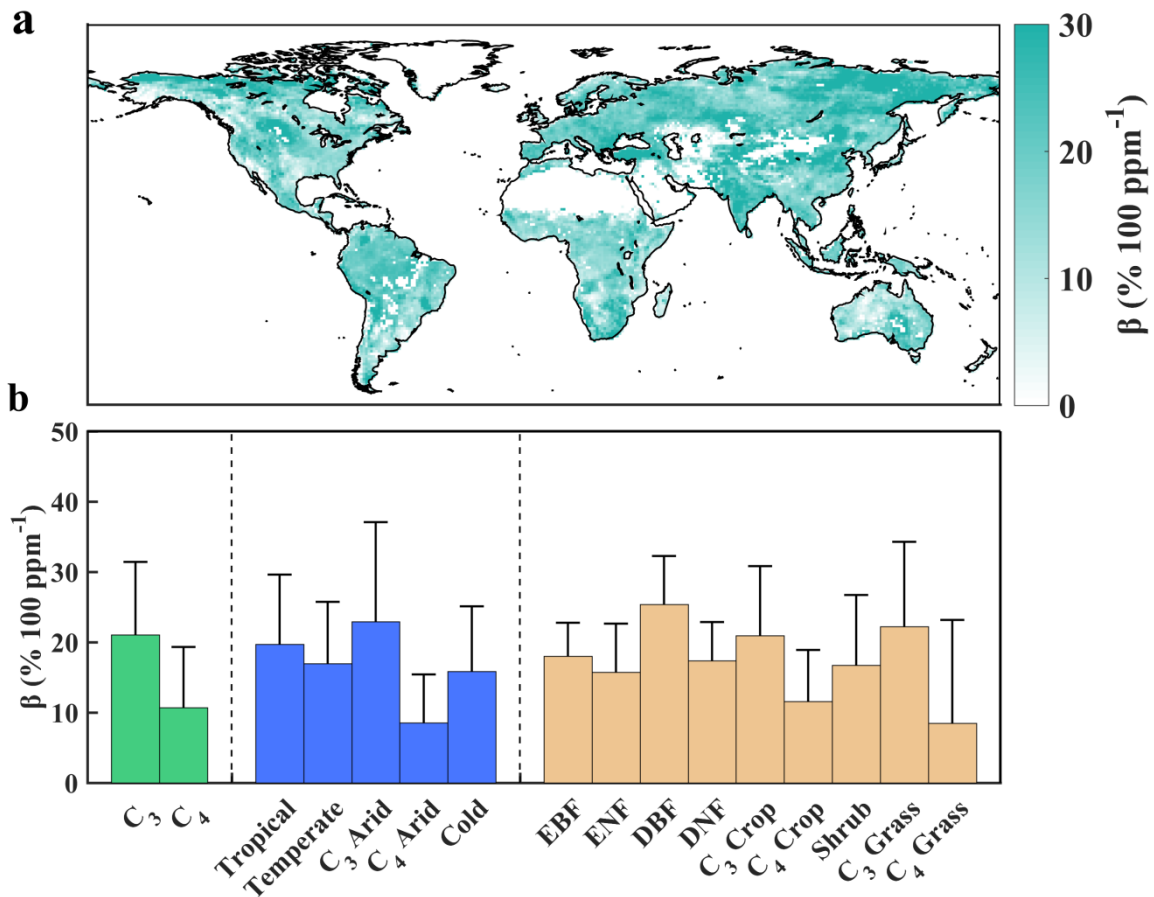
1672
 1673 **Fig. S6. Masks of land cover change: a, from the land use product used in TRENDY; b,**
 1674 **from the CCI land cover product.** In order to reduce the effects of land cover change on the
 1675 temporal trends of β , we made the masks of land cover change. Two data sets were used: the
 1676 land use harmonization (LUH2 v2h) used in TRENDY models and the CCI land cover data. If
 1677 the area of changed land cover was $>20\%$ of the total area in each 1° pixel, the pixel was
 1678 marked in red and excluded from this analysis. For consistency with the TRENDY models, we
 1679 used the mask based on LUH2 data in the following analysis.
 1680



1681

1682 **Fig. S7. Absolute values of β for the period 1982–2015 from satellite GPP proxies, LUE-**
 1683 **based GPP, and TRENDY GPP.** We calculated β of the period 1982–2015 for satellite GPP
 1684 proxies and the revised EC-LUE GPP using non-linear statistical methods (Eq. (2)). β from
 1685 TRENDY GPP was calculated using the process-based methods (Eq. (3)). The error bars
 1686 represent the standard deviations (SDs) of all the pixels ($n = 12850$). The horizontal dotted
 1687 lines are used to aid comparisons with the results from TRENDY models.
 1688

1689



1690

1691

1692

1693

1694

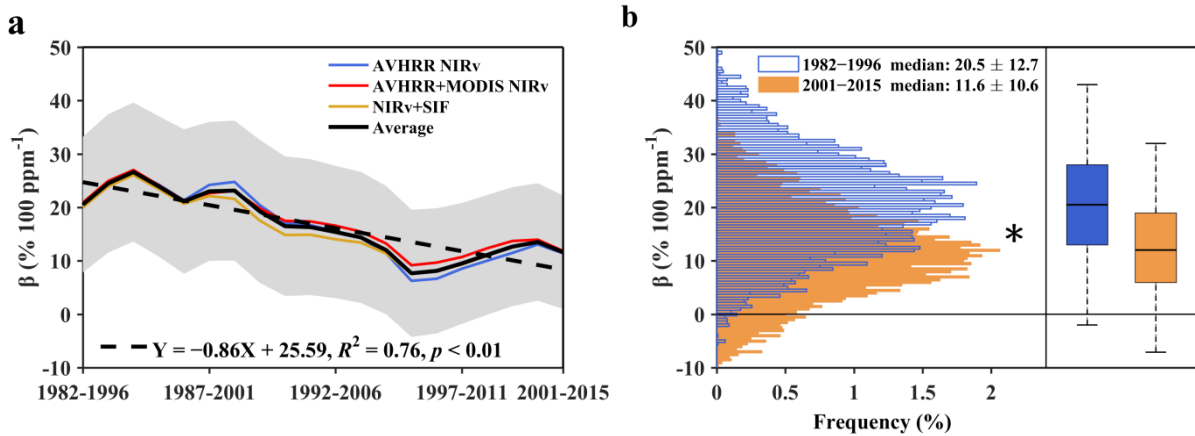
1695

1696

1697

Fig. S8. Global distributions of β (a) and their variations across different vegetation physiology types (C₃ or C₄), climate zones, and biome types (b). We calculated β for the period 1982–2015 from satellite GPP proxies using non-linear statistical regressions (Eqs. (2)). The error bars represent the standard deviations (SDs). EBF, evergreen broadleaf forest; ENF, evergreen needleleaf forest; DBF, deciduous broadleaf forest; DNF, deciduous needleleaf forest.

1698

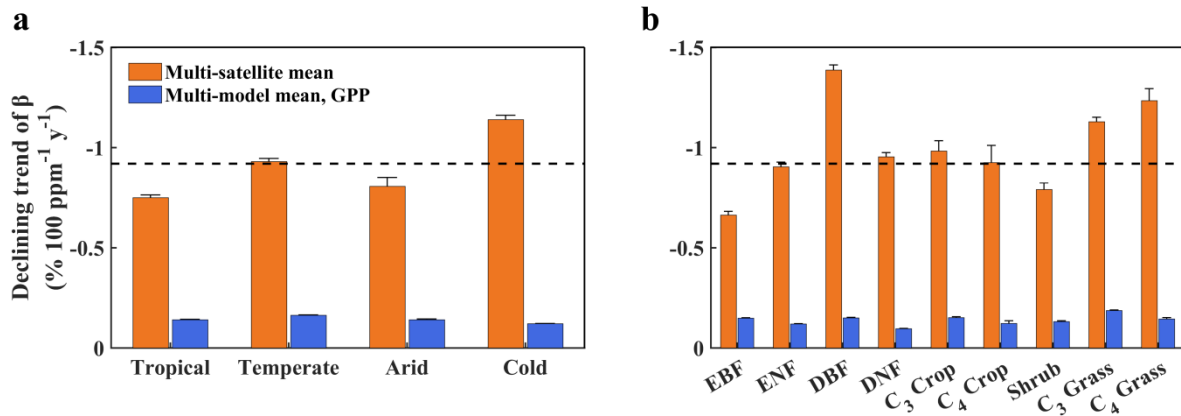


1699

1700 **Fig. S9. Decrease in global β after excluding the crop areas.** **a**, Temporal changes of β for
 1701 three satellite GPP proxies during 1982–2015 with 15-year moving windows. The solid black
 1702 line indicates the average of these three data sets. The grey area indicates one standard
 1703 deviation (SD) either side of the mean ($n = 7569$). The dashed line indicates the linear
 1704 regression. The trend and statistical significance (p value) of β time series were estimated using
 1705 a nonparametric trend test (Mann-Kendall test). **b**, Histogram distribution of β across all pixels
 1706 in two 15-year periods (1982–1996 and 2001–2015, left panel). β was the average of these
 1707 three satellite GPP proxies. In the right panel, boxes represent the interquartile ranges of the β
 1708 values (solid lines represent the median value), and whiskers extend to one times the
 1709 interquartile range. Median β of these two periods and their SDs were marked atop. The
 1710 asterisk indicates a significantly different β between these two periods using a two-sample
 1711 Kolmogorov-Smirnov test at $p < 0.01$.

1712

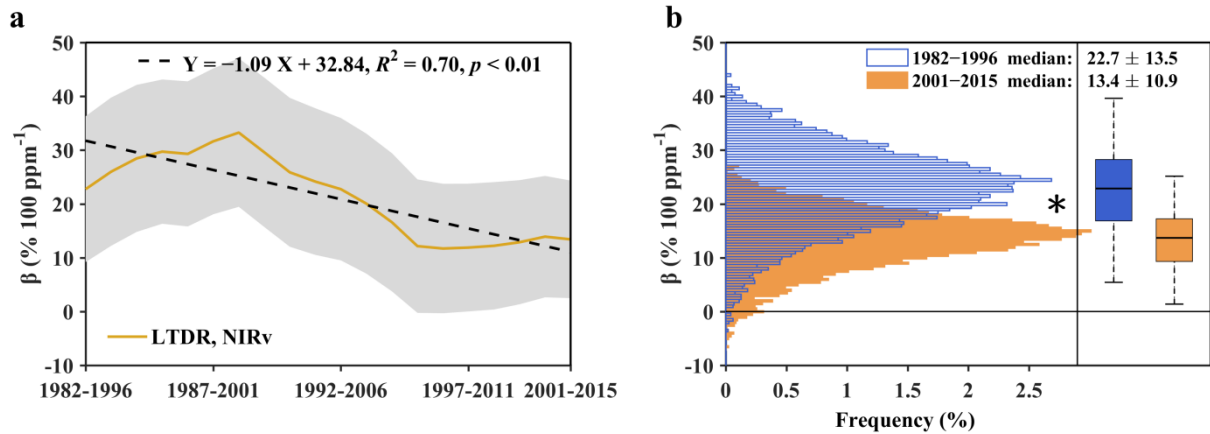
1713



1714

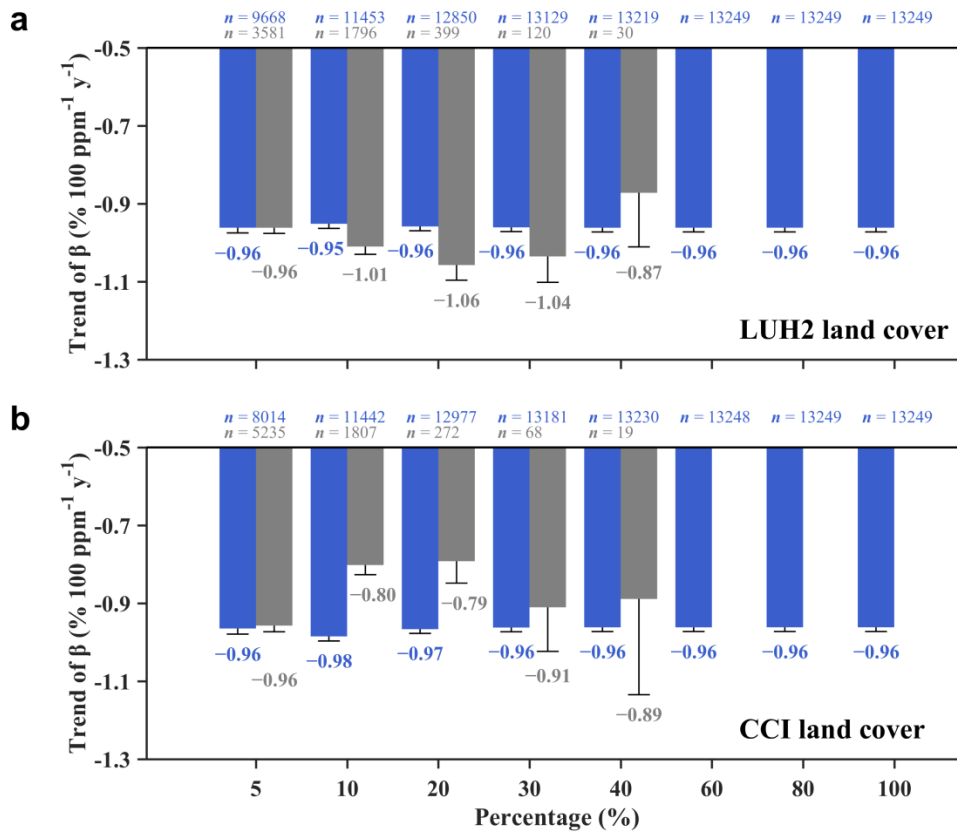
1715 **Fig. S10. Declining trends of β across (a) different climate zones and (b) different land**
 1716 **cover types.** Trends of β were derived from two different data sets (i.e., satellite GPP proxies
 1717 and TRENDY GPP) using 15-year moving windows. The climate zones were defined using the
 1718 Köppen-Geiger classification. The land cover types were derived from the CCI land cover
 1719 product. The horizontal dotted lines represent the global median value of the declining trends
 1720 in β . The error bars represent standard errors (SEs) of the means. EBF, evergreen broadleaf
 1721 forest; ENF, evergreen needleleaf forest; DBF, deciduous broadleaf forest; DNF, deciduous
 1722 needleleaf forest.

1723



1724
 1725 **Fig. S11. Temporal dynamics of β calculated from the LTDR NIRv.** a, Temporal changes
 1726 of β during 1982–2015 estimated with 15-year moving windows from the LTDR NIRv. The
 1727 dashed line indicates the linear regression. The grey area indicates one standard deviation (SD)
 1728 either side of the mean ($n = 12850$). The trends and statistical significances (p value) of the β
 1729 time series were estimated using Mann-Kendall test. b, The histogram distribution of β across
 1730 all pixels in two 15-years periods (1982–1996 and 2001–2015) for the LTDR NIRv. In the
 1731 right panel, boxes represent the interquartile ranges of the β values (solid lines represent the
 1732 median value), and whiskers extend to one times the interquartile range. Median β of these two
 1733 periods and their SDs were marked atop. The asterisks indicate a significantly different β
 1734 between the two periods using a two-sample Kolmogorov-Smirnov test at $p < 0.01$.

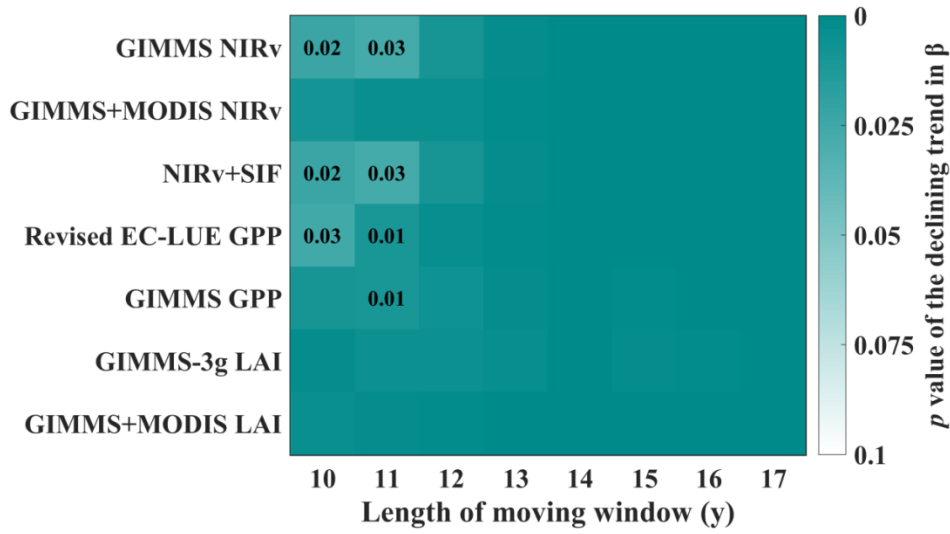
1735



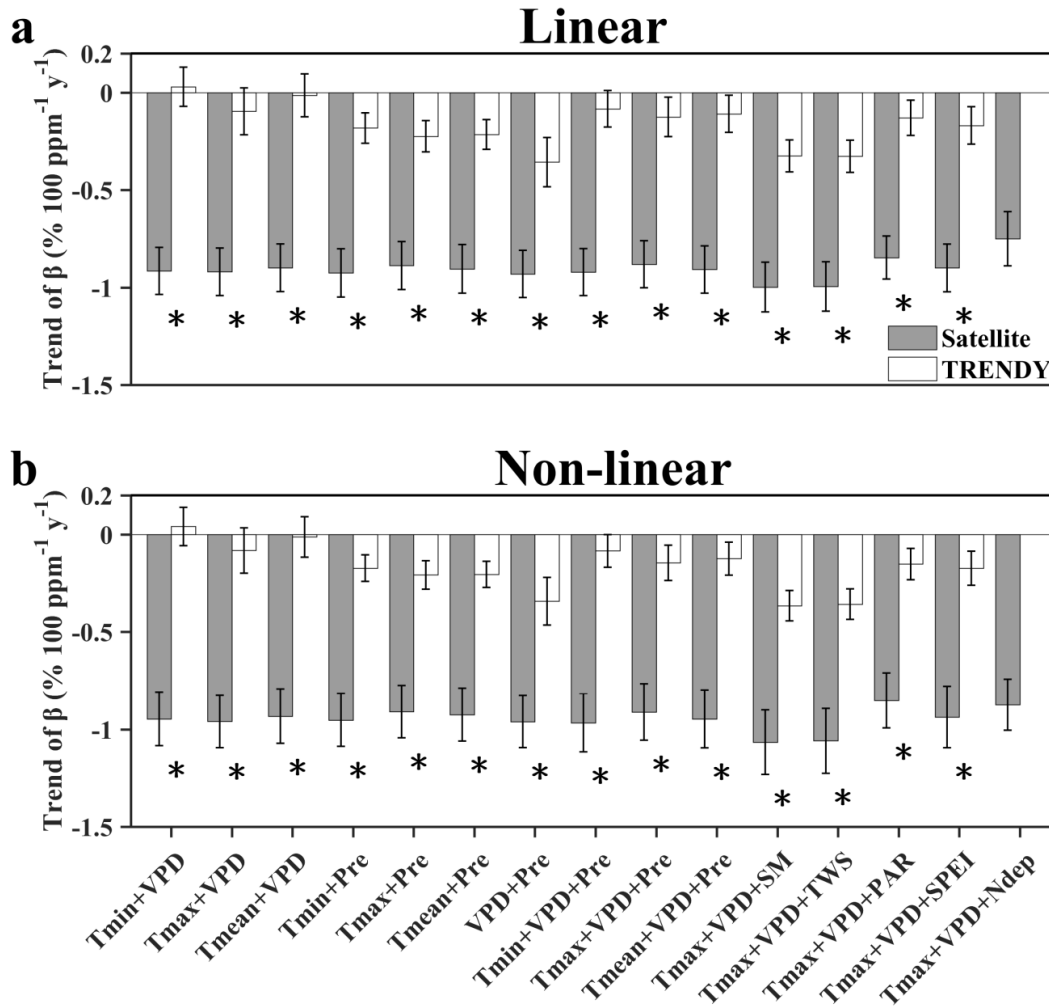
1736

1737 **Fig. S12. Trends of β using various masks of land cover changes: a, based on LUH2 data;**
 1738 **b, based on CCI data.** If the area of changed land cover was larger than the set values (i.e.,
 1739 from 5% to 100%, listed in the x-axis) of the total area in each 1° pixel, the pixel was excluded
 1740 from this analysis. We calculated β for satellite GPP proxies pixel by pixel with 15-year
 1741 moving windows. The trends of β time series were estimated using the Mann-Kendall test. The
 1742 blue bars represent the results for the remaining pixels and the grey bars represent the results
 1743 for the excluded pixels. The number of the remaining pixels and the excluded pixels for each
 1744 case was marked atop of the bars. The median decreases of β according to each scenario are
 1745 marked below each bar. The error bars represent standard errors (SEs) of the means.

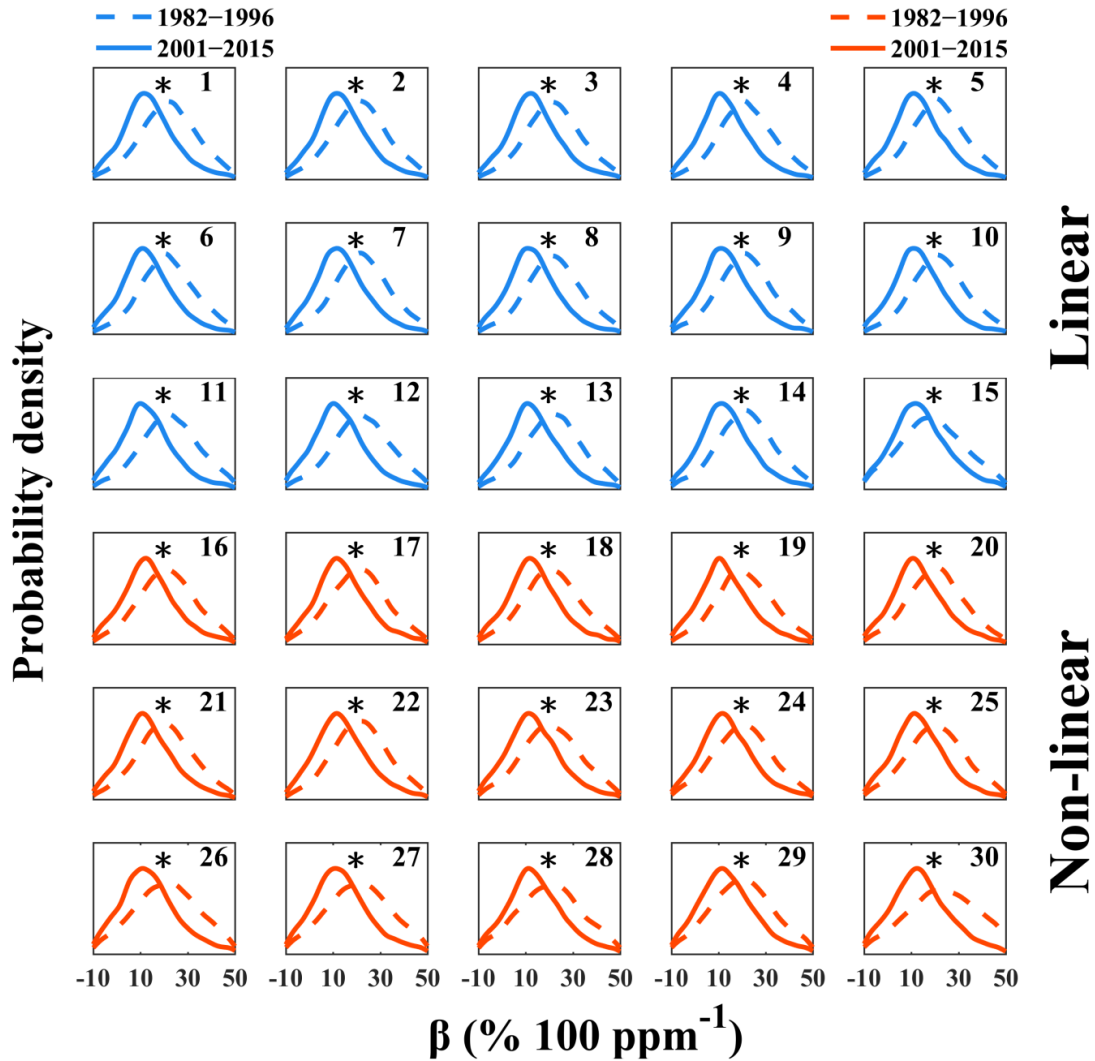
1746



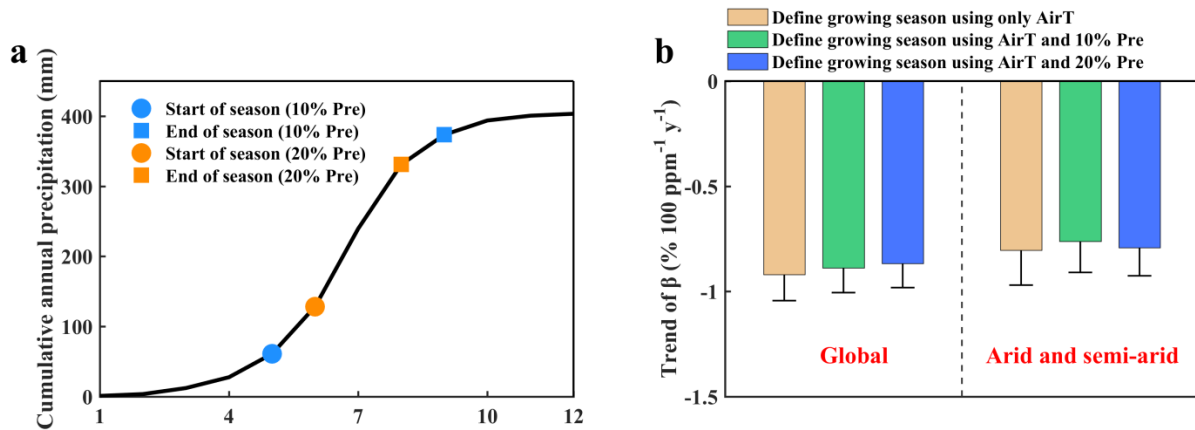
1747
 1748 **Fig. S13. P values of the declining trends in β for different lengths of moving window.**
 1749 Right y-axis represents the p values of β trends for satellite GPP proxies, LUE-based GPP and
 1750 satellite leaf area index (LAI). β was calculated using regression methods with different lengths
 1751 of moving window. The statistical significances (p values) of β time series were then estimated
 1752 using the Mann-Kendall test. All these scenarios have significantly declining trends. P values
 1753 smaller than 0.01 are not shown.
 1754



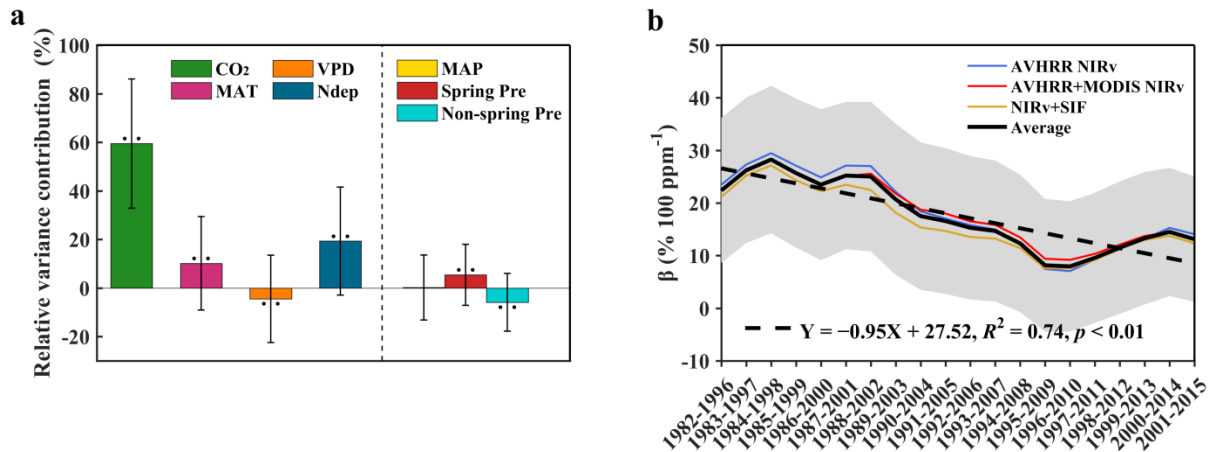
1755
 1756 **Fig. S14. Trends of β using various combinations of explanatory variables with linear (a)**
 1757 **and non-linear (b) regression for satellite GPP proxies and TRENDY GPP.** The non-linear
 1758 regression approaches considered the interaction effects of CO_2 with climatic and
 1759 environmental factors. We calculated β for three satellite GPP proxies and TRENDY GPP
 1760 pixel by pixel with 15-year moving windows using various combinations of explanatory
 1761 variables (x-axis). It should be noted that the model ('Tmax+VPD+Ndep') results for
 1762 TRENDY GPP are not calculated, because the GPP simulations in TRENDY do not include
 1763 the impacts of atmospheric Ndep. For each data set, we first calculated the global median β for
 1764 every moving window during 1982–2015. Then the trends and their standard errors (SEs) for
 1765 the β time series were estimated. Detailed results are presented in [Tables S2 & S3](#). The error
 1766 bars represent SEs. The asterisks indicate significantly different trends of β between the
 1767 satellite GPP proxies and TRENDY GPP using a two-sample Kolmogorov-Smirnov test at $p <$
 1768 0.01.
 1769



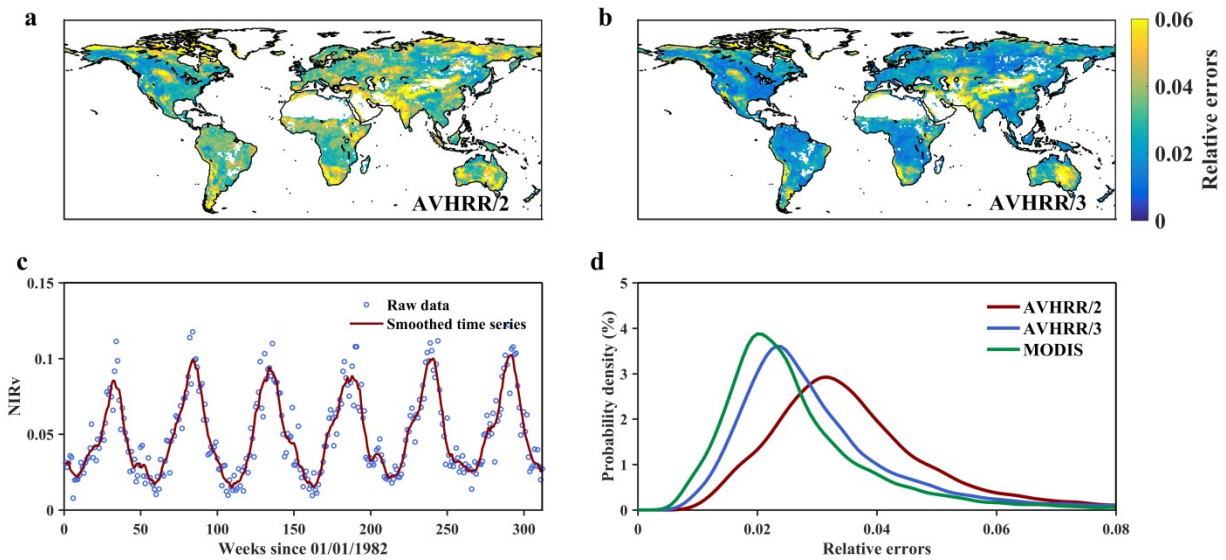
1770
1771 **Fig. S15. Probability density of β in two 15-year windows (1982–1996 and 2001–2015)**
1772 **using various combinations of explanatory variables with linear and non-linear**
1773 **regressions for satellite GPP proxies.** We calculated β for three satellite GPP proxies pixel by
1774 pixel with 15-year moving windows using various combinations of explanatory variables
1775 (overall thirty models). Detailed information of the thirty models is described in [Tables S2 &](#)
1776 [S3](#). The probability densities of β in the two 15-year windows based on these thirty models
1777 were then calculated using kernel distribution estimates. The numbers of the models are
1778 labelled in the upper-right corner of each panel. The asterisks indicate a significantly different
1779 β between these two windows using a two-sample Kolmogorov-Smirnov test at $p < 0.01$.
1780



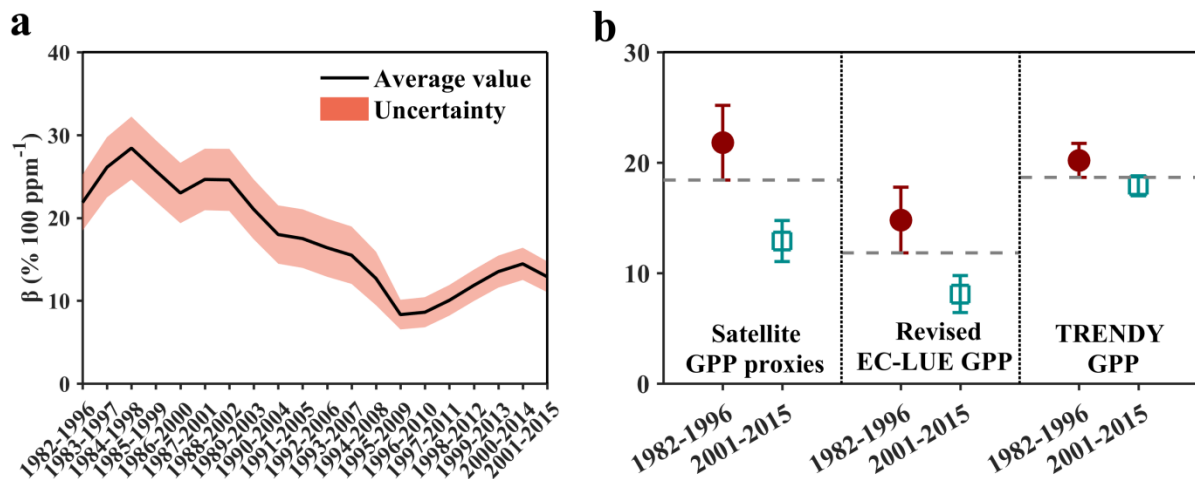
1781
 1782 **Fig. S16. Definition of the growing season using precipitation thresholds (a) and their**
 1783 **impacts on the global trends of β (b).** **a**, An example of the definition of the growing season
 1784 using different precipitation thresholds. “10% Pre” means that the start of the season was
 1785 defined as the date when the cumulative precipitation exceeded 10% of the annual total rainfall
 1786 for a given pixel, while the end of the season was defined as the date when the cumulative
 1787 precipitation exceeded 90% of the annual total rainfall. A similar definition was applied for the
 1788 “20% Pre”. **b**, Impacts from the different definitions of the growing seasons on the β trends in
 1789 global lands and arid and semi-arid areas. Three types of growing seasons were used: 1) using
 1790 only mean monthly air temperature ($> 0^\circ\text{C}$); 2) using both air temperature and “10% Pre”; 3)
 1791 using both air temperature and “20% Pre”. For each scenario, we first calculated the global
 1792 median β for every moving window during 1982–2015. Then the trends and their standard
 1793 errors (SEs) for the β time series were estimated. The error bars represent the SEs.
 1794



1795
 1796 **Fig. S17. a, Contributions to the global increasing trend of satellite GPP proxies by**
 1797 **different climate and environmental factors:** rising CO₂ (CO₂), mean annual air temperature
 1798 (MAT), vapour pressure deficit (VPD), atmospheric nitrogen deposition (Ndep), mean annual
 1799 precipitation (MAP), spring precipitation (Spring Pre) and non-spring precipitation (Non-
 1800 spring Pre). The relative contributions were calculated using the regression approach. The error
 1801 bars represent the standard deviations (SDs). Two points indicate that the relative contribution
 1802 is statistically significant ($p < 0.05$). **b, Temporal changes of β during 1982–2015 estimated**
 1803 **with 15-year moving windows after taking the seasonal distributions of precipitation into**
 1804 **consideration.** The annual precipitation was divided into four seasons: spring (March–May),
 1805 summer (June–August), autumn (September–November) and winter (December–February).
 1806 We included the seasonal precipitations into the regression model to calculate the global trends
 1807 of β . The grey area indicates one standard deviation (SD) either side of the mean ($n = 12850$).
 1808 The trends and statistical significances (p value) of the β time series were estimated using
 1809 Mann-Kendall test.
 1810

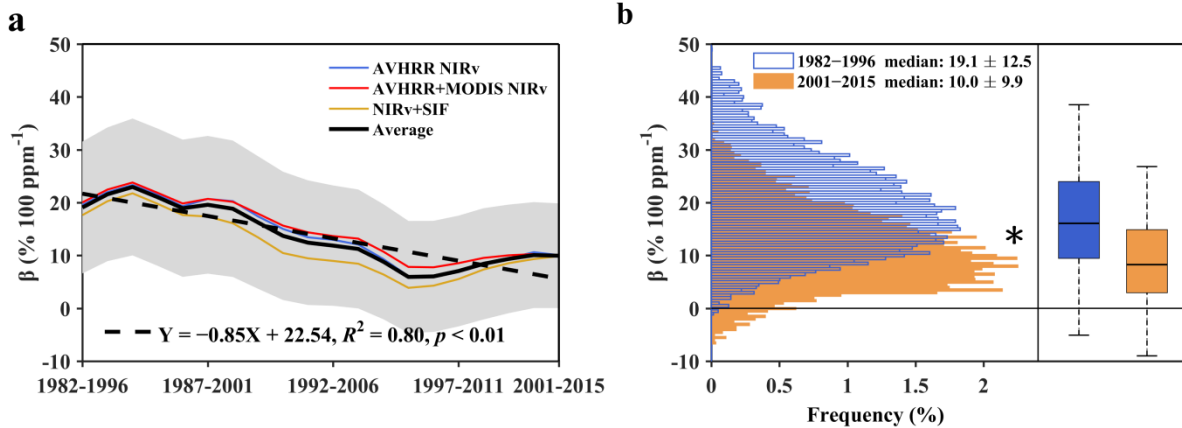


1811
 1812 **Fig. S18. Assessment of the relative errors for AVHRR and MODIS data (see**
 1813 **Supplementary Text S7). a-b,** Global distribution of relative errors for NOAA AVHRR/2 and
 1814 AVHRR/3 instruments, respectively. AVHRR/2 instruments flew from July 1981 to November
 1815 2000 onboard NOAA-7/9/11/14 satellites. AVHRR/3 instruments have flown since November
 1816 2000 to present onboard NOAA-16/17/18/19 satellites. MODIS instruments have been in
 1817 operation since December 1999 to present onboard Terra and Aqua. We estimated the relative
 1818 errors of these different sensors. Panel c shows an example of how these relative errors were
 1819 calculated. We used the weekly data to estimate the noise of monthly NIRv data. We firstly
 1820 derived the smoothed response of a time series for any single pixel, using a moving average
 1821 filter with a span of 4 weeks. The deviations between the raw and smoothed time series were
 1822 then calculated and interpreted as noise, since we assumed that the responses of vegetation at
 1823 ecosystem-level were slow within one week, therefore any sudden changes were likely caused
 1824 by noise rather than signals. We then normalized these deviations to relative errors by dividing
 1825 the peak values of the seasonal cycle. d, Probability density of the global relative errors of
 1826 different instruments (AVHRR/2, AVHRR/3 and MODIS).



1827
1828 **Fig. S19. Uncertainties of the global β time series.** **a**, Overall uncertainties of global β in
1829 each 15-year time window calculated from satellite GPP proxies. The uncertainties were
1830 estimated combining both the errors from original satellite data and uncertainties from the
1831 regression approach. The uncertainties from original satellite GPP proxies were estimated
1832 through uncertainty propagation. To estimate the uncertainty from regression approaches, we
1833 used 500 bootstrap analyses, for each combination of different sources of satellite data,
1834 different moving window lengths, different land cover change masks, different definitions of
1835 growing seasons and different combinations of climate and environmental factors. Detailed
1836 information for the estimation of uncertainty is presented in [Supplement Test S7](#). **b**, The global
1837 median β and their uncertainties for the first and the last 15-year windows (i.e., 1982–1996 and
1838 2001–2015) derived from satellite GPP proxies, revised EC-LUE GPP and TRENDY GPP,
1839 respectively. The errors bars represent the uncertainties.
1840

1841



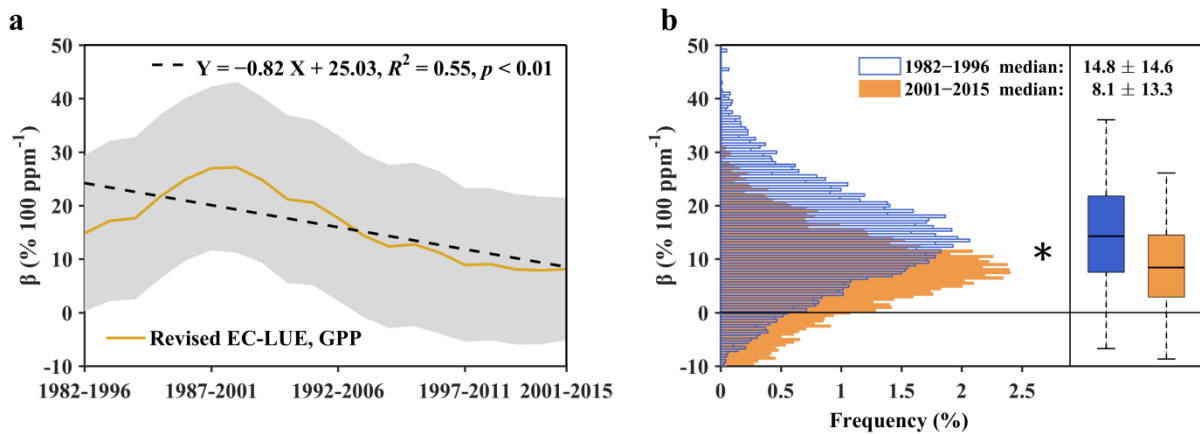
1842

1843 **Fig. S20. Declining global β detected using the optimal fingerprint attribution method.** **a,**
 1844 Temporal changes of β from the three satellite GPP proxies during 1982–2015 with 15-year
 1845 moving windows. The solid black line indicates the average of these three satellite GPP proxies.
 1846 The grey area indicates one standard deviation (SD) either side of the mean ($n = 12850$). The
 1847 dashed line indicates the linear regression. The trend and statistical significance (p value) of the
 1848 β time series were estimated using the Mann-Kendall test. **b,** The histogram distribution of β
 1849 across all pixels in two 15-years periods (1982–1996 and 2001–2015, left panel). β was the
 1850 average of these three satellite GPP proxies. In the right panel, boxes represent the interquartile
 1851 ranges of the β values (solid lines represent the median value), and whiskers extend to one
 1852 times the interquartile range. Median β of these two periods and their SDs were marked atop.
 1853 The asterisk indicates a significantly different β between these two periods using a two-sample
 1854 Kolmogorov-Smirnov test at $p < 0.01$.

1855

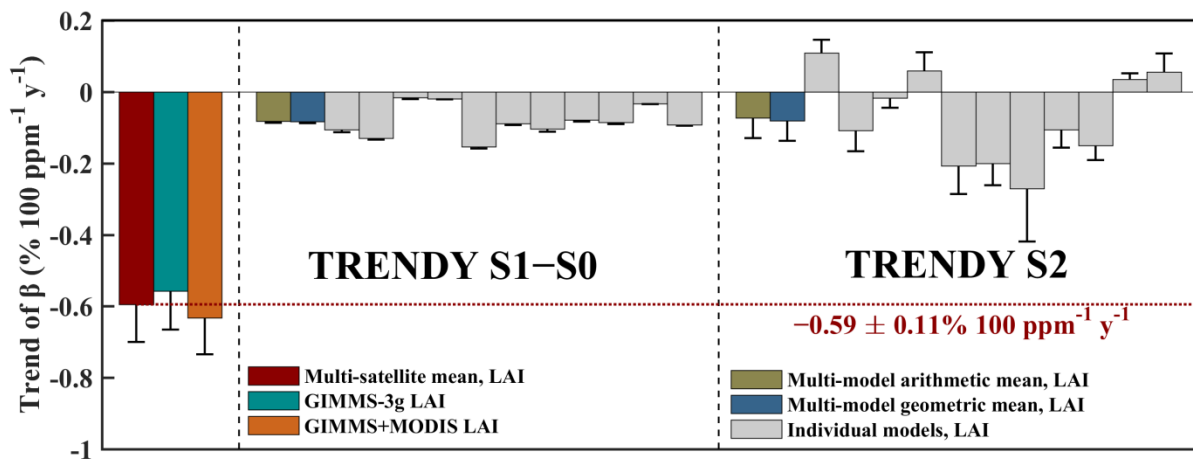
1856

1857

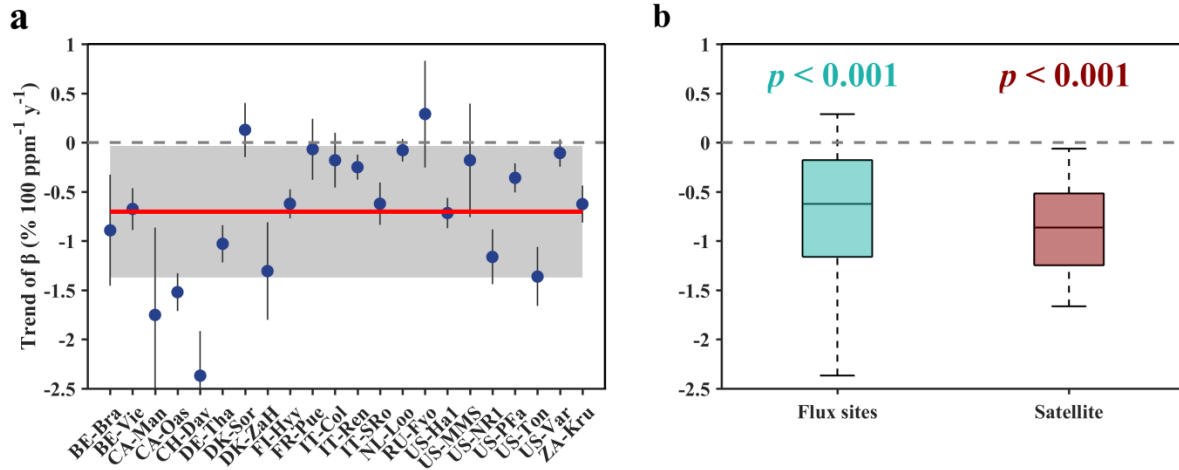


1858

1859 **Fig. S21. Temporal dynamics of β calculated from the revised EC-LUE GPP.** **a**, Temporal
 1860 changes of β during 1982–2015 estimated with 15-year moving windows from the revised EC-
 1861 LUE GPP. The dashed line indicates the linear regression. The grey area indicates one standard
 1862 deviation (SD) either side of the mean ($n = 12850$). The trends and statistical significances (p
 1863 value) of the β time series were estimated using Mann-Kendall test. **b**, The histogram
 1864 distribution of β across all pixels in two 15-years periods (1982–1996 and 2001–2015) for the
 1865 revised EC-LUE GPP. In the right panel, boxes represent the interquartile ranges of the β
 1866 values (solid lines represent the median value), and whiskers extend to one times the
 1867 interquartile range. Median β of these two periods and their SDs were marked atop. The
 1868 asterisks indicate a significantly different β between the two periods using a two-sample
 1869 Kolmogorov-Smirnov test at $p < 0.01$.
 1870

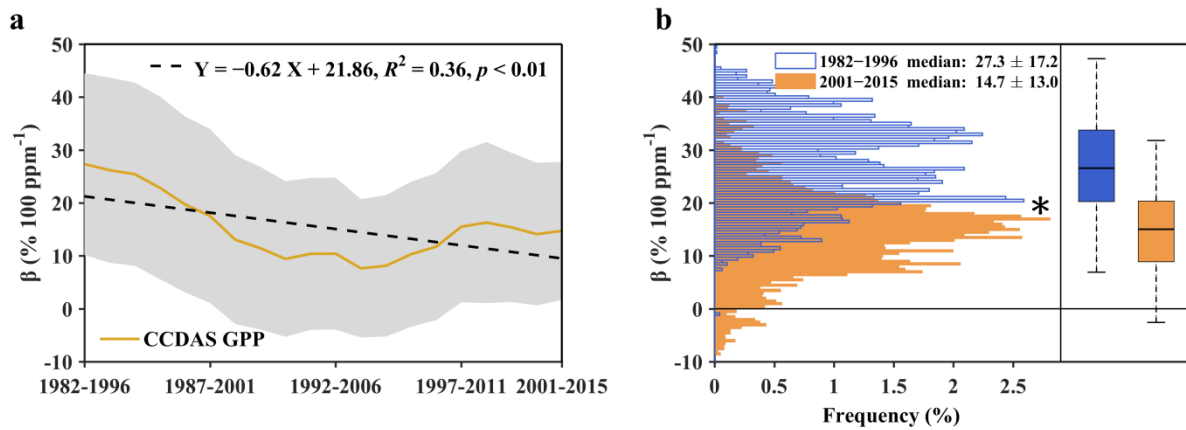


1871
 1872 **Fig. S22. Mean trends of β from satellite LAI and TRENDY LAI.** Similar to Fig. 2d, except
 1873 β was estimated from satellite-based LAI and TRENDY LAI. For satellite LAI, we used the
 1874 regression methods to calculate β . For TRENDY LAI, we used two methods to estimate β . The
 1875 first method followed the linear regression, which was used for LAI data from the TRENDY
 1876 ‘S2’ scenario. The second method referred to the differences of the LAI data between the
 1877 TRENDY ‘S1’ and ‘S0’ scenarios. For each data set, we first calculated the global median β
 1878 for every moving window during 1982–2015. Then the trends and their standard errors (SEs)
 1879 for the β time series were estimated. The error bars represent SEs. The horizontal dotted line is
 1880 used to aid comparisons with the results from the TRENDY models. Note that the DLEM
 1881 model is not included in this analysis, because LAI outputs for the DLEM model are not
 1882 available.
 1883



1884
 1885 **Fig. S23. Trends of β calculated from flux sites GPP estimates.** a, Trends of β calculated
 1886 from GPP estimations at 22 EC flux sites. We used flux data at sites which have at least 14
 1887 years of uninterrupted observations. The time series of β were estimated using the regression
 1888 approaches with 10-year moving window. The trends of the β time series were estimated using
 1889 the Mann-Kendall test. The blue dots represent the trend of β in each site, and the red line
 1890 represents the average trend of these 22 sites. The error bars and the grey area ($n = 22$)
 1891 represent the standard deviations (SDs). b, Boxplots for the β trends estimated from flux site
 1892 GPP estimates and satellite GPP proxies. We selected the β trend (calculated from satellite
 1893 GPP proxies) in the nearest pixel of each flux site, and then compared to the results calculated
 1894 from flux sites GPP. The statistical significance of the difference between these β trends and
 1895 zero were determined using one-way ANOVA test and marked atop of each box.
 1896

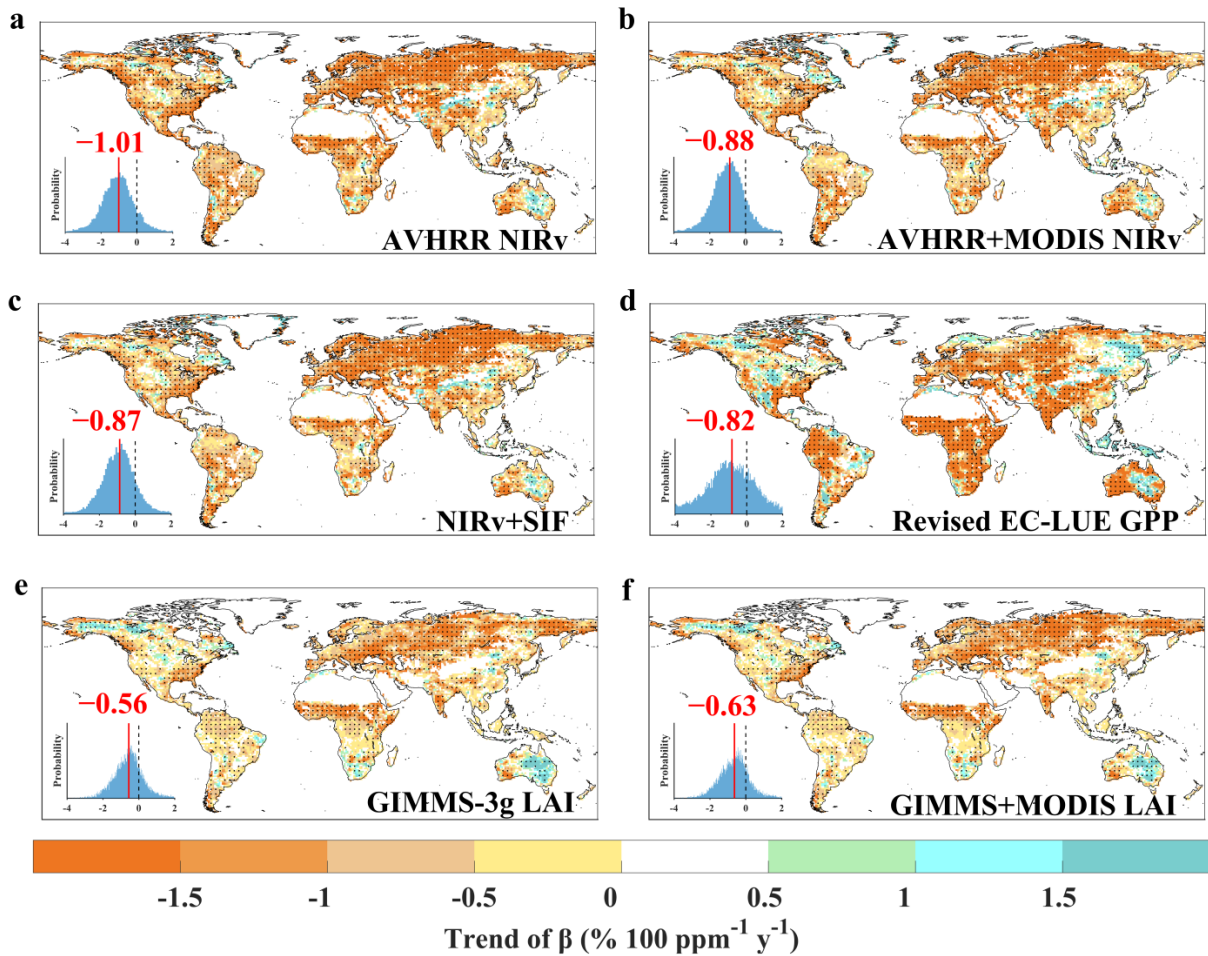
1897



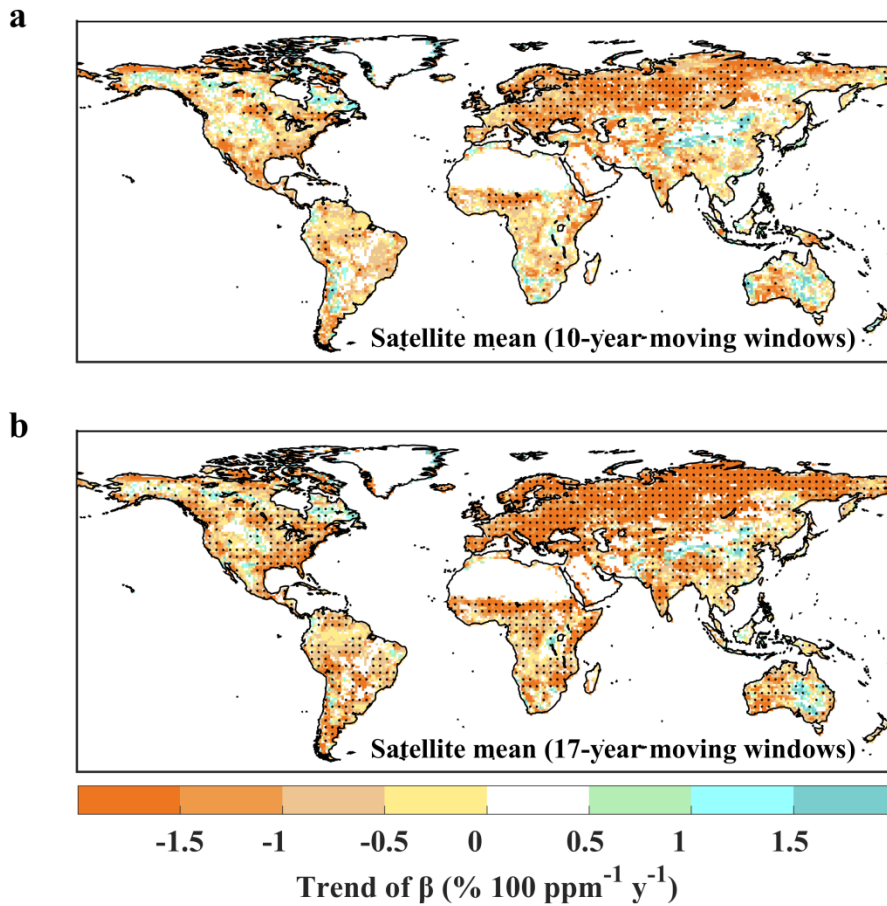
1898

1899 **Fig. S24. Temporal dynamics of β calculated from the CCDAS GPP.** a, Temporal changes
 1900 of β during 1982–2015 estimated with 15-year moving windows from the CCDAS GPP. The
 1901 dashed line indicates the linear regression. The grey area indicates one standard deviation (SD)
 1902 either side of the mean ($n = 12850$). The trends and statistical significances (p value) of the β
 1903 time series were estimated using Mann-Kendall test. b, The histogram distribution of β across
 1904 all pixels in two 15-years periods (1982–1996 and 2001–2015) for the CCDAS GPP. In the
 1905 right panel, boxes represent the interquartile ranges of the β values (solid lines represent the
 1906 median value), and whiskers extend to one times the interquartile range. Median β of these two
 1907 periods and their SDs were marked atop. The asterisks indicate a significantly different β
 1908 between the two periods using a two-sample Kolmogorov-Smirnov test at $p < 0.01$.

1909

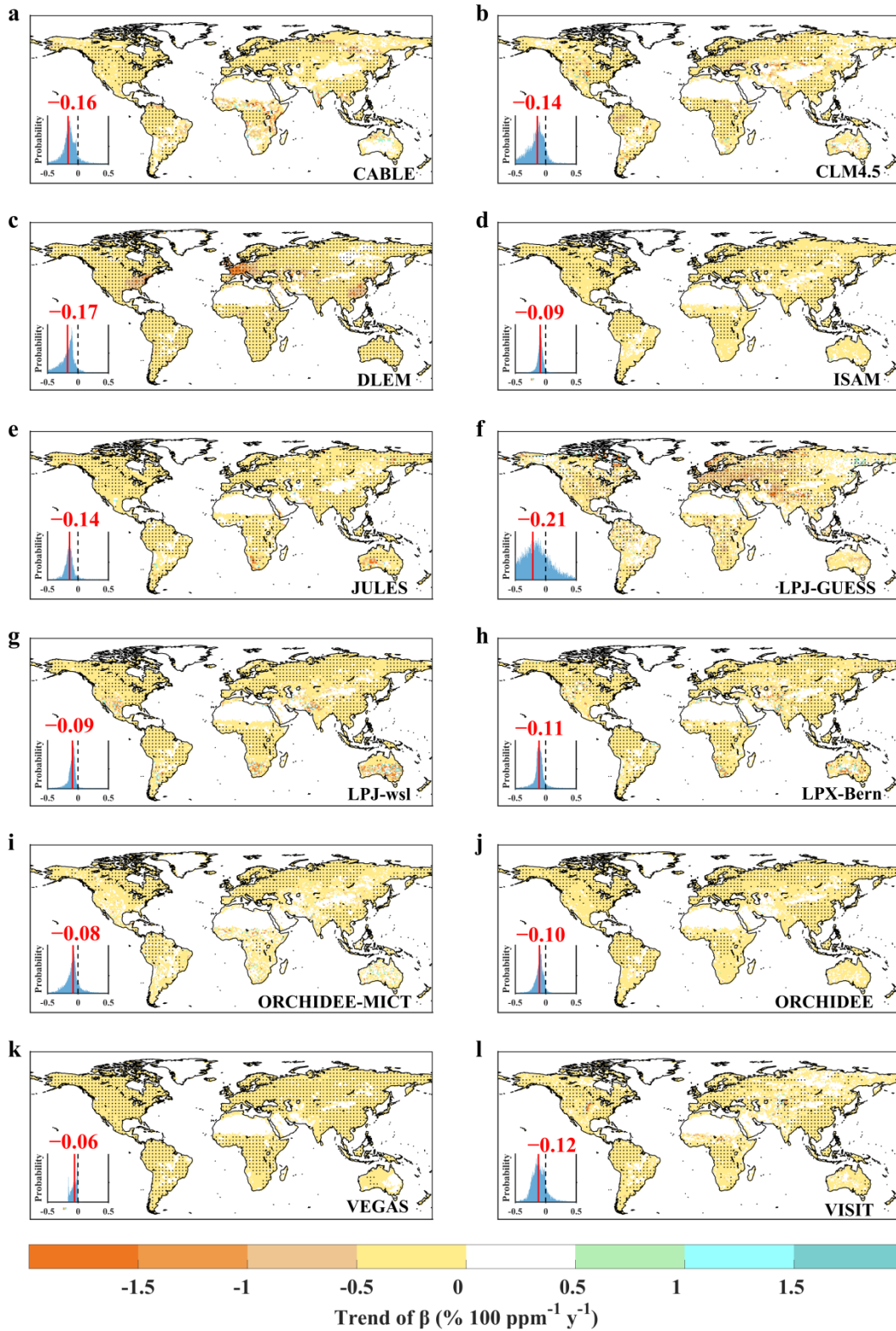


1910
 1911 **Fig. S25. Global trends of β derived from three satellite GPP proxies (a-c), LUE-based**
 1912 **GPP data set (d) and satellite LAI (e-f).** Spatial patterns of the trends in β derived from (a)
 1913 AVHRR NIR_v, (b) AVHRR+MODIS NIR_v, (c) NIR_v+SIF, (d) Revised EC-LUE GPP, (e)
 1914 GIMMS-3g LAI and (f) GIMMS+MODIS LAI using the linear regression approach with 15-
 1915 year moving windows. The trends of β time series were estimated using the Mann-Kendall test.
 1916 The kernel density distributions of the β trends across all pixels are shown in the lower-left
 1917 corner of each panel. The red vertical lines and numbers represent the medians. The regions
 1918 labelled with black dots indicate significant trends ($p < 0.05$).
 1919



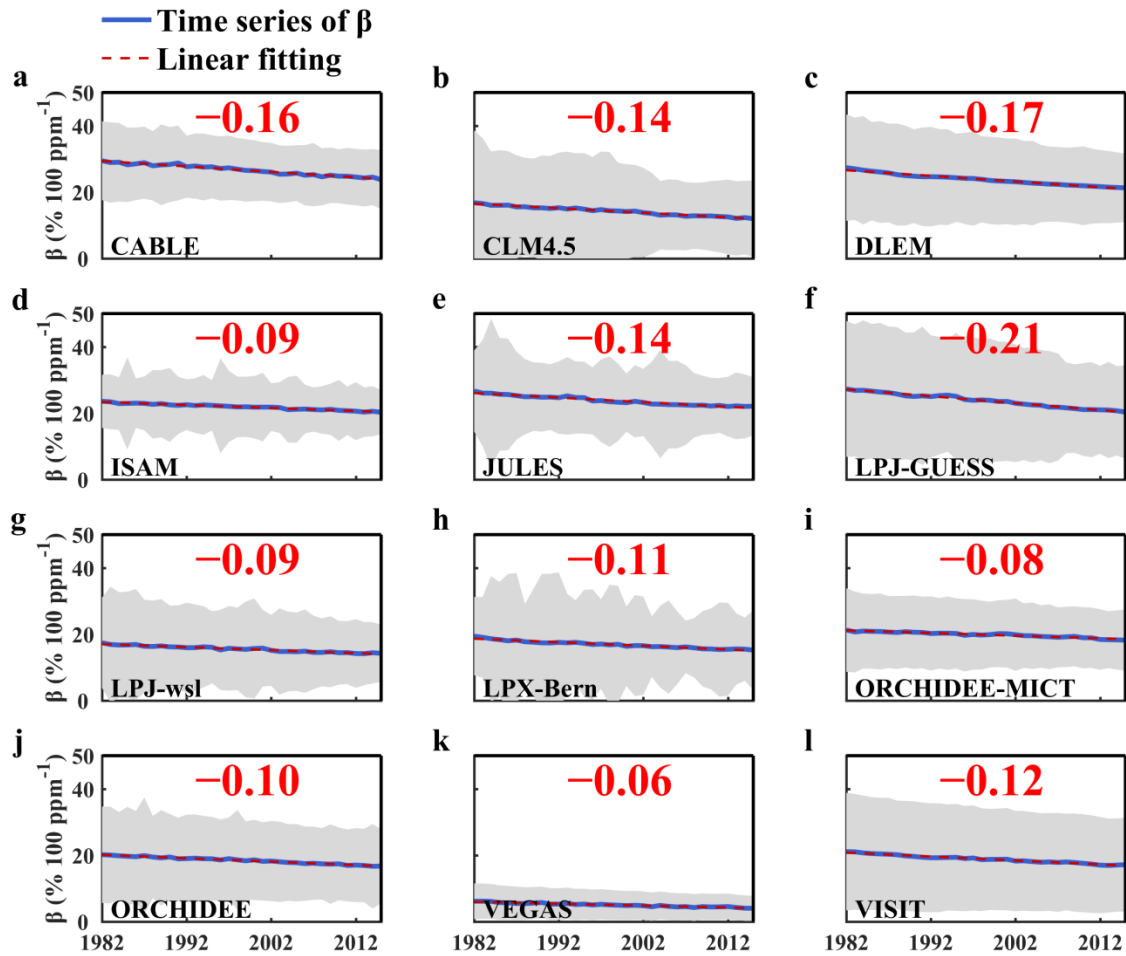
1920
1921
1922
1923
1924

Fig. S26. Global trends of β derived from satellite GPP proxies with 10-year (a) and 17-year (b) moving windows. The trends of β time series were estimated using the Mann-Kendall test. The regions labelled with black dots indicate significant trends ($p < 0.05$).

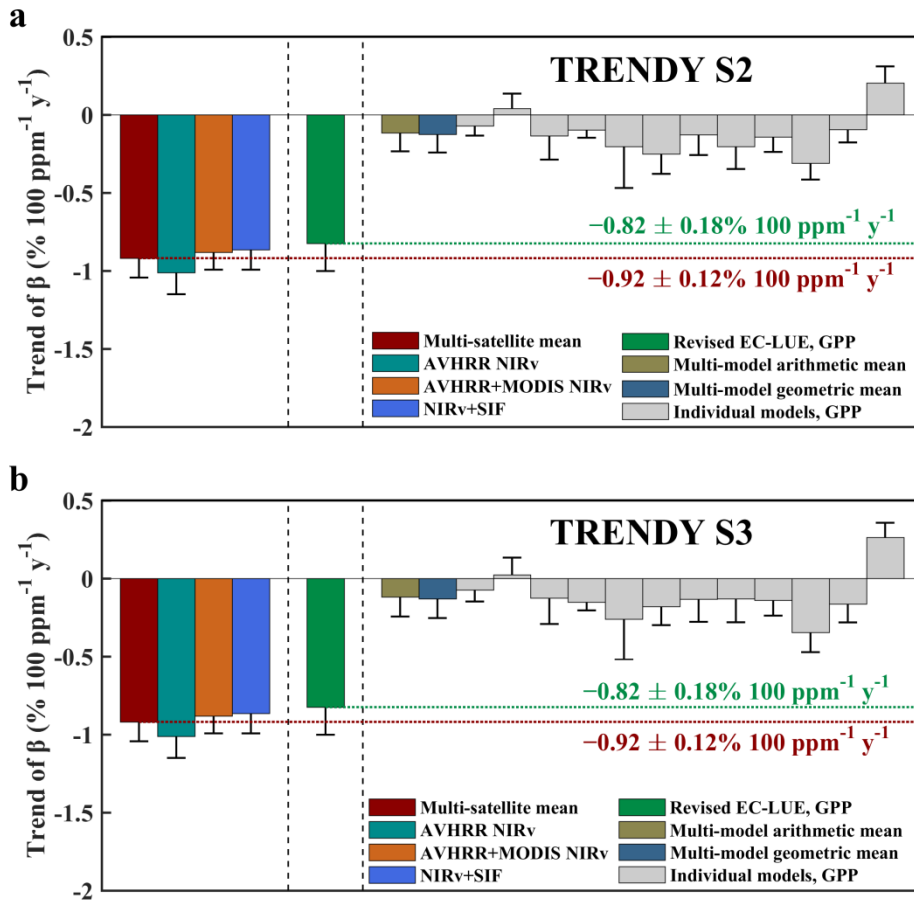


1925
1926
1927
1928
1929
1930
1931
1932

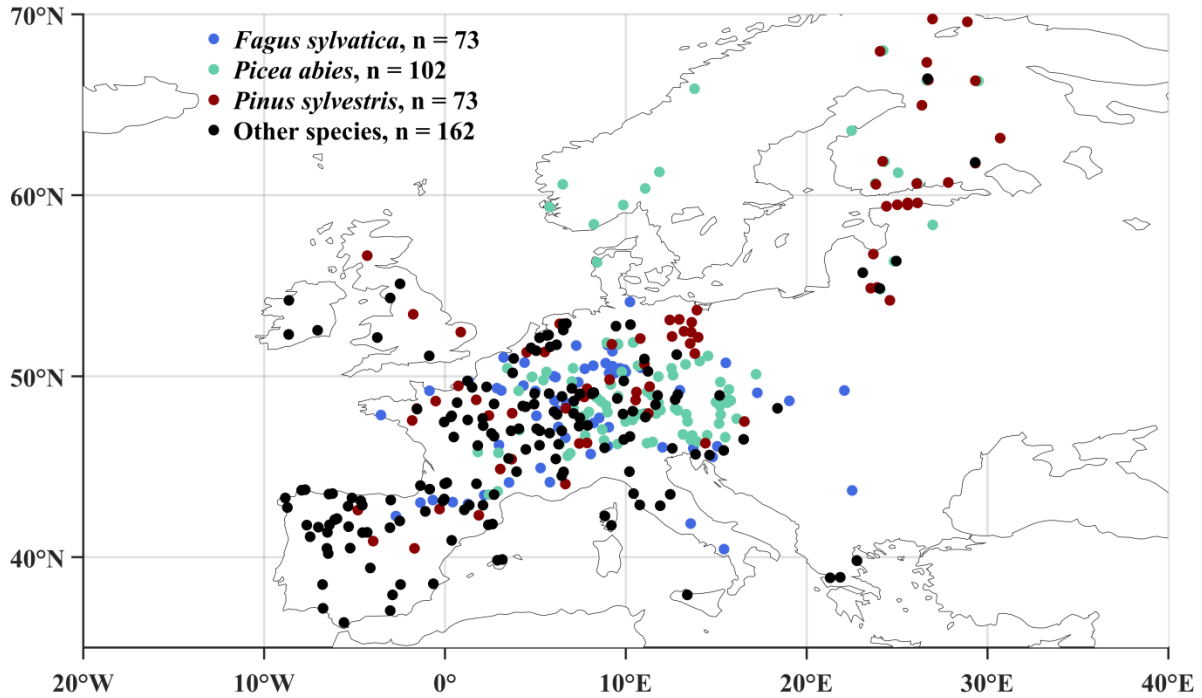
Fig. S27. Global trends of β derived from the TRENDY models. β was estimated following the Eq. (3), which was based on the differences of GPP data between TRENDY ‘S1’ and ‘S0’ scenarios. The trends of β time series were estimated using the Mann-Kendall test. The kernel density distributions of β trends across all pixels are shown in the lower-left corner of each panel. The red vertical lines and numbers represent the medians. The regions labelled with black dots indicate significant trends ($p < 0.05$).



1933
 1934
 1935 **Fig. S28. Global trends of β derived from each TRENDY model.** β was estimated following
 1936 the Eq. (3), which was based on the differences of GPP data between TRENDY ‘S1’ and ‘S0’
 1937 scenarios. The grey area indicates one standard deviation (SD) either side of the mean ($n =$
 1938 12850). The trends of the β time series were estimated using the Mann-Kendall test and
 1939 marked in red (atop of each panel).

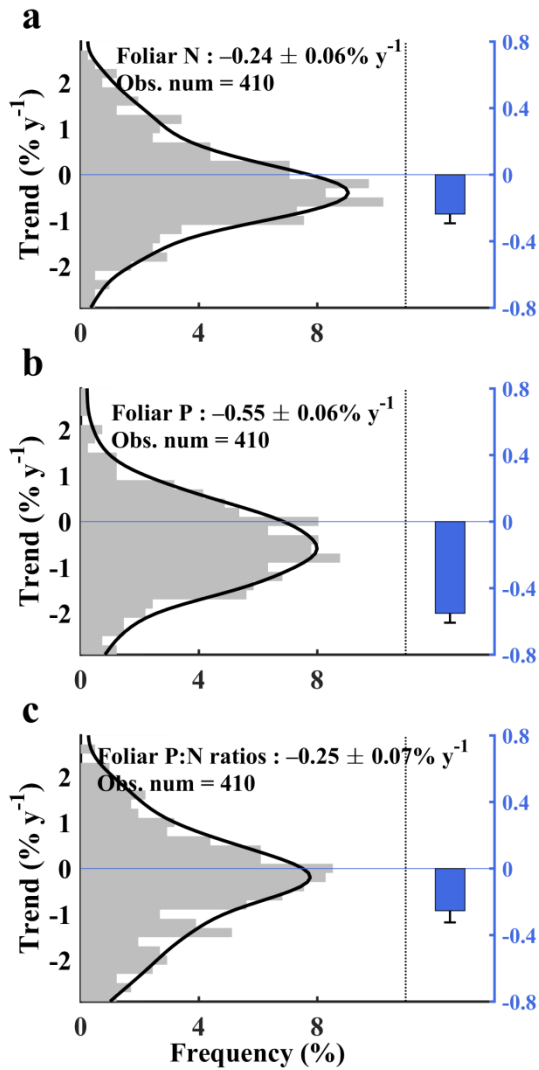


1940
 1941 **Fig. S29. Trends of β from TRENDY ‘S2’ and ‘S3’ GPP data using regression approaches.**
 1942 Similar to Fig. 2d, except β was estimated using regression methods and the TRENDY GPP
 1943 data were from the (a) ‘S2’ and (b) ‘S3’ scenarios. For each data set, we first calculated the
 1944 global median β for every moving window during 1982–2015. Then the trends and their
 1945 standard errors (SEs) for the β time series were estimated. The error bars represent SEs. The
 1946 horizontal dotted lines are used to aid comparisons with the results from the TRENDY models.
 1947



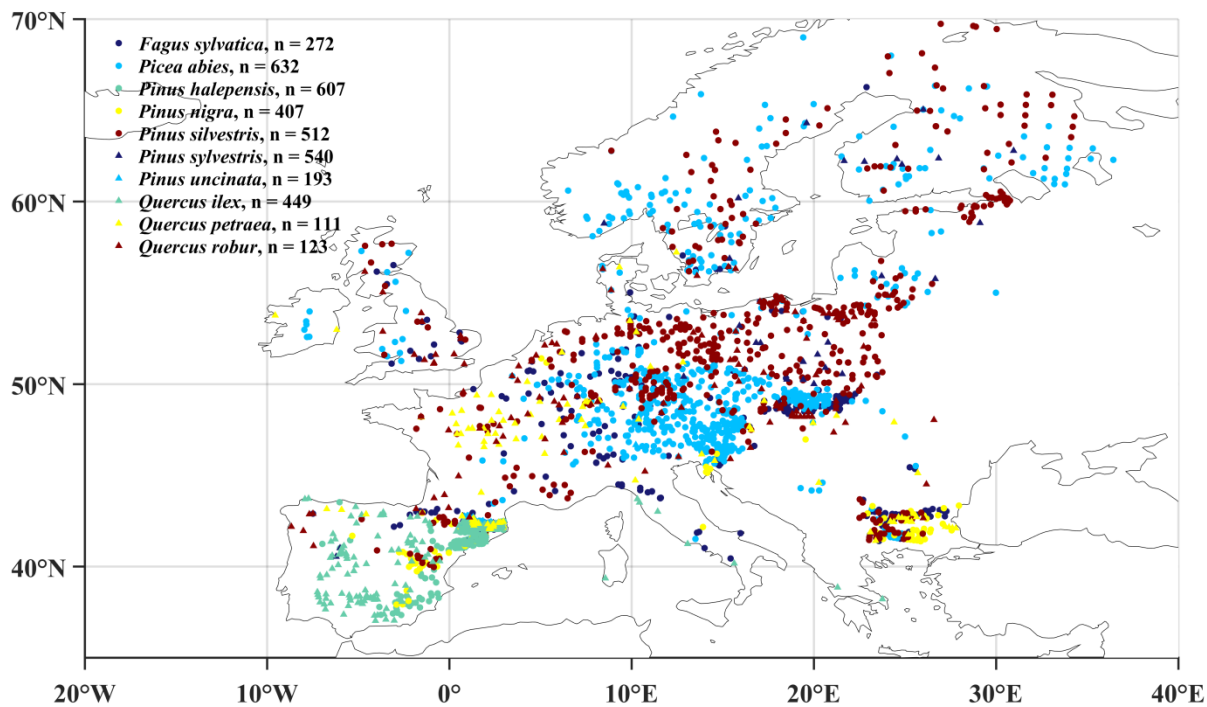
1948
1949
1950
1951
1952
1953
1954

Fig. S30. Observations of foliar N and P concentrations from ICP Forests (International Co-operative Programme on Assessment and Monitoring of Air Pollution Effects on Forests). We used 410 sites with several tree species, including the three main species (*Fagus sylvatica*, *Picea abies* and *Pinus sylvestris*). The observation period spanned from the 1990s to the 2010s.



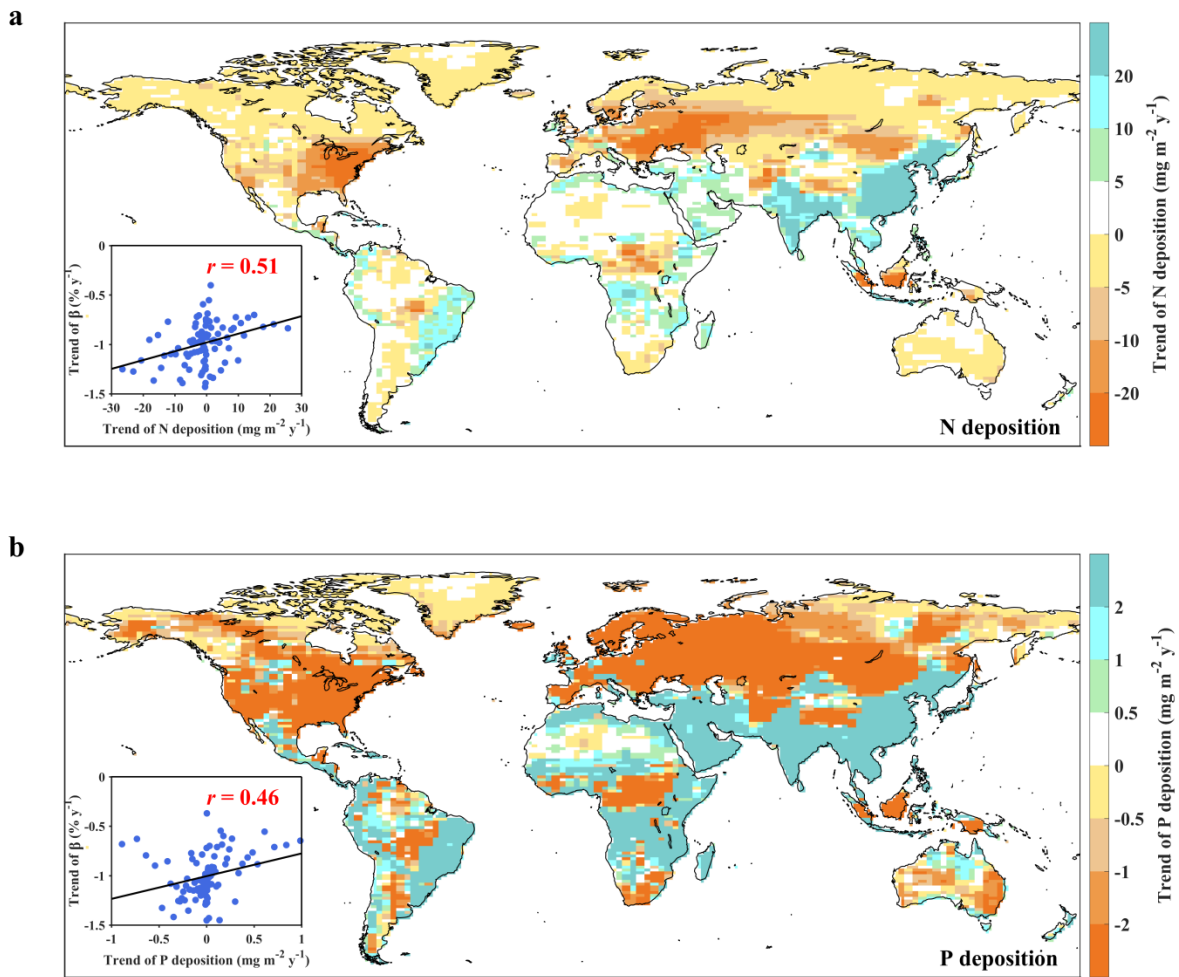
1955
1956
1957
1958
1959
1960

Fig. S31. Temporal trends of foliar traits derived from ICP Forests observations: a, foliar N concentration; b, foliar P concentration; c, foliar P:N ratio. The left panels represent the trends of foliar traits across 410 sites. The black lines represent the kernel density distribution of the values. The right panels show the site-averaged trend of each foliar trait and its standard error (SE) ($n = 410$). The scales of the y-axes of the right panels are enlarged.



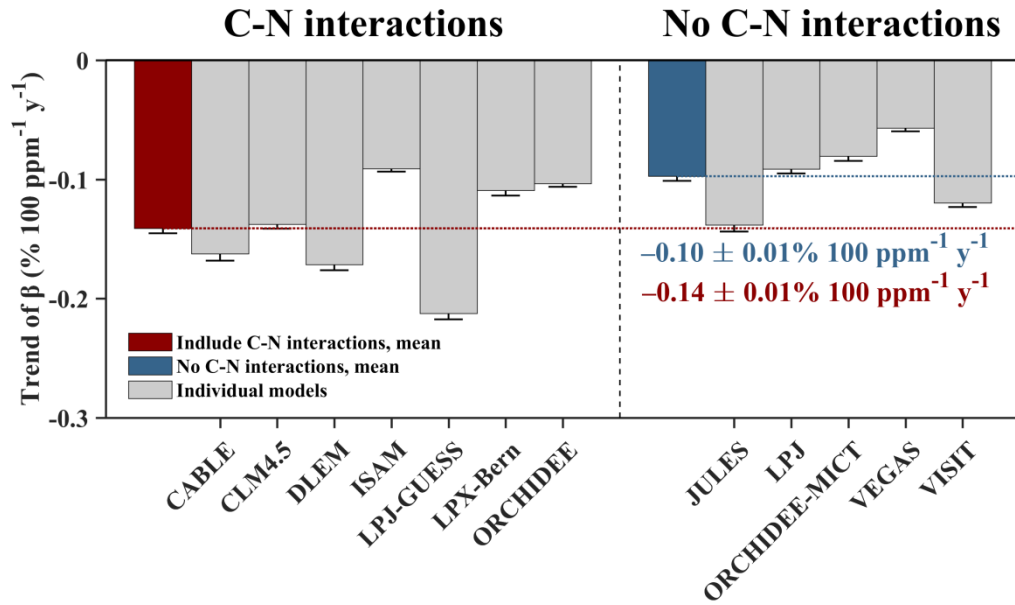
1961
1962
1963
1964

Fig. S32. Spatial observations of foliar N and P concentrations in Europe. Ten tree species with more than 100 observations were chosen. Overall 3846 site-specific samples were used.

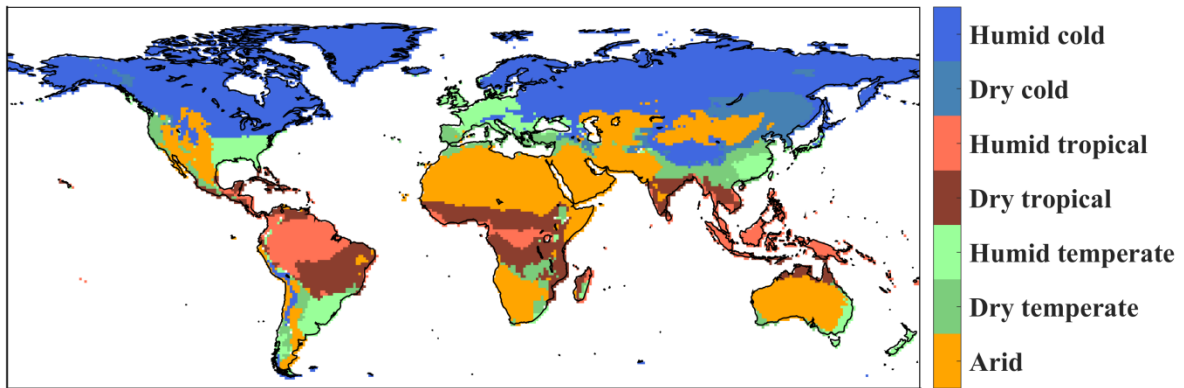


1965
1966
1967
1968
1969
1970

Fig. S33. Spatial patterns of trends in atmospheric nutrient deposition during 1980–2013: a, nitrogen; b, phosphorus. The trends of the N and P depositions were estimated using the Mann-Kendall test. The relationships between the trends of N and P deposition and the trends of β are shown in the lower-left corner of each panel.

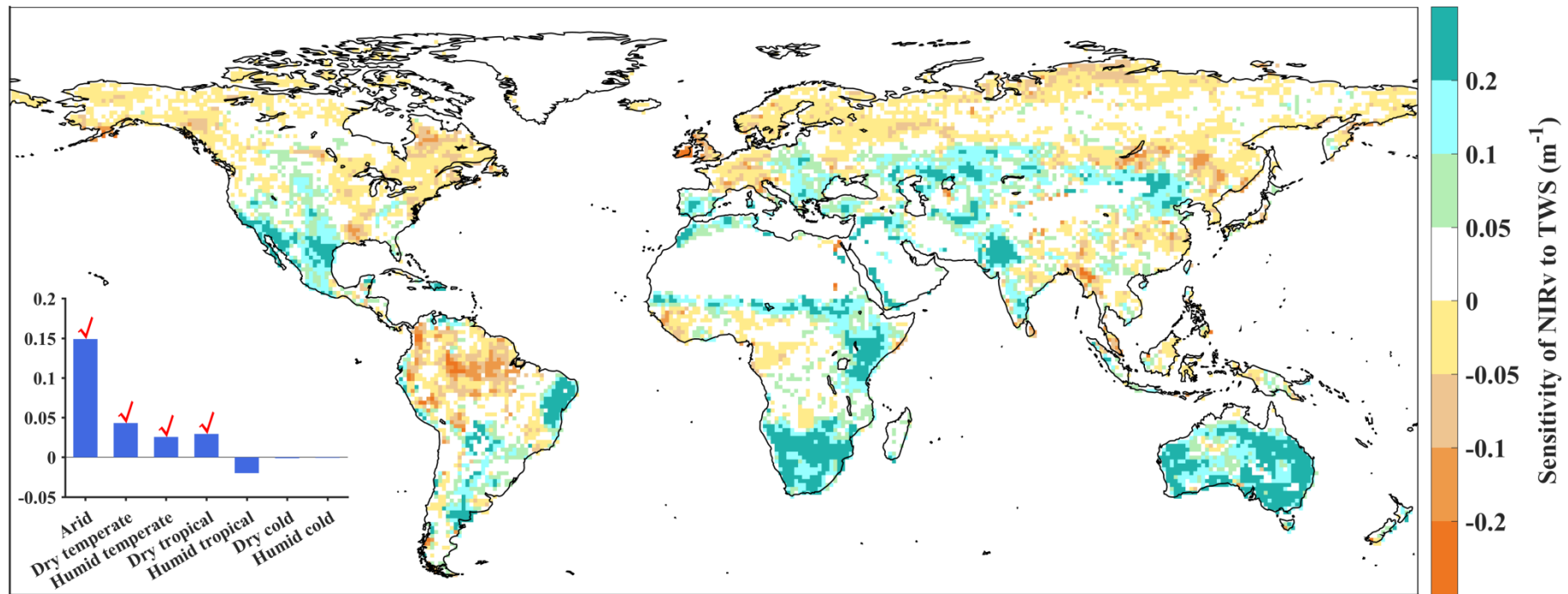


1971
 1972 **Fig. S34. Trends of β from the TRENDY models with the carbon-nitrogen (C-N)**
 1973 **interactions or without the C-N interactions.** β was estimated following Eq. (3), which was
 1974 based on the differences of GPP data between TRENDY ‘S1’ and ‘S0’ scenarios. The trends of
 1975 β time series were estimated using the Mann-Kendall test. For each data set, we first calculated
 1976 the global median β for every year during 1982–2015. Then the trends and their standard errors
 1977 (SEs) for the β time series were estimated. The error bars represent SEs. The horizontal dotted
 1978 lines are used to aid comparisons.
 1979



1980
1981
1982
1983
1984
1985
1986
1987

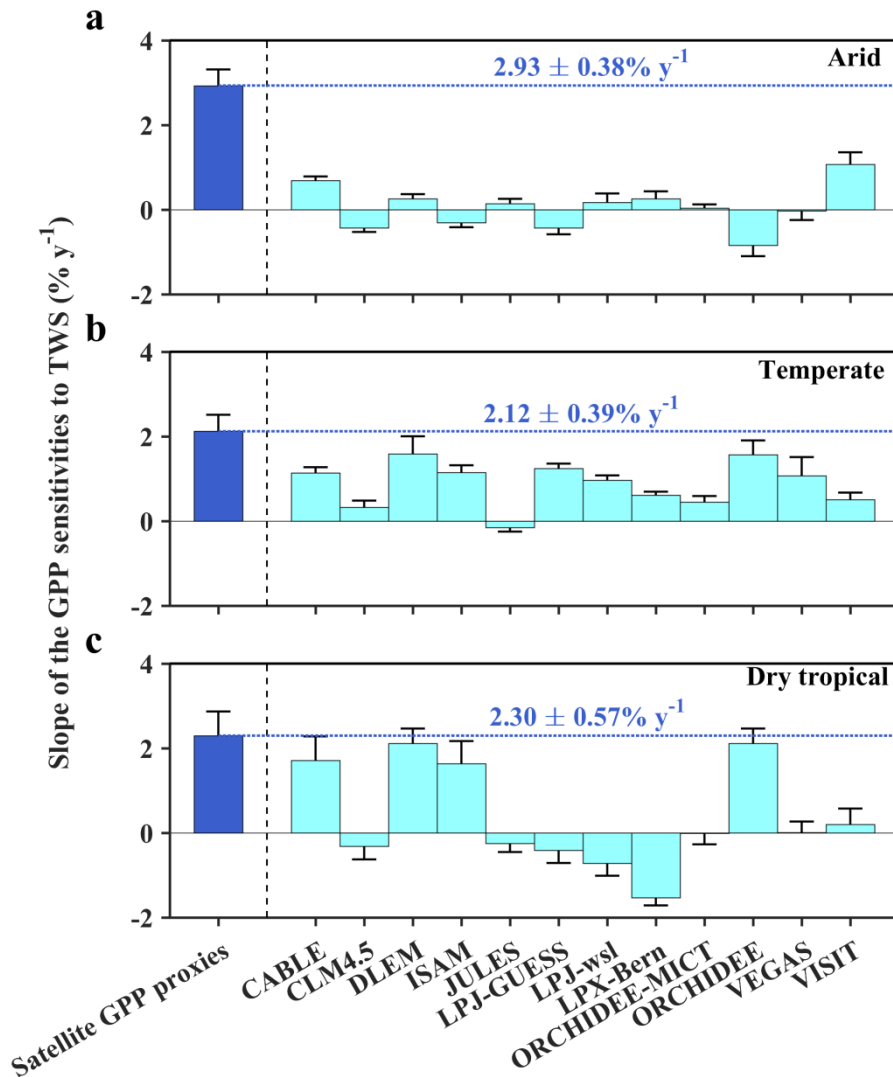
Fig. S35. Re-classified map of the climate zones. Original climate zones were derived from the Köppen-Geiger classification. We re-classified the climate zones by separating the cold, temperate and tropical areas into dry and humid types. Equatorial savannahs with dry summers or winters are classified into dry tropical, while other tropical zones are labelled as humid tropical. Snowy climates with dry summers or winters are classified into dry cold, while other cold zones are labelled as humid cold. Warm temperate climates with dry summers or winters are classified into dry temperate, while other cold zones are labelled as humid temperate.



1988

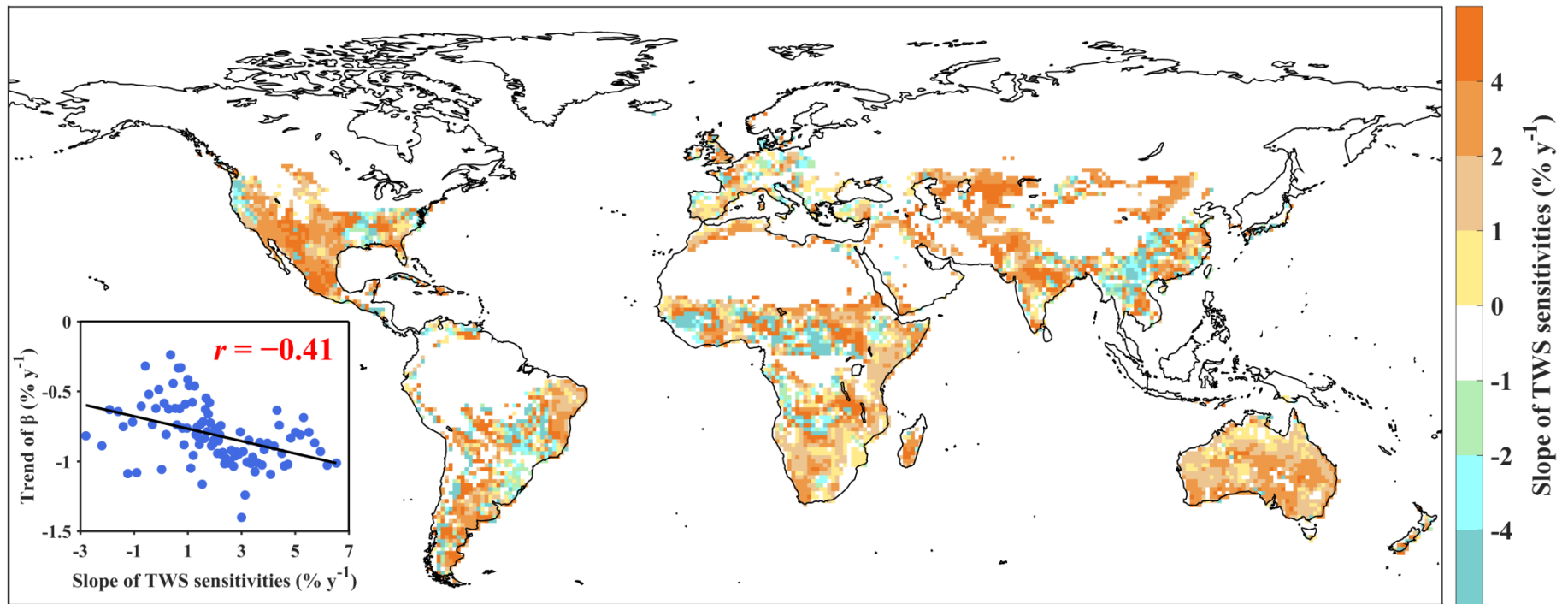
1989 **Fig. S36. Global sensitivity of GPP proxies to TWS.** The sensitivity of NIR_v to TWS represents the interannual change of NIR_v in response to
 1990 one unit interannual change in TWS. We calculated the TWS sensitivities by fitting least-squares regressions, in which satellite NIR_v annual
 1991 time series were the response variables and TWS annual time series were the predictor variables. The green areas indicate that GPP is more
 1992 sensitive to water availability and vice versa. Areas with high TWS sensitivities are in Southwest North America, central Asia, southern Africa,
 1993 the Mediterranean Basin and Australia (often covered with grass and savannah), where GPP is more sensitive to the changes of water supply.
 1994 Average TWS sensitivities across different climate zones are shown in the lower-left corner of this figure. The arid, temperate (both dry and
 1995 humid temperate) and dry tropical zones were then selected as the research areas (labelled with red checkmarks), because GPP in these zones is
 1996 more sensitive to TWS.

1997



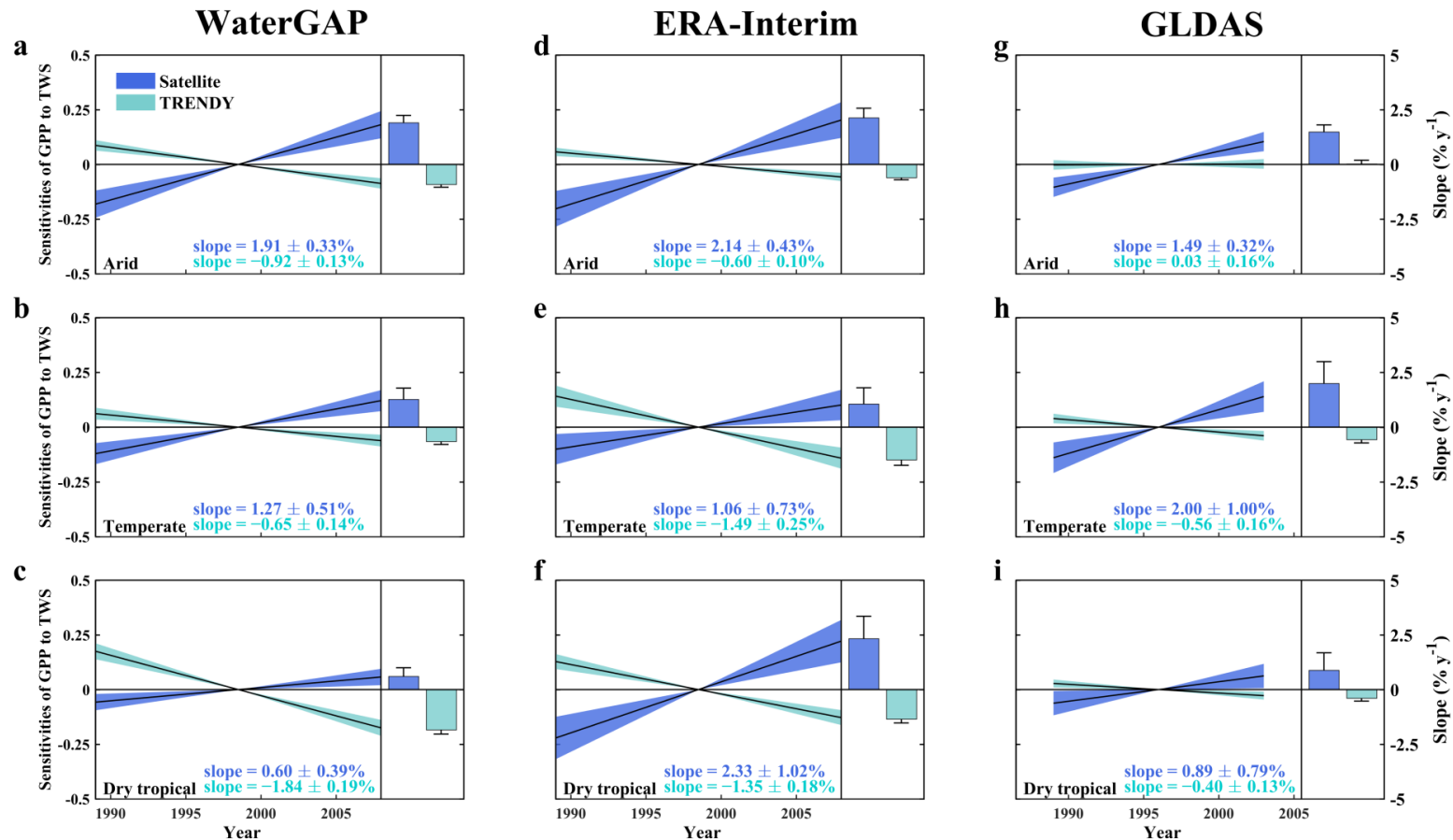
1998
1999
2000
2001
2002
2003
2004
2005
2006
2007

Fig. S37. Comparisons of the GPP sensitivities to TWS between satellite GPP proxies and individual TRENDY models. The sensitivities were calculated using the TWS data from the MERRA-2 product and then standardized. Panels (a-c) represent the results for three climate zones (arid, temperate and dry tropical). For each data set, we first calculated the global median sensitivity for every moving window during 1982–2015. Then the trends and their standard errors (SEs) for the sensitivity time series were estimated. The bars and error bars indicate the slopes and their SEs, respectively. The horizontal dotted lines are used to aid comparisons with the results from the TRENDY models.



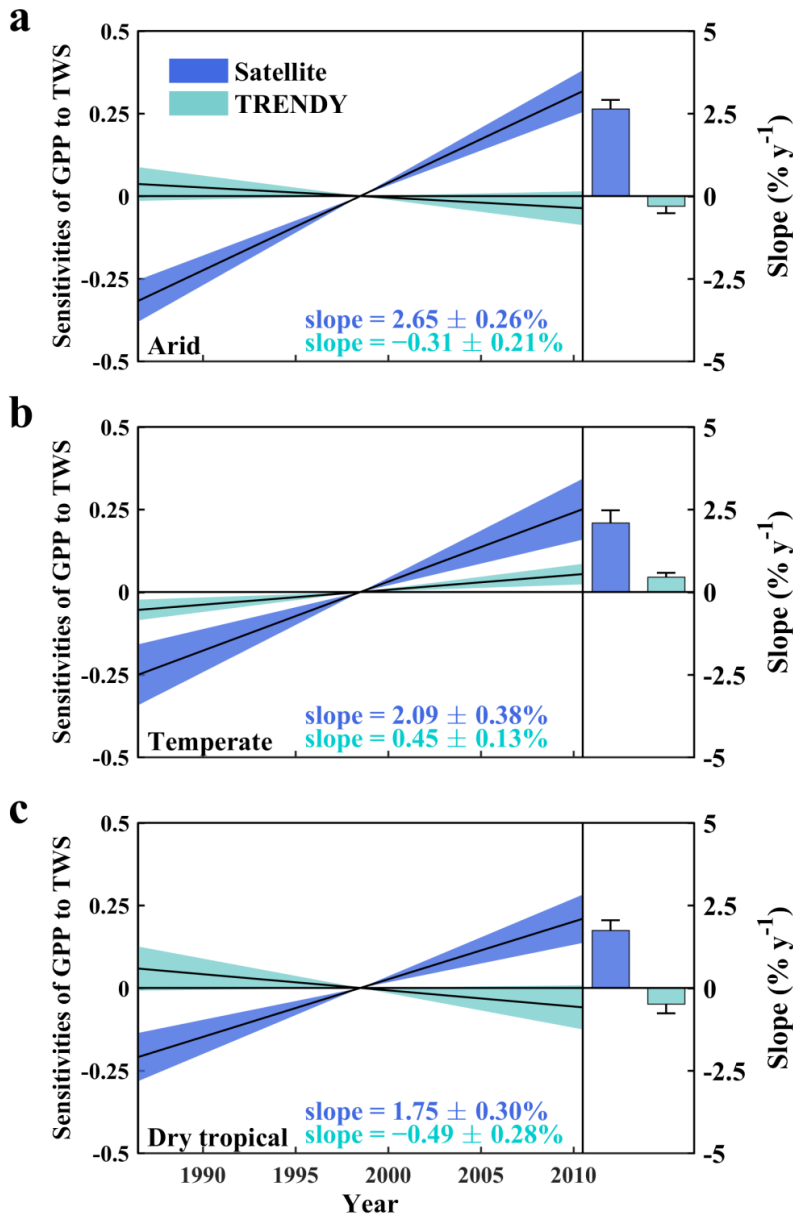
2008
2009
2010
2011
2012
2013

Fig. S38. Spatial patterns of the slopes of TWS-sensitivities and their relationship with the trends of β . The TWS-sensitivities are calculated using the TWS data from the MERRA-2 products. The trends of the TWS-sensitivities were estimated using the Mann-Kendall test. The relationships between the slopes of TWS-sensitivities and the trends of β in arid, temperate and dry tropical climate zones are shown in the lower-left corner of the panel.



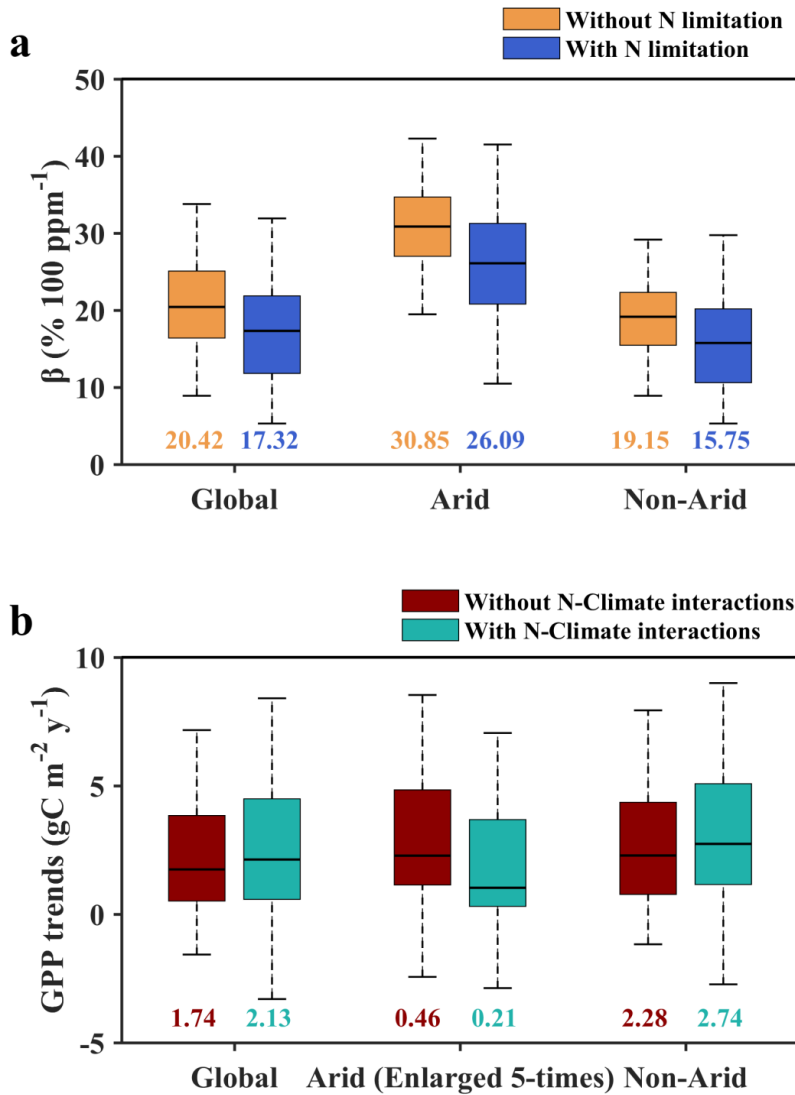
2014
2015
2016
2017
2018
2019
2020

Fig. S39. Sensitivities of GPP to TWS using three other TWS data sets: a-c, WaterGAP; d-f, ERA-Interim and g-i, GLDAS. The sensitivities were calculated using 15-year moving windows and then standardized. Different columns represent the results for three climate zones (arid, temperate and dry tropical). The solid lines in the left panels represent the linear regressions of the sensitivity time series based on satellite GPP proxies or TRENDY GPP. We first calculated the global median sensitivity for every moving window during 1982–2015. Then the trends and their standard errors (SEs) for the sensitivities time series were estimated. The shaded areas represent the SEs. The bars and error bars in the right panels indicate the slopes and their SEs, respectively. Note that the GLDAS TWS data only spanned from 1982 to 2010.

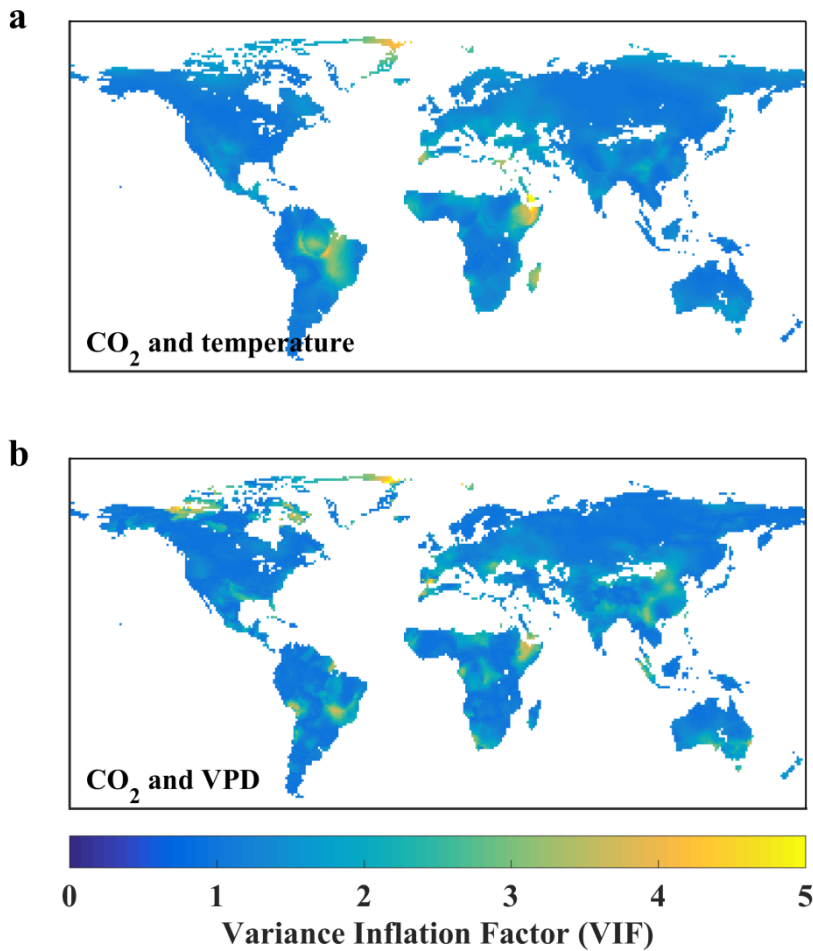


2021
2022
2023
2024
2025
2026
2027
2028
2029
2030
2031

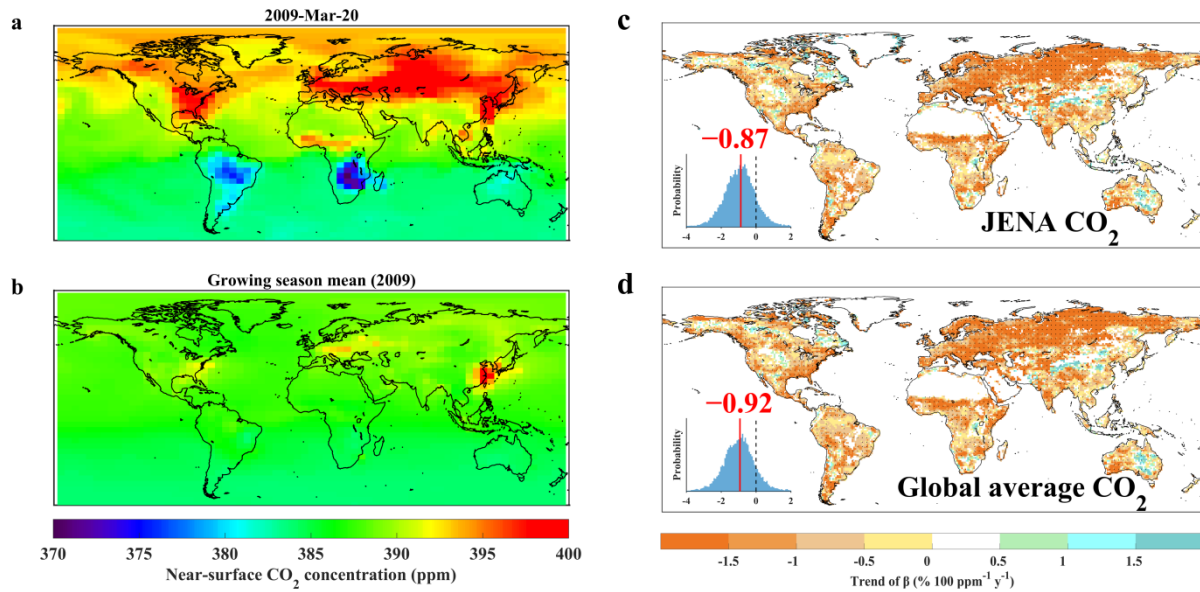
Fig. S40. Sensitivities of GPP to TWS using shorter (10-year) moving windows. The sensitivities are calculated using the TWS data from the MERRA-2 products and then standardized. Different columns represent the results for three climate zones (arid, temperate and dry tropical). The solid lines in the left panels represent the linear regressions of the sensitivity time series based on satellite GPP proxies or TRENDY GPP. We first calculated the global median sensitivity for every moving window during 1982–2015. Then the trends and their standard errors (SEs) for the sensitivities time series were estimated. The shaded areas represent the SEs. The bars and error bars in the right panels indicate the slopes and their SEs, respectively.



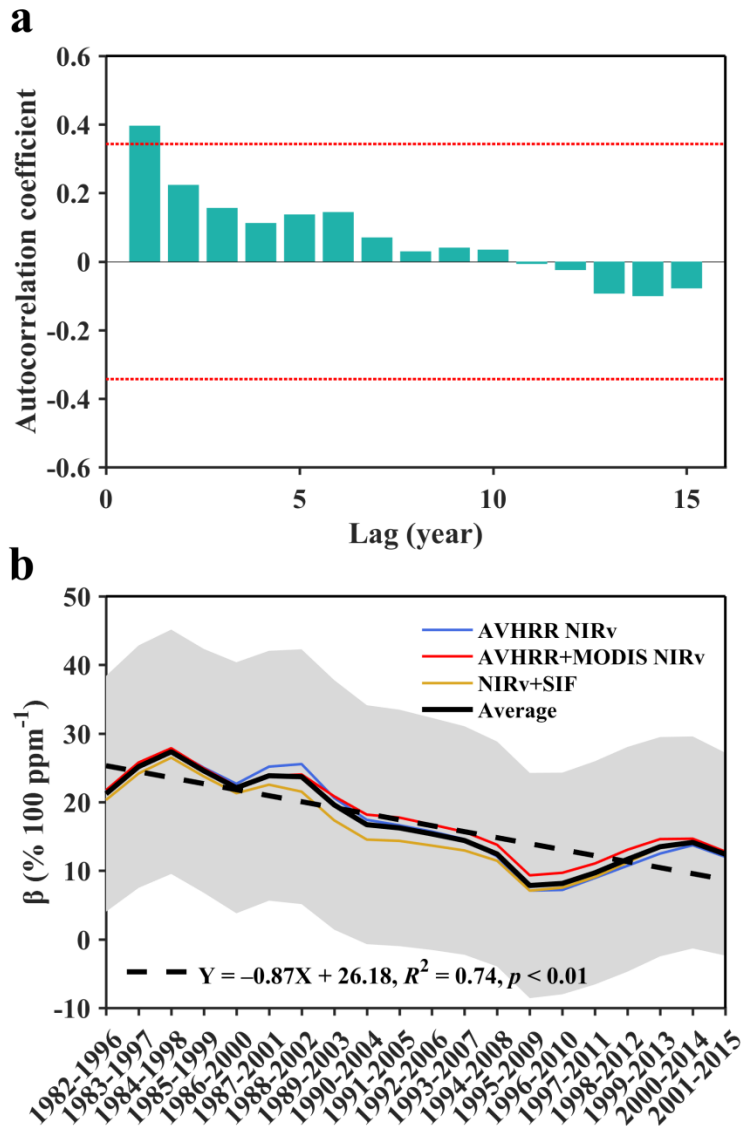
2032
 2033 **Fig. S41. The impacts of nitrogen (N) limitation on CO₂ fertilization effects (a), and the**
 2034 **impacts of N-climate interactions on GPP trends (b).** We firstly used the Boreal Ecosystem
 2035 Productivity Simulator (BEPS) model to simulate the global yearly GPP based on different
 2036 scenarios during 1982–2015. Please find the detailed information in [Supplementary Text S16](#).
 2037 We then calculated the global β values and the global GPP trends according to different
 2038 scenarios. Boxes represent the interquartile ranges of the values (solid lines represent the
 2039 median value), and whiskers extend to one times the interquartile range. Median value of each
 2040 box was marked below. In panel **b**, for clear visualization, the GPP trends in arid areas were
 2041 enlarged 5-times.
 2042
 2043
 2044



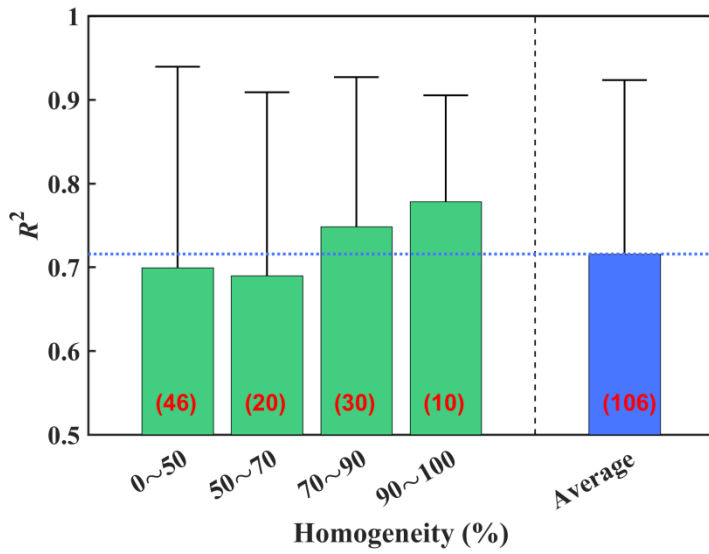
2045
2046 **Fig. S42. Global variance inflation factor (VIF) between CO₂ with Tmax and VPD,**
2047 **respectively.** VIF was used to measure how much the variance of a regression coefficient is
2048 inflated due to multicollinearity in the model. VIF values that are lower than 5 generally
2049 indicate that no multicollinearity exists in the model; VIF values between 5 and 10 generally
2050 indicate a weak multicollinearity; and VIF values that are larger than 10 generally indicate a
2051 medium or severe multicollinearity.
2052



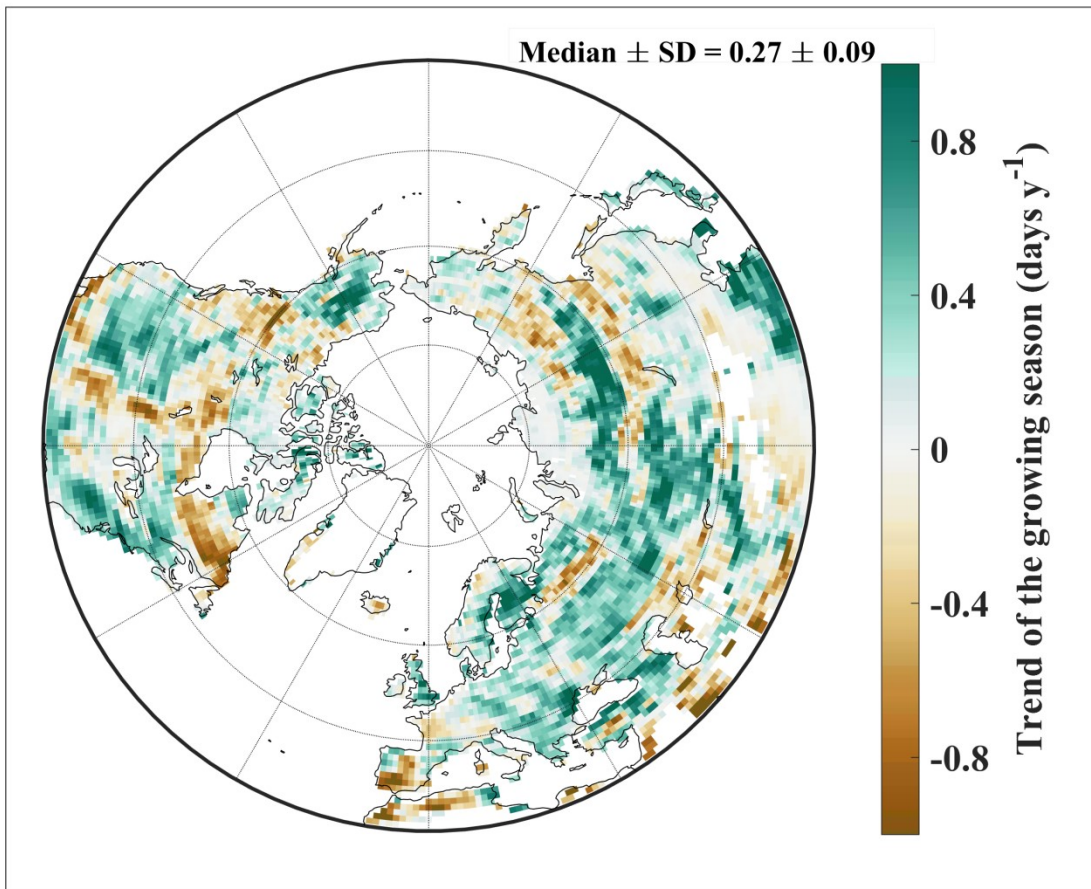
2053
 2054 **Fig. S43. Robustness of our analysis using the global average CO₂.** **a**, global gridded near-
 2055 surface CO₂ concentration at 2009-Mar-20; **b**, global gridded growing season mean near-
 2056 surface CO₂ concentrations of 2009. Global near-surface CO₂ concentrations during 1982–
 2057 2015 were obtained from the atmospheric CO₂ field simulations (sEXTocNEET_v4.3) based
 2058 on Jena CarboScope inversion model (<http://www.bgc-jena.mpg.de/CarboScope/s/main.html>).
 2059 There are clear spatial differences of the near-surface CO₂ concentrations in a certain day, e.g.,
 2060 CO₂ concentrations are higher in the Northern Hemisphere than those in the Southern
 2061 Hemisphere at 2009-Mar-20. However, this spatial difference would rarely be seen when we
 2062 integrated them into the growing season mean values, which actually were used to calculate the
 2063 global β. We further calculated the global β trends based on the gridded growing season mean
 2064 values of near-surface CO₂ concentration from JENA CarboScope model (panel **c**), and then
 2065 compared them with the results based on global average CO₂ from NOAA (panel **d**). The
 2066 almost no differences between these two results indicated that our findings based on the global
 2067 average CO₂ concentrations are robust.
 2068



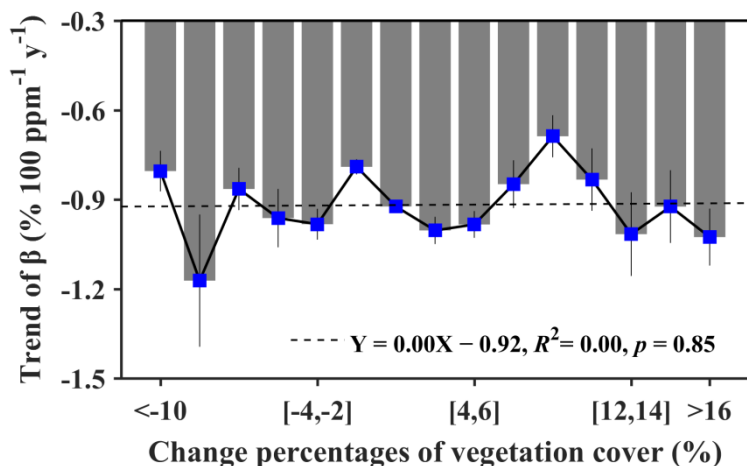
2069
2070
2071 **Fig. S44. Autocorrelation in yearly satellite GPP proxies and their impacts on the trends**
2072 **of β .** **a**, Autocorrelation coefficients for yearly satellite GPP proxies during 1982–2015. The
2073 values are the average of the three satellite data sets (AVHRR NIR_v, AVHRR+MODIS NIR_v
2074 and NIR_v+SIF). Dashed lines indicate 95% confidence bounds. **b**, Temporal dynamics of β for
2075 three satellite GPP proxies with 15-year moving windows during 1982–2015 using a linear
2076 mixed model that specifically accounts for the temporal autocorrelation with a first-order
2077 autocorrelation function. The solid black line indicates the average of these three observations.
2078 The grey area indicates one standard deviation (SD) either side of the mean ($n = 12850$). The
2079 dashed black line indicates the linear regression. The trend and statistical significance (p value)
2080 of the β time series were estimated using a nonparametric trend test (Mann-Kendall test).



2081
 2082 **Fig. S45. R^2 values between monthly MODIS NIRv with GPP according to different**
 2083 **homogeneity levels of the flux sites.** The X-axis represents the homogeneity percentage of the
 2084 flux site, i.e., how much the land cover type of the satellite pixels was the same with that of the
 2085 flux site. The number of the flux sites in each category was marked in red text. The error bars
 2086 represent standard deviations (SDs).
 2087



2088
2089 **Fig. S46. The linear trends of growing season length (GSL) during 1982–2015 across the**
2090 **mid- to high-latitudes (>30°N).** Following a widely used method (see the details in
2091 [Supplementary Text S1](#)), annual GSL were firstly estimated during 1982–2015 and then the
2092 linear trends were estimated using the Mann-Kendall test. The median value of all the pixels
2093 and its standard deviation (SD) were marked atop of this figure ($n = 7934$).
2094



2095

2096 **Fig. S47. Relationship between vegetation cover changes and β trends during 1982–2015.**
 2097 We firstly calculated the change percentages of the vegetation cover of each pixel based on a
 2098 long-term global vegetation cover dataset (76). Values in the x-axis larger than zero indicate
 2099 that the vegetation cover is increasing during 1982–2015 and vice versa. Then we estimated
 2100 the relationship between vegetation cover changes and global β trends. Data are classified into
 2101 15 bins for clear visualization based on the x-axis. The blue squares represent the means for
 2102 each bin, and the error bars represent the standard deviations (SDs). The dotted black lines
 2103 represent the linear regression.

2104

2105 **Table S1. Descriptions and access information of the data sets.**

Data set	Short description	Reference	Data access
AVHRR NDVI and NIR _T	Normalized vegetation index (NDVI) and Total scene near-infrared band reflectance from AVHRR	(60)	https://ltdr.modaps.eosdis.nasa.gov/cgi-bin/ltdr/ltdrPage.cgi?fileName=products
GIMMS 3g.v1 NDVI and LAI	NDVI and leaf area index (LAI) from GIMMS 3g products	(59, 96)	https://ecocast.arc.nasa.gov/data/pub/gimms/3g.v1/ http://sites.bu.edu/cliveg/datacodes/
MODIS NDVI, NIR _T and LAI	NDVI and NIR _T from MCD43A4 v6; LAI from MCD15A3H v6	(126, 127)	https://ladsweb.modaps.eosdis.nasa.gov/search/order/1/MODIS:Combined-Terra-Aqua
cSIF	Global spatially contiguous SIF data set using neural networks and MODIS data	(52)	https://figshare.com/authors/Yao_Zhang/4949929
FLUXNET 2015 data product	Monthly GPP observations from 106 flux sites Annual GPP observations from 22 flux sites	(128)	http://fluxnet.fluxdata.org/data/fluxnet2015-dataset/
Land cover classifications	Global land cover results from land use harmonization (LUH2 v2h) and CCI products	(74, 75)	http://maps.elie.ucl.ac.be/CCI/viewer/download.php http://luh.umd.edu/data.shtml
Revised EC-LUE GPP	GPP data including CO ₂ effects on LUE (1982–2015)	(129)	https://doi.org/10.6084/m9.figshare.8942336.v1
TRENDY v6 GPP and LAI	GPP data from twelve and LAI data from eleven carbon-cycle models	(14)	sftp_trendy-v6@trendy.ex.ac.uk
Global CO ₂ concentration	Mean global CO ₂ based on global air measurement network	(130)	https://www.esrl.noaa.gov/gmd/ccgg/trends/
CRU Version 4.0.1	Global gridded climate product based on weather stations	(131)	http://data.ceda.ac.uk/badc/cru/data/cru_ts/cru_ts_4.01/
Global PAR data	Global PAR data from CRU-NCEP	(132)	https://rda.ucar.edu/datasets/ds314.3/
Global SPEI data set v2.5	Standardized precipitation evapotranspiration index	(133)	http://digital.csic.es/handle/10261/153475
Foliar N and P concentrations observation time series	Observations for foliar N and P concentrations from ICP Forests (410 sites)	(23)	https://doi.org/10.3220/DATA20200824095051
Site-specific observations of foliar N and P concentrations	Site-specific observations of foliar N and P concentrations in Europe (3846 samples)	(134)	https://doi.org/10.3220/DATA20200824095051
Global N and P deposition data	Data for global gridded atmospheric N and P deposition (1980–2013)	(57)	https://figshare.com/s/898e5d6c4f0982674ae3
MERRA-2 data	Soil moisture and terrestrial water storage data from a numerical prediction model (MERRA-2) constrained by multiple observations	(110)	https://gmao.gsfc.nasa.gov/reanalysis/MERRA-2/data_access/
WaterGAP TWS data	Terrestrial water storage data from a global hydrological model (WaterGAP 2.2d)	(111)	https://doi.pangaea.de/10.1594/PANGAEA.918447
ERA-Interim TWS data	Soil moisture and snow storage from an atmospheric re-analysis model	(112)	https://apps.ecmwf.int/datasets/data/interim-full-modat/levtype=sfc/
GLDAS Noah v2.0 TWS data	Soil moisture and snow storage from land surface models	(113)	https://ldas.gsfc.nasa.gov/gldas/GLDASdownload.php

2107 **Table S2. Trends of β using linear regression approach with various combinations of explanatory variables for satellite GPP proxies,**
 2108 **revised EC-LUE GPP and GPP from TRENDY models.** The robustness of the declining trend in β was tested by calculating the trend of β
 2109 using fifteen combinations of explanatory variables, which were listed below. Linear regression approaches were used. Overall fifteen models
 2110 were conducted for the three satellite GPP proxies, revised EC-LUE GPP and GPP from the TRENDY ‘S2’ scenarios. We firstly calculated the β
 2111 time series using 15-year moving windows and then estimated the temporal trends using the Mann-Kendall test. The means and corresponding
 2112 standard errors (SEs) are listed below. Tmax, Tmin and Tmean represent the maximum, minimum and mean air temperatures respectively; Pre,
 2113 precipitation; VPD, vapour pressure deficit; SM, soil moisture; TWS, terrestrial water storage; PAR, Photosynthetically Active Radiation; SPEI,
 2114 Standardized precipitation evapotranspiration index; Ndep, atmospheric nitrogen deposition.

Model no.	Explanatory variables	Trend of β (mean \pm SE, % 100 ppm ⁻¹ y ⁻¹)								
		Satellite GPP proxies					Revised EC-LUE GPP		TRENDY ‘S2’ GPP	
		AVHRR NIR _v	AVHRR+MODIS NIR _v	NIR _v +SIF	Satellite mean	R ²	Trend	R ²	Trend	R ²
1	Tmin+VPD	-0.91 \pm 0.13	-0.92 \pm 0.11	-0.91 \pm 0.13	-0.92 \pm 0.12	0.54	-0.80 \pm 0.17	0.57	0.01 \pm 0.10	0.46
2	Tmax+VPD	-1.01 \pm 0.13	-0.88 \pm 0.11	-0.87 \pm 0.13	-0.92 \pm 0.12	0.54	-0.82 \pm 0.18	0.58	-0.12 \pm 0.12	0.46
3	Tmean+VPD	-0.89 \pm 0.13	-0.91 \pm 0.11	-0.89 \pm 0.13	-0.90 \pm 0.12	0.54	-0.81 \pm 0.17	0.58	-0.01 \pm 0.11	0.46
4	Tmin+pre	-0.91 \pm 0.13	-0.95 \pm 0.11	-0.91 \pm 0.13	-0.93 \pm 0.12	0.55	-0.96 \pm 0.15	0.54	-0.18 \pm 0.08	0.50
5	Tmax+pre	-0.88 \pm 0.13	-0.91 \pm 0.11	-0.88 \pm 0.13	-0.89 \pm 0.12	0.56	-0.97 \pm 0.16	0.56	-0.22 \pm 0.08	0.51
6	Tmean+pre	-0.89 \pm 0.13	-0.93 \pm 0.11	-0.89 \pm 0.13	-0.90 \pm 0.12	0.55	-0.97 \pm 0.16	0.55	-0.22 \pm 0.08	0.51
7	VPD+pre	-0.92 \pm 0.13	-0.94 \pm 0.11	-0.92 \pm 0.13	-0.93 \pm 0.12	0.56	-0.98 \pm 0.19	0.56	-0.36 \pm 0.13	0.48
8	Tmin+VPD+pre	-0.91 \pm 0.13	-0.94 \pm 0.11	-0.91 \pm 0.13	-0.92 \pm 0.12	0.61	-0.84 \pm 0.16	0.64	-0.08 \pm 0.09	0.58
9	Tmax+VPD+pre	-0.87 \pm 0.13	-0.90 \pm 0.11	-0.87 \pm 0.13	-0.88 \pm 0.12	0.61	-0.83 \pm 0.17	0.65	-0.13 \pm 0.10	0.59
10	Tmean+VPD+pre	-0.90 \pm 0.13	-0.93 \pm 0.11	-0.90 \pm 0.13	-0.91 \pm 0.12	0.61	-0.84 \pm 0.17	0.65	-0.11 \pm 0.10	0.59
11	Tmax+VPD+SM	-0.99 \pm 0.13	-1.02 \pm 0.11	-0.99 \pm 0.13	-1.00 \pm 0.13	0.68	-0.95 \pm 0.18	0.71	-0.33 \pm 0.08	0.65
12	Tmax+VPD+TWS	-0.99 \pm 0.13	-1.01 \pm 0.11	-0.99 \pm 0.13	-1.00 \pm 0.13	0.69	-0.96 \pm 0.18	0.71	-0.33 \pm 0.08	0.66
13	Tmax+VPD+PAR	-0.84 \pm 0.12	-0.86 \pm 0.10	-0.84 \pm 0.12	-0.85 \pm 0.11	0.67	-0.80 \pm 0.17	0.70	-0.13 \pm 0.09	0.65
14	Tmax+VPD+SPEI	-0.89 \pm 0.13	-0.91 \pm 0.11	-0.89 \pm 0.13	-0.90 \pm 0.12	0.66	-0.85 \pm 0.16	0.69	-0.17 \pm 0.10	0.66
15	Tmax+VPD+Ndep	-0.74 \pm 0.15	-0.77 \pm 0.12	-0.74 \pm 0.15	-0.75 \pm 0.14	0.61	-0.58 \pm 0.19	0.64	–	–

2115

2116

2117 **Table S3. Trends of β using non-linear regression approach with various combinations of explanatory variables for satellite GPP proxies,**
 2118 **revised EC-LUE GPP and GPP from TRENDY models.** Similar to Table S2, except the non-linear regression approaches were used to
 2119 estimate β . The non-linear regression approaches considered the interaction effects between CO₂ with climatic and environmental factors.

Model no.	Explanatory variables	Trend of β (mean \pm SE, % 100 ppm ⁻¹ y ⁻¹)								
		Satellite GPP proxies					Revised EC-LUE GPP		TRENDY 'S2' GPP	
		AVHRR NIR _v	AVHRR+MODIS NIR _v	NIR _v +SIF	Satellite mean	R ²	Trend	R ²	Trend	R ²
16	Tmin+VPD	-0.94 \pm 0.14	-0.97 \pm 0.12	-0.94 \pm 0.14	-0.95 \pm 0.14	0.65	-0.79 \pm 0.17	0.67	0.02 \pm 0.10	0.58
17	Tmax+VPD	-1.05 \pm 0.14	-0.92 \pm 0.12	-0.89 \pm 0.14	-0.96 \pm 0.13	0.65	-0.81 \pm 0.18	0.68	-0.11 \pm 0.12	0.58
18	Tmean+VPD	-0.92 \pm 0.14	-0.95 \pm 0.13	-0.92 \pm 0.14	-0.93 \pm 0.14	0.64	-0.81 \pm 0.17	0.67	-0.01 \pm 0.10	0.58
19	Tmin+pre	-0.94 \pm 0.14	-0.98 \pm 0.12	-0.94 \pm 0.14	-0.95 \pm 0.14	0.65	-0.97 \pm 0.16	0.64	-0.17 \pm 0.07	0.60
20	Tmax+pre	-0.90 \pm 0.14	-0.93 \pm 0.12	-0.90 \pm 0.14	-0.91 \pm 0.13	0.65	-0.98 \pm 0.17	0.65	-0.21 \pm 0.07	0.61
21	Tmean+pre	-0.91 \pm 0.14	-0.95 \pm 0.12	-0.91 \pm 0.14	-0.93 \pm 0.14	0.65	-0.98 \pm 0.16	0.65	-0.21 \pm 0.07	0.61
22	VPD+pre	-0.95 \pm 0.14	-0.98 \pm 0.12	-0.95 \pm 0.14	-0.96 \pm 0.13	0.66	-1.02 \pm 0.20	0.65	-0.34 \pm 0.12	0.59
23	Tmin+VPD+pre	-0.96 \pm 0.15	-0.99 \pm 0.14	-0.96 \pm 0.15	-0.97 \pm 0.15	0.75	-0.86 \pm 0.17	0.77	-0.09 \pm 0.08	0.73
24	Tmax+VPD+pre	-0.90 \pm 0.15	-0.93 \pm 0.13	-0.90 \pm 0.15	-0.91 \pm 0.14	0.75	-0.84 \pm 0.17	0.77	-0.15 \pm 0.09	0.73
25	Tmean+VPD+pre	-0.94 \pm 0.15	-0.97 \pm 0.14	-0.94 \pm 0.15	-0.95 \pm 0.15	0.75	-0.86 \pm 0.17	0.77	-0.12 \pm 0.08	0.73
26	Tmax+VPD+SM	-1.05 \pm 0.17	-1.10 \pm 0.15	-1.05 \pm 0.17	-1.07 \pm 0.17	0.85	-0.99 \pm 0.19	0.86	-0.37 \pm 0.08	0.83
27	Tmax+VPD+TWS	-1.05 \pm 0.17	-1.09 \pm 0.15	-1.05 \pm 0.17	-1.06 \pm 0.17	0.85	-0.98 \pm 0.18	0.86	-0.36 \pm 0.08	0.83
28	Tmax+VPD+PAR	-0.84 \pm 0.15	-0.88 \pm 0.13	-0.84 \pm 0.15	-0.85 \pm 0.14	0.84	-0.82 \pm 0.17	0.85	-0.15 \pm 0.08	0.83
29	Tmax+VPD+SPEI	-0.93 \pm 0.16	-0.96 \pm 0.14	-0.93 \pm 0.16	-0.94 \pm 0.16	0.84	-0.89 \pm 0.17	0.85	-0.17 \pm 0.09	0.83
30	Tmax+VPD+Ndep	-0.86 \pm 0.14	-0.90 \pm 0.11	-0.86 \pm 0.14	-0.87 \pm 0.13	0.76	-0.74 \pm 0.20	0.77	-	-

2120 **Table S4. Description of the EC flux sites used in this study.** Overall 106 sites were used to
 2121 analyze the relationship between NIRv and GPP, of which 22 flux sites were used to estimate
 2122 the trends of β (marked with black points). Lat: latitude, Lon: longitude.

NO.	Site	Lat	Lon	IGBP	Years	¹	NO.	Site	Lat	Lon	IGBP	Years	¹
1	AT-Neu	47.1	11.3	GRA	2002-2012		54	FR-Fon	48.5	2.8	DBF	2005-2014	
2	AU-ASM	-22.3	133.2	ENF	2010-2014		55	FR-Gri	48.8	2.0	CRO	2004-2014	
3	AU-Cpr	-34.0	140.6	SAV	2010-2014		56	FR-LBr	44.7	-0.8	ENF	1996-2008	
4	AU-DaP	-14.1	131.3	GRA	2007-2013		57	FR-Pue	43.7	3.6	EBF	2000-2014	●
5	AU-DaS	-14.2	131.4	SAV	2008-2014		58	GF-Guy	5.3	-52.9	EBF	2004-2014	
6	AU-Dry	-15.3	132.4	SAV	2008-2014		59	IT-BCi	40.5	15.0	CRO	2004-2014	
7	AU-How	-12.5	131.2	WSA	2001-2014		60	IT-Col	41.8	13.6	DBF	1996-2014	●
8	AU-Stp	-17.2	133.4	GRA	2008-2014		61	IT-Cpz	41.7	12.4	EBF	1997-2009	
9	AU-Tum	-35.7	148.2	EBF	2001-2014		62	IT-Lav	46.0	11.3	ENF	2003-2014	
10	AU-Wom	-37.4	144.1	EBF	2010-2014		63	IT-MBo	46.0	11.0	GRA	2003-2013	
11	BE-Bra	51.3	4.5	MF	1996-2014	●	64	IT-Noe	40.6	8.2	CSH	2004-2014	
12	BE-Lon	50.6	4.7	CRO	2004-2014		65	IT-Ren	46.6	11.4	ENF	1998-2013	●
13	BE-Vie	50.3	6.0	MF	1996-2014	●	66	IT-Ro1	42.4	11.9	DBF	2000-2008	
14	BR-Sa1	-2.9	-55.0	EBF	2002-2011		67	IT-Ro2	42.4	11.9	DBF	2002-2012	
15	CA-Gro	48.2	-82.2	MF	2003-2014		68	IT-SRo	43.7	10.3	ENF	1999-2012	●
16	CA-Man	55.9	-98.5	ENF	1994-2008	●	69	IT-Tor	45.8	7.6	GRA	2008-2014	
17	CA-NS2	55.9	-98.5	ENF	2001-2005		70	JP-SMF	35.3	137.1	MF	2002-2006	
18	CA-NS3	55.9	-98.4	ENF	2001-2005		71	MY-PSO	3.0	102.3	EBF	2003-2009	
19	CA-NS5	55.9	-98.5	ENF	2001-2005		72	NL-Hor	52.2	5.1	GRA	2004-2011	
20	CA-NS6	55.9	-99.0	OSH	2001-2005		73	NL-Loo	52.2	5.7	ENF	1996-2014	●
21	CA-Oas	53.6	-106.2	DBF	1996-2010	●	74	RU-Fyo	56.5	32.9	ENF	1998-2014	●
22	CA-Obs	54.0	-105.1	ENF	1997-2010		75	US-ARM	36.6	-97.5	CRO	2003-2012	
23	CA-Qfo	49.7	-74.3	ENF	2003-2010		76	US-Blo	38.9	-120.6	ENF	1997-2007	
24	CA-SF2	54.3	-105.9	ENF	2001-2005		77	US-Cop	38.1	-109.4	GRA	2001-2007	
25	CA-SF3	54.1	-106.0	OSH	2001-2006		78	US-GLE	41.4	-106.2	ENF	2004-2014	
26	CA-TP1	42.7	-80.6	ENF	2002-2014		79	US-Goo	34.3	-89.9	GRA	2002-2006	
27	CA-TP2	42.8	-80.5	ENF	2002-2007		80	US-Ha1	42.5	-72.2	DBF	1991-2012	●
28	CA-TP3	42.7	-80.3	ENF	2002-2014		81	US-IB2	41.8	-88.2	GRA	2004-2011	
29	CA-TP4	42.7	-80.4	ENF	2002-2014		82	US-Los	46.1	-90.0	WET	2000-2014	
30	CH-Cha	47.2	8.4	GRA	2005-2014		83	US-MMS	39.3	-86.4	DBF	1999-2014	●
31	CH-Dav	46.8	9.9	ENF	1997-2014	●	84	US-Me2	44.5	-121.6	ENF	2002-2014	
32	CH-Fru	47.1	8.5	GRA	2005-2014		85	US-Me3	44.3	-121.6	ENF	2004-2009	
33	CH-Lae	47.5	8.4	MF	2004-2014		86	US-Me6	44.3	-121.6	ENF	2010-2014	
34	CH-Oe1	47.3	7.7	GRA	2002-2008		87	US-NR1	40.0	-105.5	ENF	1998-2014	●
35	CH-Oe2	47.3	7.7	CRO	2004-2014		88	US-Ne1	41.2	-96.5	CRO	2001-2013	
36	CZ-BK1	49.5	18.5	ENF	2004-2014		89	US-Ne2	41.2	-96.5	CRO	2001-2013	
37	CZ-BK2	49.5	18.5	GRA	2004-2012		90	US-Ne3	41.2	-96.4	CRO	2001-2013	
38	CZ-wet	49.0	14.8	WET	2006-2014		91	US-Oho	41.6	-83.8	DBF	2004-2013	
39	DE-Akm	53.9	13.7	WET	2009-2014		92	US-PFa	45.9	-90.3	MF	1995-2014	●
40	DE-Geb	51.1	10.9	CRO	2001-2014		93	US-SRC	31.9	-110.8	OSH	2008-2014	
41	DE-Gri	51.0	13.5	GRA	2004-2014		94	US-SRG	31.8	-110.8	GRA	2008-2014	
42	DE-Hai	51.1	10.5	DBF	2000-2012		95	US-SRM	31.8	-110.9	WSA	2004-2014	
43	DE-Kli	50.9	13.5	CRO	2004-2014		96	US-Sta	41.4	-106.8	OSH	2005-2009	
44	DE-Lkb	49.1	13.3	ENF	2009-2013		97	US-Syv	46.2	-89.3	MF	2001-2014	
45	DE-Lnf	51.3	10.4	DBF	2002-2012		98	US-Ton	38.4	-121.0	WSA	2001-2014	●
46	DE-Obe	50.8	13.7	ENF	2008-2014		99	US-Twt	38.1	-121.7	CRO	2009-2014	
47	DE-Spw	51.9	14.0	WET	2010-2014		100	US-UMB	45.6	-84.7	DBF	2000-2014	
48	DE-Tha	51.0	13.6	ENF	1996-2014	●	101	US-UMd	45.6	-84.7	DBF	2007-2014	
49	DK-Sor	55.5	11.6	DBF	1996-2014	●	102	US-Var	38.4	-121.0	GRA	2000-2014	●
50	DK-ZaH	74.5	-20.6	GRA	1996-2014	●	103	US-WCr	45.8	-90.1	DBF	1999-2014	
51	ES-Amo	36.8	-2.3	OSH	2007-2012		104	US-Whs	31.7	-110.1	OSH	2007-2014	
52	ES-LJu	36.9	-2.8	OSH	2004-2013		105	US-Wkg	31.7	-109.9	GRA	2004-2014	
53	FI-Hyy	61.8	24.3	ENF	1996-2014	●	106	ZA-Kru	-25.0	31.5	SAV	2000-2013	●

2123 ¹These sites are used to calculate the temporal trends of β .

2124 **Table S5. Results of the spatial mixed-effects model.** We used the trends of β as the response
 2125 variables, tree species as the random variables, and also used several potential explanatory
 2126 variables, including mean annual air temperature (MAT), mean annual precipitation (MAP)
 2127 and foliar N and P concentrations. A Gaussian spatial correlation scheme was added in this
 2128 model to account for potential within-group spatial autocorrelations. The models were
 2129 performed using the ‘nlme’ package in R (version 3.4.3)(135).

Effect	Trend of β (% 100 ppm ⁻¹ y ⁻¹)		
	Coefficient \pm SD	<i>F</i>	<i>p</i> > <i>F</i>
Multi-observation mean	<i>R</i> ² = 0.54, <i>p</i> < 0.0001, n = 3846		
MAT (°C)	-0.118 \pm 0.008	160.64	<0.0001
MAP (1000 mm)	-0.723 \pm 0.089	64.90	<0.0001
Foliar N concentration (mg g ⁻¹)	0.035 \pm 0.006	44.65	<0.0001
Foliar P concentration (mg g ⁻¹)	0.065 \pm 0.020	10.39	0.0013

2130